

University of Southampton Research Repository
ePrints Soton

Copyright © and Moral Rights for this thesis are retained by the author and/or other copyright owners. A copy can be downloaded for personal non-commercial research or study, without prior permission or charge. This thesis cannot be reproduced or quoted extensively from without first obtaining permission in writing from the copyright holder/s. The content must not be changed in any way or sold commercially in any format or medium without the formal permission of the copyright holders.

When referring to this work, full bibliographic details including the author, title, awarding institution and date of the thesis must be given e.g.

AUTHOR (year of submission) "Full thesis title", University of Southampton, name of the University School or Department, PhD Thesis, pagination

University of Southampton

PhD Thesis

DESIGN, VALIDATION AND
APPLICATION
OF A NEW COASTAL ALTIMETRY
STRATEGY

Marcello Passaro

Supervisors: Paolo Cipollini, Graham D. Quartly, Helen M. Snaith

A thesis submitted for the degree of Doctor of Philosophy in the
Faculty of Natural and Environmental Sciences School of Ocean and
Earth Science

Submission: September 2015

Declaration

This thesis is a presentation of my original research work. Wherever contributions of others are involved, every effort is made to indicate this clearly, with due reference to the literature, and acknowledgement of collaborative research and discussions.

Marcello Passaro

Acknowledgements

I wish to thank my supervisors, Paolo Cipollini, Graham Quartly and Helen Snaith, for giving me sufficient freedom in my research and at the same time for guiding me towards the right direction. I am very thankful for their understanding demonstrated in the hard moments of the last three years. In particular, a lot of the work behind the ALES algorithm would not have been successful without fruitful discussions with Paolo and his direct contribution in debugging and speeding up bits of code. Moreover, I am particularly grateful to Graham for revising my manuscript; his interest and patience helped me in spotting and correcting inconsistencies.

The same gratitude goes to Jérôme Benveniste, who supervised my traineeship at ESA ESRIN and the members of his satellite altimetry team, Salvatore Dinardo and Bruno Lucas. Moreover, I would like to thank Stefano Vignudelli (IBF-CNR Pisa) and Luciana Fenoglio-Marc (PSGD,TU Darmstadt), who have believed in this project since the beginning and have collaborated as coauthors of peer-reviewed publications, hosting me in their research institutes. I am also grateful to Rosalia Santoleri and her group (ISAC-CNR Roma), who hosted me for three months in their premises.

My thanks go to everyone who has contributed to the development of my research: Yang Le and Bao Li Feng for sharing their algorithms; Christopher Buchhaupt, Maria Joana Fernandes, Ivan Haigh, Abderrahim Halimi, Kristine Madsen, Walter Smith, Luke West, Phil Woodworth for their suggestions.

The development of the ALES algorithm has been partially supported by the Natural Environment Research Council (NERC Ocean Physics Research Programme), the ESA/DUE eSurge (ESA/ ESRIN Contract Number 4000103880/11/I-LG) and eSurge-Venice (ESA/ ESRIN Contract No. 4000104485/11/I-LG) projects. Special thanks go to Prof. Dr.-Ing. Matthias Becker and to the Deutsche Forschungsgemeinschaft (Project COSELE) for the support during the stay at the Institute for Physical and Satellite Geodesy (PSGD) in Darmstadt.

Finally, thanks to all the friends met in Southampton and Rome, who made everything way easier than it would have been otherwise.

Abstract

Satellite altimetry has revolutionised our understanding of ocean dynamics thanks to frequent sampling and global coverage. Nevertheless, coastal data have been flagged as unreliable due to land and calm water interference in the altimeter and radiometer footprint and uncertainty in the modelling of high-frequency tidal and atmospheric forcing.

This thesis addresses the first issue, i.e. altimeter footprint contamination, presenting ALES, the Adaptive Leading Edge Subwaveform retracker. ALES is potentially applicable to all the pulse-limited altimetry missions and its aim is to process both open ocean and coastal data with the same accuracy using just one algorithm. ALES uses only a portion of the returned echo to estimate sea level and sea state, adapting the width of the estimation window according to the significant wave height.

The sea level and the significant wave height estimated by ALES are validated regionally for three different missions: Envisat, Jason-1 and Jason-2. Validation is performed by comparison with in-situ data, i.e. tide gauges and buoys. The results show that ALES is able to provide more reliable 20-Hz data for all three missions in areas where even 1-Hz averages are flagged as unreliable in standard products.

The ALES data are applied to improve the analysis of the annual cycle of the sea level in the North Sea-Baltic Sea transition area. The coastal amplitude of the annual cycle estimated from ALES altimetry data is in better agreement with estimations derived from in situ data than the one from the reference data set. In the Indonesian Seas, ALES data are used to cross-calibrate the SAR altimetry product of Cryosat-2 and to derive an empirical sea state bias correction to the SAR altimetry estimations (equal to 5% of the significant wave height), still missing in the official product.

Contents

Declaration	III
Acknowledgements	III
Abstract	V
1 Introduction	1
1.1 Thesis outline	2
2 Theoretical background and state of the art	5
2.1 The altimetry missions	5
2.2 The altimetric waveform	6
2.3 The altimetric waveforms in the coastal zone	7
2.3.1 Retracking and its state of the art	8
2.4 From range to sea surface height: corrections in the coastal zone . . .	13
2.4.1 Tidal height	13
2.4.2 Wet tropospheric correction	15
2.4.3 Sea state bias	16
2.5 Sea level in the coastal zone	16
2.6 Innovations in satellite altimetry	17
3 Concept and design of an innovative retracker	21
3.1 Mathematical model and estimator	21
3.1.1 ALES rationale	23
3.2 ALES strategy	24
3.2.1 First pass: leading edge detection and fitting	25
3.2.2 Second pass: selection of sub-waveform and precise final estimation	27
3.2.3 Mispointing angle	28

4 The retracking strategy: ALES validation	31
4.1 Methods for validation	31
4.2 ALES sea level validation: Adriatic Sea and Mossel Bay	33
4.2.1 Dataset and area of study	33
4.2.2 Validation of raw data	36
4.2.3 Outlier detection	38
4.2.4 Correlation coefficient	41
4.2.5 Root Mean Square Difference	43
4.2.6 Distribution and bias analysis	46
4.3 ALES Significant Wave Height validation: the German Bight	50
4.3.1 Dataset and area of study	50
4.3.2 Outliers detection and 1-Hz averages	52
4.3.3 Preliminary analysis of DFT gates and σ_p impact in SWH estimation	53
4.3.4 Analysis at the closest locations	55
4.3.5 Along-track analysis	58
5 ALES application: the sea level annual cycle in the North Sea/Baltic Sea transition zone from Envisat	65
5.1 Area of study	66
5.2 Dataset	67
5.3 Methods	69
5.3.1 Data reprocessing	69
5.3.2 Estimation of the annual cycle	72
5.3.3 Estimation of the steric height	75
5.4 Results and discussion	76
5.4.1 Altimetry data quality	76
5.4.2 Time series of sea surface height anomaly	77
5.4.3 Pointwise estimation of the annual cycle	80
5.4.4 Sub-basin estimation of the annual cycle	85
5.4.5 Climatology and steric component of the annual cycle	91
6 ALES application: sea level analysis in the Indonesian seas and expansion to Cryosat-2	95
6.1 Area of study	96
6.2 Dataset	98
6.3 Methods	100
6.3.1 Methods for data screening and outliers detection	100

6.3.2	Methods for the statistics of crossover differences	101
6.3.3	Methods for regional derivation of seasonal signals and trends in the sea level	101
6.4	Results and discussion	102
6.4.1	Comparison of performances between Envisat and CS-2	102
6.5	Statistics of crossover differences and cross-calibration	106
6.6	Inter-calibrated time series	110
6.6.1	North Java and South Java	110
6.6.2	Indonesian Seas	114
7	Overall discussion and impact of the research	117
7.1	Improvements in Range and SWH Estimation	117
7.2	Improvements in coastal sea level analysis	119
8	Conclusions	123
8.1	Future prospect	125
Appendices		127
Appendix A	ALES for AltiKa	129
A.1	ALES for AltiKa: retracking 40-Hz waveforms	129
A.2	ALES for AltiKa: retracking at higher frequencies	131
A.3	Discussion	134

List of Figures

4.1	The areas of study and the extent of the retracked altimetry passes. Top: Northern Adriatic and Gulf of Trieste. Bottom: Mossel Bay, along the South African coast. Bathymetry is shown by means of contour lines: they are drawn every 10 m.	37
4.2	North Adriatic: PCHC for Env 416 (top), J-1 161 (centre) and J-2 196 (bottom). On the x-axis the along-track latitude of the nominal tracks are shown. Land is shaded in grey. The distance from the closest coastline is specified by a green line which refers to the y-axis on the right. For J-2 196, the latitude of the islet which separates the gulf from the lagoon is represented by a vertical dashed line.	39
4.3	South Africa: PCHC for Env 687 (top), and J-2 198 (bottom). On the x-axis the along-track latitude of the nominal tracks are shown. Land is shaded in grey. The distance from the closest coastline is specified by a green line which refers to the y-axis on the right.	40
4.4	North Adriatic: percentage of outliers for Env 416 (top), J-1 161 (centre) and J-2 196 (bottom). On the x-axis the along-track latitude of the nominal tracks is shown. Land is shaded in grey. The distance from the closest coastline is specified by a green line which refers to the y-axis on the right. For J-2 196, the latitude of the islet which separates the gulf from the lagoon is represented by a vertical dashed line.	42
4.5	South Africa: percentage of outliers for Env 687 (top), and J-2 198 (bottom). On the x-axis the along-track latitude of the nominal tracks is shown. Land is shaded in grey. The distance from the closest coastline is specified by a green line which refers to the y-axis on the right.	43
4.6	North Adriatic: correlation coefficient between Trieste TG and Env 416 (top), J-1 161 (centre) and J-2 196 (bottom). On the x-axis the along-track latitude of the nominal tracks is shown and the latitude of the TG is highlighted with a black dot. Land is shaded in grey. The distance from the closest coastline is specified by a green line which refers to the y-axis on the right. For J-2 196, the latitude of the islet which separates the gulf from the lagoon is represented by a vertical dashed line. Negative values and correlation computed for less than 10 points in the time series are not shown.	44

4.7 South Africa: correlation coefficient between Mossel Bay TG and Env 687 (top), and J-2 198 (bottom). On the x-axis the along-track latitude of the nominal tracks is shown and the latitude of the TG is highlighted with a black dot. Land is shaded in grey. The distance from the closest coastline is specified by a green line which refers to the y-axis on the right. Negative values and correlation computed for less than 10 points in the time series are not shown.	45
4.8 North Adriatic: absolute RMS difference between Trieste TG and Env 416 (top), J-1 161 (centre) and J-2 196 (bottom). On the x-axis the along-track latitude of the nominal tracks is shown. Black dots on the x-axis highlight the latitude of the TG (big dot) and of the closest point along track (small dot). Land is shaded in grey. The distance from the closest coastline is specified by a green line which refers to the y-axis on the right. A black dashed line marks the difference between the along track mean sea surface (DTU10) and the mean sea surface DTU10 at the TG. For J-2 196, the latitude of the islet which separates the gulf from the lagoon is represented by a vertical dashed line.	46
4.9 South Africa: RMS of the difference between Mossel Bay TG values and Env 687 TWLE (top), and J-2 198 TWLE (bottom). The mean of the difference for each along track location was removed. On the x-axis the along-track latitude of the nominal tracks is shown. Black dots on the x-axis highlight the latitude of the TG (big dot) and of the closest point along track (small dot). Land is shaded in grey. The distance from the closest coastline is specified by a green line which refers to the y-axis on the right.	47
4.10 Histograms of consecutive TWLE differences in modulus for each track for SGDR (blue) and ALES (red). Columns of SGDR are thinner in order to facilitate the distinction.	48
4.11 The areas of study and the extent of the retracked altimetry passes. Bathymetry is shown by means of contour lines: they are drawn every 5 m.	51

4.12 Two examples of radargrams for each Envisat track: the upper panels correspond to times of high tide, while the lower panels refer to a low-tide situation. Each column correspond to a high-rate waveform along a satellite track. The horizontal dimension corresponds to the latitude of each waveform. The intensity of the return is colour-coded from blue to red. The area of the tidal flats is recognisable by the presence of specular waveforms (single narrow peak and no gradual decay in the trailing edge), particularly evident at low tide, when more land lies above the sea level.	53
4.13 Analysis of 4 different retracking strategies for Envisat. Statistics are produced considering the 20 nominal high-rate points from Env 474 and Env 85 closest to the Helgoland buoy and the high-rate points from Env 85 closest to the Elbe buoy. The difference between ALES SWH retrieval and buoy measurements are analysed in terms of A) mean bias, B) standard deviation (std), C) percentage of outliers and D) number of available observations for varying SWH.	55
4.14 Scatter plot of Envisat retracked SWH against the corresponding in-situ estimations at the closest 1-Hz point of the satellite track to the buoy. Shown are the results with ALES with waveforms augmented by 2 gates (full circle), standard SGDR (open circle) and SGDR recomputed using a different σ_p (open square)	57
4.15 Scatter plot of Jason retracked SWH against the corresponding in-situ estimations at the closest point of the satellite track to the buoy. The upper plots refer to the 20-Hz data, the lower to the 1-Hz data. The plots on the left refer to Jason-2, the plots on the right to Jason-1. Shown are the results with ALES (full circle) and standard SGDR (open circle).	58
4.16 Along-track validation of SWH estimations for Envisat pass 85 against data from Elbe (left) and Helgoland (right) buoys in terms of PCHC at 1 Hz and 18 Hz (top), std of 1-Hz estimations from buoy values (centre) and median bias of 1-Hz estimations (bottom). On the x-axis the along-track latitude of the nominal tracks are shown. Land is shaded in grey. The closest point of the track from the buoy is highlighted by a black dashed vertical line. The distance up to 30 km from the closest coastline is specified by a green line which refers to the y-axis on the right.	61

4.17 Along-track validation of SWH estimations for Envisat pass 474 against data from the Helgoland buoy (left) and Envisat pass 543 against data from the Westerland buoy (right) in terms of PCHC at 1 Hz and 18 Hz (top), std of 1-Hz estimations from buoy values (centre) and median bias of 1-Hz estimations (bottom). On the x-axis the along-track latitude of the nominal tracks are shown. Land is shaded in grey. The closest point of the track from the buoy is highlighted by a black dashed vertical line. The distance up to 30 km from the closest coastline is specified by a green line which refers to the y-axis on the right.	62
4.18 Along-track validation of SWH estimations for Jason-2 (left) and Jason-1 (right) pass 213 against data from the Helgoland buoy in terms of PCHC at 1 Hz and 20 Hz (top), std of 1-Hz estimations from buoy values (centre) and median bias of 1-Hz estimations (bottom). On the x-axis the along-track latitude of the nominal tracks are shown. Land is shaded in grey. The closest point of the track from the buoy is highlighted by a black dashed vertical line. The distance up to 30 km from the closest coastline is specified by a green line which refers to the y-axis on the right.	63
5.1 The area of study. On the left, the red circles are the locations of the TGs and the black lines are the Envisat tracks. On the right, the sub-basin are defined and colour-coded and the main circulation pattern is shown. Colorscale is linear between 0 and -100 and then linear but with different slope between -100 and -800.	67
5.2 Monthly averages of SSHA (with 3-month running mean filter applied) grouped by sub-basin, from TGs (black dashed line) and satellite altimetry within 15 km of the coast for ALES reprocessed dataset (red squares) and Envisat SL_cci (blue circles).	71
5.3 Autocorrelation function of the residuals after OLS (above) and PW FGLS annual cycle estimation for the time series of ALES reprocessed altimetry data in the Kattegat Sea within 15 km of the coast. The blue line indicate the 95% confidence bounds of the autocorrelation. The time lag on the x axis is in months.	73
5.4 Comparison between ALES reprocessed (left) and Envisat SL_cci (right) datasets in terms of number of cycles available (upper plots) and standard deviation of the SSHA time series (lower plots) for each 1-Hz location.	78

5.5	Histogram of the root mean square of SSHA computed at each 1-Hz location from ALES reprocessed (red), Envisat SL_cci (blue) and RADS (green) datasets.	79
5.6	Monthly averages of zonal wind stress from 20 century (CR20 v2) reanalysis (in green) and of SSH (in blue) from ALES dataset within 15 km of the coast in Sweden Skagerrak.	81
5.7	Estimates of annual cycle amplitude from TG data (squares) and 1-Hz altimetry points along the Envisat tracks for ALES reprocessed dataset (left) and Envisat SL_cci (centre). The plot on the right shows the estimates from gridded SL_cci.	81
5.8	Standard deviation of the SSH RADS time series for each 1-Hz location.	84
5.9	Estimates of the amplitude of the annual cycle of the sea level (top) and corresponding uncertainty at 95% level (bottom) for each sub-basin from TG data (black cross) and altimetry within 15 km of the coast, from 15 to 25 km and from 25 to 35 km (left to right in each sub-basin box). The estimation is performed with the PW method. The estimates come from ALES reprocessed dataset (blue), Envisat SL_cci (cyan) and gridded SL_cci (grey).	86
5.10	Estimates of the phase of the annual cycle of the sea level (top) and corresponding uncertainty at 95% level (bottom) for each sub-basin from TG data (black cross) and altimetry within 15 km of the coast, from 15 to 25 km and from 25 to 35 km (left to right in each sub-basin box). The estimation is performed with the PW method. The estimates come from ALES reprocessed dataset (blue), Envisat SL_cci (cyan) and gridded SL_cci (grey). The estimates correspond to timing of annual cycle maximum.	89
5.11	Annual cycle amplitude (left) and month of the annual cycle maximum (right) of the steric height derived from climatological data. . .	92
5.12	Estimates of the sinusoidal signal related to the annual cycle of the mass component of the sea level variability (thick line) for each sub-basin, obtained by subtracting the steric annual signal (estimated from climatology, thick dashed line) from the total annual signal (estimated from ALES dataset, thin dashed line). Estimates are computed from data within 15 km of the coast (red), and from 25 to 35 km (blue).	94

6.1	The domains selected North and South of Java Island (NJ and SJ) delimited by the black lines and the SAR boxes of CS-2 (delimited by the red lines).	98
6.2	The basins of interest within the Indonesian seas, defined according to the <i>Limits of Ocean and Seas</i> published by the International Hydrographic Organization in 1953.	98
6.3	Statistics for the time series of Env B ALES (blue), Env C ALES (orange) and Cryosat-2 SARvatore (red) in North Java (left) and South Java (right). A.1 and A.2: number of satellite passes available in each month. B.1 and B.2: Standard Deviation of the monthly SLA values. C.1 and C.2: Standard Deviation of the monthly geophysical correction applied to the SLA estimations. Only data from months when at least 10 passes were available are shown.	103
6.4	Overpass time in the Java region for Envisat (blue) and Cryosat-2 (red).	104
6.5	Average 20Hz noise of the SLA values in SJ and NJ within 50 km of the coast for Env B ALES (blue), Env C ALES (orange) and CS-2 SARvatore (red). Also shown is the average estimated Significant Wave Height for each mission (green curves).	105
6.6	Variability of the parameters of interest in North Java (left column) and South Java (right column) depending on the distance from the coastline (in km on the x axis) for Env B ALES (blue), Env C ALES (orange) and CS-2 SARvatore (red). Top: Standard Deviation of the monthly SLA values. Bottom: Average 1Hz noise of the SLA values. . .	105
6.7	Upper plot: distribution of crossover differences depending on time difference between the satellite passes. Lower plot: distribution of crossover differences depending on distance from the coastline. . . .	106
6.8	Left: Histogram of crossover differences considering only points farther than 70 km of the coast. Right: Same histogram with focus on the crossovers between Env C and CS-2 with and without applying a SSB correction in each dataset.	107
6.9	Mean (top), standard deviation (middle) and number (bottom) of crossover differences grouped according to the distance from the coast. The squares are horizontally displaced to facilitate the reading. . . .	108
6.10	SLA difference at crossover points versus SWH estimation from Cryosat-2; the linear fitting shows a slope of 1 cm in 1 m and an intercept at -2 mm.	109

6.11	Mean (top), standard deviation (middle) and number (bottom) of crossover differences grouped according to the distance from the coast and sub-basin of reference. The squares are horizontally displaced to facilitate the reading.	110
6.12	Time series in NJ and SJ at 0-50 km from the coast using Envisat B+C data (blue dotted lined) or Envisat B+CS2 data (red dotted line). The straight lines show the linear fitting using Envisat B+C data (blue), Envisat B+CS2 data (red) and Envisat B+CS2 data only until the end of Envisat Phase C ("ALES Env B + CS2 lim", in green)	111
6.13	Multimission EnvB+CS2 time series (in red) and Jason-Colorado Uni time series (blue) for Java Sea (top left), Flores Sea (top right), Banda Sea (bottom left) and Ceram (bottom right). The black straight line indicates the start of CS2 dataset.	116
A.1	AltiKa pass 416 (14 cycles): PCHC (top), correlation coefficient (centre) and absolute RMS difference (bottom) between Trieste TG and ALES (SGDR) data in red (blue). On the x-axis the along-track latitude of the nominal tracks are shown. Black dots on the x-axis highlight the latitude of the TG (big dot) and of the closest point along track (small dot). Land is shaded in grey. The distance from the closest coastline is specified by a green line which refers to the y-axis on the right. A black dashed line marks the difference between the along track mean sea surface (DTU10) and the mean sea surface DTU10 at the TG.	130
A.2	Tracking error engendered by summing fewer IEs. a) Illustration that the leading edge is well-defined by just a few summed pulses, whereas the trailing edge is much less clear. b), d) Consistency of retracking of range and SWH respectively within a 1s burst. c), e) Mean absolute bias (relative to processing of 40-Hz waveforms) for range and <i>SWH</i>	133

ACRONYMS AND ABBREVIATIONS

ALES	Adaptive Leading Edge Subwaveform
BLUE	Best Linear Unbiased Estimator
CTOH	Centre For Topographic Studies Of The Ocean And Hydrosphere
CPP	Coastal Proximity Parameter
CS-2	Cryosat-2
CU	Colorado University
DFT	Discrete Fourier Transform
DAC	Dynamic Atmosphere Correction
DTC	Dry Tropospheric Correction
ENS	El Niño Southern Oscillation
ECMWF	European Centre For Medium Range Weather Forecasting
FGLS	Feasible Generalised Least Squares
FFT	Fast Fourier Transformed
GCOS	Global Climate Observing System
GNSS	Global Navigation System (GNSS) Stations
GPD	GNSS-Based Path Delay
LRM	Low Resolution Mode
MLE	Maximum Likelihood Estimation
MSS	Mean Sea Surface
MAD	Median Absolute Deviation
MMSE	Minimum Mean Square Estimator
NOCS	National Oceanography Centre Southampton
NM	Nelder-Mead
NJ	North Of Java Island
SJ	South Of Java Island
NCC	Norwegian Coastal Current
OLS	Ordinary Least Squares
PCHC	Percentage Of Cycles For High Correlation
PTR	Point Target Response
PW	Prais-Winsten
PSMSL	Permanent Service For Mean Sea Level
PRF	Pulse Repetition Frequency
r	Correlation Coefficient
RADS	Radar Altimetry Database System

RMS	Root Mean Square
RMSE	Root Mean Square Error
RMSD	Root Mean Square Of The Difference
SL cci	Sea Level Climate Change Initiative
SSB	Sea State Bias
SSHA	Sea Surface Height Anomaly
SGDR	Sensor Geophysical Data Records
SWH	Significant Wave Height
SODA	Simple Ocean Data Assimilation
Std	Standard Deviation
TG	Tide Gauge
TWLE	Total Water Level Envelope
WTC	Wet Tropospheric Correction
ZWD	Zenith Wet Delay

Chapter 1

Introduction

Satellite altimetry has become an invaluable oceanographic tool: after decades of observing the oceans only by "in-situ" measurements, the advent of remote sensing meant the possibility to obtain repeated measurements all over the ocean. It became therefore possible to monitor the sea level, the sea state and, indirectly, the geostrophic currents, on a global scale, reaching areas that are hardly crossed by oceanographic cruises.

The increasing precision of the measurements lead to a wide literature describing the global circulation and the sea level trends, which have had a lead role in the description of the changes that are happening in the Earth climate system, where the ocean plays a main role.

The measurement of sea level from the satellites is based on the estimation of the distance between the satellite and the ocean surface ("range"), which needs to be corrected for a number of factors, mainly depending on the fact that the signal travels through the atmosphere. The range and the sea state are estimated in a process called "retracking".

While retracking and corrections are procedures that guarantee an accuracy of 2.5 cm for averaged estimations every 7 km along a track [2], this is not yet true in the coastal ocean. There are three types of limitations concerning standard satellite altimetry in the coastal regions: the presence of land and areas with different scattering characteristics in the satellite footprint interferes with the radar signal; the geophysical corrections applied in standard altimetry are not suitable to the shorter spatial and temporal wavelengths of coastal dynamics; the current sampling is insufficient to detect and distinguish features like coastal tides or flow instabilities [3].

The coasts are the most highly populated areas in the world and at risk considering the current level at which the sea level is rising. In-situ observations are scarcest

in some of the highest populated areas, which are also hotspots of sea level rise such as Indonesia. The advances in coastal altimetry can have high societal impact: a better description of the sea level and circulation in the coastal zone can raise local awareness and help the plans of adaptation. In oceanographic terms, the coastal ocean sees the strongest variability in terms of coastal currents and sea level variations. Models are currently not able to replicate this variability and the availability of coastal altimetry observation can help the efforts, not only by cross-validation, but also by the possibility of assimilating the new estimations. An accurate coastal altimetry product is therefore needed for the benefit of applications such as local circulation models [4], sea level analysis [5] and observations of storm surges [6].

Upcoming satellite missions will enhance the potential of coastal altimetry in the near future, but it is important to reprocess the already existing 20 years of observations, which already span a considerable window on seasonal, annual and interannual time scales.

The objective of this research is to bridge innovative solutions in terms of signal processing of the altimetry waveforms to the actual usefulness in terms of scientific exploitation of a new coastal altimetry dataset. In particular, this thesis aims at:

1. Developing the optimal retracking solution.
2. Defining and applying the criteria to demonstrate the performances of a retracking system.
3. Evaluating the improvements that the use of a coastal dedicated altimetry strategy brings to regional sea level analysis.

1.1 Thesis outline

The next chapters are structured as follows

- Chapter 2 provides the theoretical background and briefly analyse the state of the art of retracking;
- Chapter 3 introduces the Adaptive Leading Edge Subwaveform (ALES) retracking algorithm;
- Chapter 4 provides the validation of the algorithm by comparing the results against in-situ data;

-
- Chapter 5 includes the application of the ALES-derived coastal sea level dataset in the North Sea/Baltic Sea transition zone and discuss the improvements brought to the seasonal sea level analysis;
 - Chapter 6 discusses the synergy between the ALES-derived dataset and the dataset coming from the new generation of satellite altimeters, focusing on sea level analysis in the Indonesian archipelago;
 - Chapter 7 summarises the main findings and discusses the significance of this research.
 - Chapter 8 draws the conclusions and proposes future steps and synergies of the project.

Chapter 2

Theoretical background and state of the art

2.1 The altimetry missions

The history of satellite altimetry dates back to the 1970s, particularly with the launch of Seasat in 1978 and then Geosat in 1985. The evolution of radar techniques and of the orbit determination has gradually increased the precision and therefore the usability of satellite altimetry data. In particular, the launches of ERS-1 in 1991 (followed in the same orbit by ERS-2 in 1995, Envisat in 2002 and Altika in 2013) and of Topex/Poseidon in 1992 (followed in the same orbit by Jason-1 in 2001 and Jason-2 in 2008) marked the beginning of the era of continuous global altimetry observations along repeated tracks. As this author writes, new missions are being developed and some are about to be launched, guaranteeing the continuity of service, but also experimenting with innovations as briefly described in section 2.6.

The methods of this research are applied in particular to the Envisat and the Jason missions, given the availability of raw data, the precision of their orbit determination and their relevance for climatic studies. Envisat and Jason mainly differ between each other for the orbit characteristics: while Envisat had a 35-day repeating sun-synchronous orbit (with impacts on the aliasing of tidal components, as discussed in chapter 5), the Jason series follows a 10-day prograde orbit with a much larger track spacing. The orbital characteristics of these missions are summarised in table 2.1. The theoretical basis described in this chapter applies to both Envisat and the Jason series, unless otherwise specified.

	Envisat	Jason 1	Jason 2
Mission duration	2002-2012	2001-2012	2008-ongoing
Repeat cycle	35 days	10 days	10 days
Track spacing at the equator	80 km	315 km	315 km

Table 2.1: Mission characteristics for Envisat, Jason 1 and Jason 2.

2.2 The altimetric waveform

Satellite altimetry is based on a simple radar principle. A short pulse of radiation with known power is transmitted from a satellite towards the sea. The pulse interacts with the rough sea surface and part of the incident radiation within the altimetric footprint reflects back to the radar altimeter, which records the returned echo of the pulse. The power of the signal as received by the satellite is registered in a time series called a "waveform", sampled with a two-way travel time resolution of 3.125 ns; each resolution cell is known as a "gate". The acquisition depends on the functioning of the on-board tracker, which adjusts the altimeter observation window in time in order to keep the reflected signal coming from the Earth within the window. The output of the on-board tracker is the "Tracker range", which is a first estimation of the distance between the satellite and the sea surface.

Each individual echo is strongly perturbed by Rayleigh noise (speckle) coming from the incoherent addition of signals from reflecting facets inside the satellite footprint [7]. Assuming that noise on consecutive waveforms is uncorrelated (which sets an upper boundary on the useful pulse repetition frequency of the altimeter [8]), it can be reduced by averaging a number of waveforms prior to transmission (downlink) to the ground. Typical downlinked "high-rate" waveforms at ~ 20 Hz are an average of 100 consecutive samples at ~ 2 kHz [7]. In order to retrieve geophysical information from these waveforms, a processing step called "retracking" has to be performed on the ground [9]. The retracking process consists of fitting a model response to the real waveform. Over the open ocean, most waveforms are well described by the Brown-Hayne mathematical model [10, 11], which is recalled in section 2.3.1 and which is the standard model used for retracking for ocean surfaces.

Waveforms that conform to the Brown-Hayne model present a fast-rising leading edge and a slowly-decaying trailing edge. Figure 2.1 shows the characteristics of an idealized open ocean waveform without noise, in order to define the parameters of interest for the retracking. The mid-point of the leading edge is chosen as an estimate of the distance between the satellite and the sea surface (range), since it

is related to the sea surface mean position at nadir. The leading edge is therefore particularly important for the retracking, since it contains the parameters that a retracker usually estimates: the position of the mid-point with respect to the fixed nominal tracking point determined by the on-board tracker (Epoch τ); the rise time of the leading edge, which is related to the significant wave height (SWH); the amplitude of the received signal, from which the backscatter coefficient σ^0 is derived and then related to the wind speed. The retracked range is computed by adding the Epoch to the Tracker range. The figure also shows that the slope of the trailing edge is related to the antenna mispointing angle, i.e. the angle that the real pointing direction of the antenna forms with the desired nadir position.

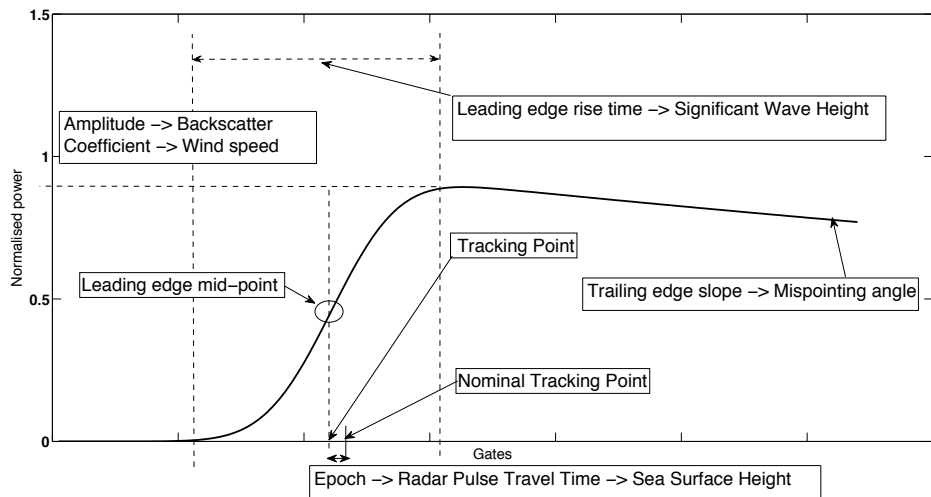


Figure 2.1: Characteristics of an idealised open ocean waveform.

2.3 The altimetric waveforms in the coastal zone

The residual noise of real waveforms, particularly evident along the trailing edge, can influence the correct retrieval of the parameters of interest in the retracking process, since the waveforms deviate from the theoretical open ocean shape. This is known to happen in particular in the last 10 km from the coastline: at this distance, both coastal waters and raised land can give returns within the altimeter's range window, changing the waveform shape from that expected for a homogeneous surface. Several studies in recent years have classified coastal waveforms [12, 13, 14]. Two of the predominant coastal waveform classes are quasi-specular and multi-peak echoes [15]. They are both connected with the presence of highly reflective targets (bright targets) whose signatures are seen tracing an hyperbola in consecutive

waveforms, as seen in the examples of figure 2.2 [16].

The physical features causing bright targets are still subject to debate. [17] states that signals coming from small targets like ships are only detected in the first gates before the leading edge, while land features such as islands can influence the entire waveform due to their high backscatter coefficient. In the same study, the fact that coastal bright targets are not present in every cycle is attributed to exposure of tidal flats by the tidal cycle. [18] and [19] have investigated the bright targets over a coastal area near the island of Pianosa. They both concluded that the presence of patches of high reflectance is not a constant event and that they are most likely related to sea state and can be generated by unbroken wave crests and patches of calm water.

Figure 2.2 shows six along-track radargrams (stacks of consecutive high-rate waveforms, one for each column) from Envisat track 416 flying over the northern end of the Adriatic Sea (map in figure 4.1). Land is shaded in grey. The colorbar codes the power of each gate for every waveform. Brighter features in the speckle noise along the trailing edge are seen progressing from later gates towards the leading edge and back, along hyperbolic paths as expected from simple geometrical arguments [18].

Using geometry considerations described in [20] and assuming that the actual tracking point is not significantly different from its nominal position, it is possible to compute the distance of the last gate of the waveform from the nominal tracking point, i.e. the radius of the satellite footprint at the end of the trailing edge, which is 7.3 km for Envisat and 8.3 km for Jason for calm seas. Depending on the elevation, land returns could still appear in the trailing edge, even if the surface is located outside the expected footprint, because their location could be equidistant with the ocean surface near nadir. Nevertheless, this would produce a more predictable hyperbolic feature than what is shown in the radargrams, where bright targets are not seen constantly at every cycle and their location and extent varies. It is therefore evident that the perturbations cannot be exclusively attributed to land in the satellite footprint.

2.3.1 Retracking and its state of the art

The Brown model

The Brown-Hayne theoretical ocean model [10, 11] is the standard model for the open-ocean retrackers and describes the average return power of a rough scattering surface (i.e. what we simply call *waveform*). The return power V_m is

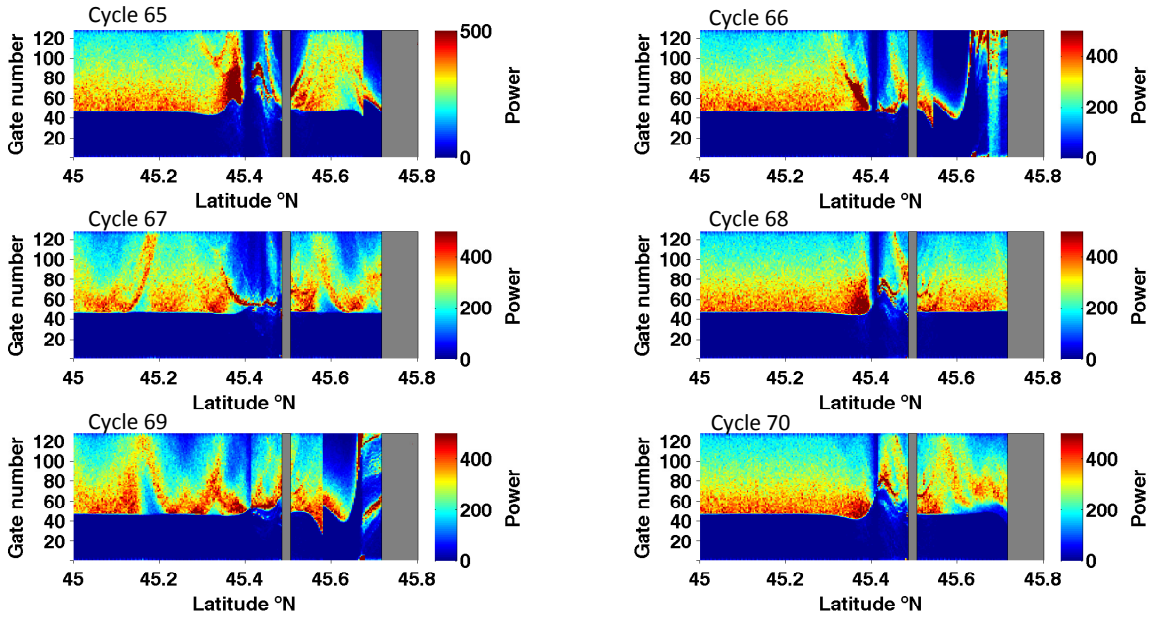


Figure 2.2: Radargrams of Envisat track 416 over the Adriatic Sea (cycles 65 to 70). Land is shaded in grey. Every vertical line corresponds to a waveform at a latitude specified on the X axis. Y axis: gate numbers for each waveforms. The colorbar shows the power level for each gate.

$$V_m(t) = a_\xi P_u \frac{[1 + \operatorname{erf}(u)]}{2} \exp(-v) + T_n \quad (2.1)$$

where

$$a_\xi = \exp\left(\frac{-4 \sin^2 \xi}{\gamma}\right) \quad \gamma = \sin^2(\theta_0) \frac{1}{2 \cdot \ln(2)}$$

$$\operatorname{erf}(x) = 2 \frac{1}{\sqrt{\pi}} \int_0^x e^{-t^2} dt$$

$$u = \frac{t - \tau - c_\xi \sigma_c^2}{\sqrt{2} \sigma_c} \quad v = c_\xi \left(t - \tau - \frac{1}{2} c_\xi \sigma_c^2 \right)$$

$$c_\xi = b_\xi a \quad b_\xi = \cos(2\xi) - \frac{\sin^2(2\xi)}{\gamma} \quad a = \frac{4c}{\gamma h \left(1 + \frac{h}{R_e}\right)}$$

$$\sigma_c^2 = \sigma_p^2 + \sigma_s^2 \quad \sigma_s = \frac{SWH}{2c}$$

where c is the speed of light, h the satellite altitude, R_e the Earth radius, ξ the off-nadir mispointing angle, θ_0 the antenna beam width, τ the Epoch with respect to the nominal tracking reference point, σ_c the rise time of the leading edge (depending on a term σ_s linked to SWH and on the width of the radar point target response σ_p), P_u the amplitude of the signal and T_n the thermal noise level.

In practice, the model in equation 2.1 is a raised sigmoid $\frac{[1+\text{erf}(u)]}{2}$ describing the increasing power in the waveform leading edge and the subsequent plateau, multiplied by a negative exponential which models the reduction of power in the waveform tail (decay), plus thermal (additive) noise T_n . The amplitude of the signal P_u is attenuated by a term a_ξ dependent on mispointing ξ . P_u can be converted into a measurement of the backscatter coefficient σ^0 on the basis of the instrument calibration. Note that the SWH, in addition to affecting the rise time of the waveform, also has a small effect on the sigmoid location (variable u) and on the waveform decay (variable v), via the term $c_\xi \sigma_c^2$.

The rise time of the leading edge (σ_c) depends on the width of the radar point target response σ_p and on a term σ_s linked to SWH. It is important here to stress the meaning of σ_p . The point target response (PTR), convolved with the probability density function of the sea surface height distribution and the step function, defines the average of the illuminated area within the satellite footprint [9]. The PTR has the form of a sinc^2 function and, in order to simplify the convolution, is approximated in the Brown model by a Gaussian function of which σ_p describes the width:

$$PTR(t) \sim \exp\left(\frac{-t^2}{2\sigma_p^2}\right) \quad (2.2)$$

The value of σ_p changes depending on the mission. In the Jason processing, $\sigma_p = 0.513r_t$ is used, with r_t the time resolution (3.125 ns). Envisat data have been originally processed with $\sigma_p = 0.53r_t$ [16]. These are also the values used by ALES for both missions.

In the latest version of the Envisat Sensor Geophysical Data Records (SGDR), the value of σ_p was switched to $0.6567r_t$. As noted in [21], this had a particularly

strong impact at low SWH: for real SWH of 1 m, the new values are lower than previously by 30 cm and too small compared to buoys or models. Moreover the noise of the retrieval for small waves is now higher and this is attributed to be a direct consequence of the non linear dependancy of SWH from σ_p . The effect of the two different values of σ_p for Envisat is tested on ALES estimations in section 4.3.3.

A complete physical description of the functional form can be found in [10] and [16].

Sampling issues in altimetry

In the standard procedure of pulse-limited altimetry, as a result of the sampling of the individual echo, 128 In-Phase/Quadrature samples are gathered and Fast Fourier transformed (FFT) [9]. For Envisat the 128 gates of each 18-Hz waveform have been obtained by squaring the modules of the FFT and averaging over 100 echoes. Each 128 values of an FFT correspond to a given frequency. In order to better describe the leading edge two additional gates have been stored in the SGDR [22]: a Discrete Fourier Transform (DFT) algorithm was computed on-board at two intermediate frequencies chosen to be in the leading edge portion of the waveform and the corresponding values were then squared and averaged as described above in the standard procedure.

The increased sampling also gives a partial solution to the undersampling issue in conventional altimeters, described by [23]. Since the pulse bandwidth of a conventional altimeter is $B = 320$ MHz, to respect the Nyquist theorem it would be sufficient to sample the signal with a rate corresponding to a gate spacing of $\Delta = c/2B = 0.468$ m, which is the gate spacing of the waveforms. Nevertheless, since both Jason and Envisat form the waveforms by squaring the magnitude of a complex function resulting from the Fourier transformation of the receiver output, the bandwidth is actually doubled and the waveform is consequently undersampled, due to the fact that the range resolution corresponds to half of the Nyquist rate. This problem is particularly felt in the case of fast rising times (which translated into very low SWH values), since the leading edge of the waveform is poorly described.

The effect of the insertion of the additional gates is tested in ALES together with different values of σ_p . The results are presented in section 4.3.3 and the best method is then used for validation in chapter 4.

Jason does not provide additional gates and therefore in this study the waveforms are interpolated prior to retracking in order to double the amount of gates by oversampling and increase the redundancy of the information across the leading edge.

An optimal solution would be the interpolation of the complex amplitudes of every single echo, before squaring the magnitudes and averaging the results. Individual echoes are not available and therefore this strategy is not feasible. For this study, it was decided to perform on every 20-Hz waveform an Akima interpolation, i.e. a piecewise spline interpolation that fits a smooth curve to the given points [24].

Existing retracking methods

Regardless of their origin, the bright targets previously described degrade the estimation of geophysical parameters based on Brown-Hayne retracking. To avoid this problem, different dedicated coastal retracking solutions have been suggested and tested in recent years. The latest strategies involve one or a combination of the following methods:

- the classification of the waveforms depending on their shape [25, 13, 14, 26]
- the use of empirical parameters and/or threshold values to model the waveform [25, 27, 28, 29]
- the adaptation of a different functional form for every kind of characteristic shape that the waveforms can assume [30, 14]
- the simultaneous processing of multiple waveforms to detect the bright targets prior to retracking [18, 31]
- the addition of peaks to the Brown-Hayne functional form to model the presence of bright targets [32]
- the retracking of subwaveforms, i.e. portion of waveforms not affected by the bright targets [33, 34, 35, 26, 15]

Most of these attempts have been successful in demonstrating that meaningful geophysical estimates can be retrieved from data records which were previously disregarded. However there are a number of still unresolved issues. The use of empirical and threshold retrackers lacks a physical description of the functional form; moreover the choice of parameters might vary in different coastal conditions. The addition of further parameters (peaks) to the model can improve the overall fitting of the waveform without necessarily resulting in a better fitting of the three important parameters (τ , SWH, σ_0), and also introduces additional complications in terms of numerical convergence of the estimation. The use of different retrackers depending on conditions and the switching from one to another, requires an accurate quantification of biases amongst them, to avoid "jumps" in the retrieved parameters. Even

the simple distinction between open and coastal ocean to apply different retracking strategies raises questions about where the boundary should be set, and what are the consequences of introducing such a discontinuity.

2.4 From range to sea surface height: corrections in the coastal zone

Figure 2.3 illustrates the steps that have to be followed to extract the sea surface height signal from range retrievals. The orbit determination systems provide a precise altitude of the satellite of a reference surface (ellipsoid). The sea surface height is obtained by subtracting the range from the satellite altitude, but this measurement, besides the instrumental effects, have also to be corrected for the atmospheric effects that influence the radar speed and for other time-variable geophysical phenomena. Near the coast, some of the standard corrections are degraded and need to be improved.

Oceanographers are often interested in deriving the anomaly with respect to a mean state excluding the tidal component of the variability (tidal height) and the effect of the atmospheric pressure on the sea surface (atmospheric pressure loading). Ideally, the height of the geoid could be extracted from the signal in order to isolate the variable part, given that the geoid is an equipotential surface that can be considered constant on a first approximation and that corresponds to the undisturbed state of the ocean (i.e., without any variation caused by currents, tides or interactions with the atmosphere). In standard practice, a mean sea surface (MSS) that approximates the geoid is removed from the sea surface height and the remaining signal is defined as the sea surface height anomaly (SSHA).

Assessing the quality of the corrections applied to the range goes beyond the scope of this research. Nevertheless, it is important to briefly resume the problems that affect in particular the wet tropospheric correction and the estimation of the tidal height in the coastal zone. A comprehensive description of the corrections and their impact on the coastal sea level estimation can be found in [36].

2.4.1 Tidal height

In shallow waters, the tidal wavelength changes proportionally to the square root of depth and therefore varies with the bathymetry, resulting in complex local shallow-water tidal constituents. Tides near the coast can cause a variation of several meters to the sea level and their high frequency constituents are unresolved and aliased in

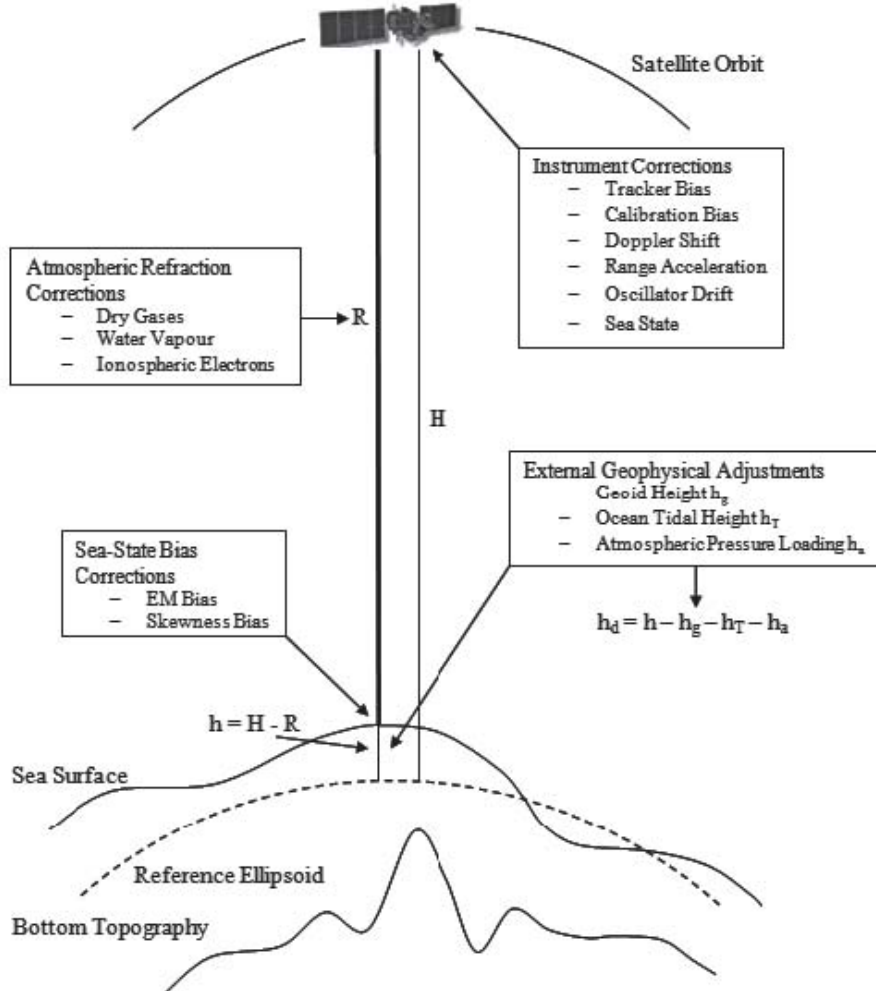


Figure 2.3: Reprinted from <http://mycoordinates.org/using-satellite-altimetry-to-monitor-and-determine-sea-level/>: schematics of the determination of sea surface height (h) from range (R) and satellite altitude (H).

the altimetry data. [37]

To achieve the dealiasing of tides, as well as to solve the issue of short period ocean response to wind and atmospheric pressure forcing, high resolution regional models are needed, since present global tide models are often not suitable to perform a tidal analysis over coastal and shelf seas. In the literature, there are already examples of optimised regional tidal solutions used in altimetry processing ([38]; [39]). Unfortunately regional tidal models are far from being implemented in several regions of the world.

Global tidal solutions have been computed by several research groups in the last decades. Satellite altimetry data are often assimilated in the underlying math-

ematical models, in order to minimise the difference between the solution of the hydrodynamical equations and the available observations (see for example [40] for the TPXO model) . A comprehensive review and evaluation of the accuracy of the global tidal models is available in [41].

Global tidal models are used in the following chapters to derive the SSHA: Their validity is tested against in-situ data and the effect of the aliasing problems is assessed in the derivation of sea level periodicities (see chapter 5).

2.4.2 Wet tropospheric correction

The wet tropospheric correction takes into account the refraction due to water vapour in the troposphere. It is traditionally calculated from onboard microwave radiometers, but it is not reliable in the coastal zone: on Envisat, for example, the radiometer 3-dB footprint has a diameter of 21.2 to 22.5 km, depending on the antenna frequency, but the effect of land intrusion in the footprint is already significant at 30-50 km from the coast in terms of the error it induces on the correction [42, 43].

The first way to overcome the limitation of having a large radiometer footprint is by simply avoiding the usage of radiometer data near the coast. [44] has been a pioneering study and a first attempt whose algorithm was largely based on data recovery through interpolation. [45], studying the surface circulation around Cape Verde region through merged Topex/Poseidon and ERS-2 altimeter data, made one of the first attempt to apply a coastal dedicated correction. Following studies have replaced the radiometer information with modelled data from the European Centre for Medium Range Weather Forecasting (ECMWF) [6]. This strategy proved very useful, although resolution problems emerge: the ECMWF temporal resolution is 6 hours, but the tropospheric water content can vary at shorter temporal scales, while the maximum spatial resolution (from the operational model) is $0.12 \times 0.12^\circ$, i.e. smaller than the satellite resolution [46]. [47] proposed a method applied to Jason-1, where the algorithm of the standard retrieval of wet troposphere delay from the radiometer is modified by parameterizing the coefficients as a function of the land fraction, whose contribution is determined by simulated coastal temperature brightness values.

One of the most precise corrections has arguably been applied by [48] in the South West European region, reducing the uncertainty on the wet tropospheric delay below 1 cm also in the last 50 km strip. This correction is based on the Zenith Wet Delay (ZWD) values from coastal Global Navigation System (GNSS) stations. Although the coverage is being improved, the benefits of this method are nevertheless compromised in regions like Africa, where GNSS stations are hundreds

of kilometres far from one another.

This research led to the GNSS-based Path Delay (GPD) wet tropospheric correction, which is applied in this study in chapter 5. The GPD correction has been produced as part of the ESA Sea Level Climate Change Initiative (SL_cci) project [48]. It combines the ZWD from GNSS measurements at inland coastal stations with the valid values of Wet Tropospheric Correction computed from the Microwave Radiometer on board the satellites and with the output of a numerical weather model. It is fully compatible with the microwave radiometer based correction (used in the open ocean) and guarantees consistency in the transition from open ocean to the coastal zone. More detailed description and validation of the results is found in [48].

2.4.3 Sea state bias

The sea state bias (SSB) correction compensates from the fact that the estimated sea level is lower than the truth due to the way the large radar footprint interacts with a wavy surface. In particular, part of the correction is needed because the radar cross section, i.e. the surface intercepted by the transmitted signal, is larger toward the wave troughs and smaller toward the crests [49], while the rest is attributable to tracker-related biases (see [9] for details). In standard altimetry, a good approximation accounts for a sea state bias on the order of the 4% of the estimated SWH, although models and coefficients vary slightly depending on the mission (see [36] for a comprehensive list). Throughout this study, the correction given in the SGDR product is used, although for future perspectives a new computation of the SSB using the ALES algorithm described in this thesis should be taken in consideration to improve the correction in the coastal zone. Only for Cryosat-2 data (sections 2.6 and 6.2), due to the fact that at the time of writing a proper SSB algorithm for the mission has not yet been implemented, a tentative SSB correction equal to 4% of the wave height has been adopted.

2.5 Sea level in the coastal zone

Sea level is a fundamental climate variable needed to understand the way the ocean interacts with climate fluctuations, and as such has been included in the Global Climate Observing System (GCOS) list of Essential Climate Variables (ECVs). Benefiting from multiple altimetry missions, oceanographers have been able to describe global sea level variability and long-term trends. However as it has been said, the confidence in altimetry data decreases towards the coast. Along the coastlines, the

most reliable and frequent measurements come from tide gauges (TGs), but their coverage is not global and they do not provide a description of the changes that intervene between coast and open ocean. To the best knowledge of the author, there are no published studies that have attempted the use of a specialised retracked dataset to perform an analysis of the sea level variability in the coastal ocean with satellite altimetry.

Up to now, researchers have focused in particular in comparing the trends of sea level derived from TGs and open ocean altimetry. Generally, it has been found that on a global scale there is no significant difference between coastal and global mean sea level rise, but the coastal mean sea level trend has larger interannual variabilities, probably due to regional effects mainly caused by the ENSO [50].

This research deals in particular with one of sea level's most prominent periodic variations: the annual component, which is affected both by steric effects (changes in water density) and mass variations. The amplitude and phase of the annual cycle are related to the seasonality of a wide range of phenomena: warming/cooling of sea water, precipitation, rivers runoff, seasonal atmospheric processes and ocean circulation [51, 52]. Measured annual cycle amplitudes range from a few centimetres to almost 30 cm depending on the region of the world [53]; the phase therefore has an important effect during extreme sea level events, when storm surges combine with tides and mean sea level.

The steric contribution to the annual sea level signal is known to be prevalent in the deep ocean, while in coastal regions complex bathymetry, local circulation and forcing from rivers, atmosphere and wind can be more significant. The variables that affect the annual cycle are often characterised by strong spatial gradients in coastal regions and previous studies have demonstrated that the annual cycle characteristics can change from open ocean to coast [54]. Moreover [55] demonstrated that the consistency between TGs and standard altimetry estimations of the annual cycle varies considerably depending on the regions. Coastal sea level variability is therefore the most challenging to interpret, and also to measure.

2.6 Innovations in satellite altimetry

Considering the new altimetry missions, there are two main technical improvements that can enhance the coastal capabilities for sea level determination: the use of Ka-band and the Delay-Doppler (also called "SAR") altimeters. Both of them are characterised by better noise performances and smaller footprint, which are beneficial for coastal applications.

AltiKa, launched in February 2013, is the first Ka-band altimeter, operating at 35.75 GHz, with a pulse repetition frequency (PRF) of 3700 Hz (providing mean waveforms at 40 Hz, i.e. every 174 m along track). While standard altimeters have been set on Ku-band, Ka-band now allows a larger bandwidth providing a smaller footprint radius (\sim 4 km) [56]. This characteristic guarantees that more independent echoes can be averaged to produce more precise estimations, hence the higher PRF. The drawback of the use of Ka-band is the higher sensitivity to atmospheric conditions, particularly the attenuation of the signal due to rain, but recent studies have shown that this impacts less than 0.1% of data [57].

The Delay-Doppler altimeter is used on Cryosat-2 (CS-2) mission and will be used on Sentinel-3. It sends pulses with a high PRF in order to achieve pulse-to-pulse coherence. Each resolution cell in the along-track direction is characterised by a Doppler frequency that can be exploited using the phase information of the complex echoes that return to the satellite. In this way, a higher number of independent looks can be referred to a reduced footprint (pulse-Doppler limited footprint), which is effectively beam-limited (\sim 200 m in the along-track direction) if compared to the classic pulse-limited shape of the standard footprint, as shown in figure 2.4 [1]. Across-track, the left-right ambiguity of the received echo is still present, since for a relatively homogenous surface (such as the oceanic footprint illuminated by the satellite) the power of each range resolution cell corresponds to the signal received at the same time from both sides of the footprint, which lie at the same distance from the receiver.

Finally, it is worth mentioning the planned SWOT mission (year of launch: 2020), which will carry two SAR antennae and a nadir-looking altimeter that will measure simultaneously, allowing the usage of interferometric techniques. The promised intrinsic SAR resolution of a few meters could describe even sub-mesoscale dynamics in the coastal ocean [58].

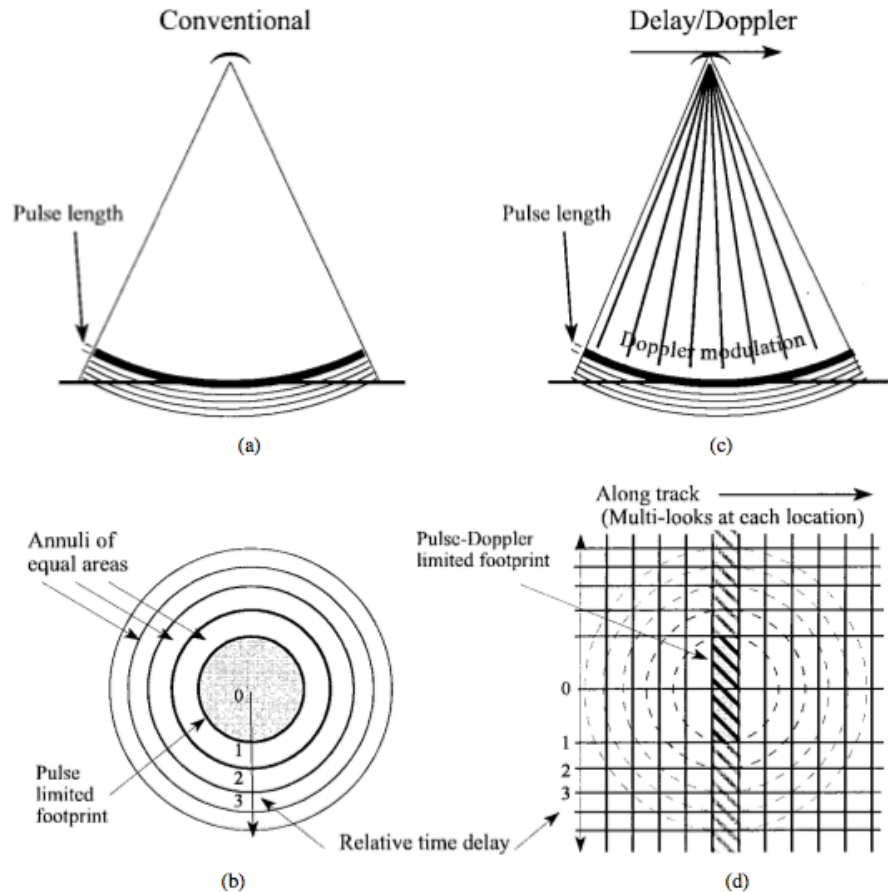


Figure 2.4: Reprinted from [1]: Comparison of a conventional pulse-limited radar altimeters (a) illumination geometry side view and (b) footprint plan view, to a Delay-Doppler altimeters (c) illumination geometry side view and (d) footprint plan view. The conventional radar altimeter measurement space is inherently 1-D, whereas that of the Delay-Doppler altimeter is 2-D.

Chapter 3

Concept and design of an innovative retracker

3.1 Mathematical model and estimator

In section 2.3 it was shown that bright targets appear in the tail of the altimetric waveforms in the coastal zone, making them significantly different from the Brown model, which tries to fit a slowly decaying trailing edge to the real waveform.

This chapter aims at presenting a retracker that overcomes these difficulties and can be applied both over open and coastal ocean without discontinuity: the Adaptive Leading Edge Sub-waveform (ALES) retracker. ALES represents an evolution of the family of the sub-waveform retrackers, in that it adapts the width of the sub-waveform according to the SWH, while still adopting the Brown-Hayne theoretical ocean model. ALES is designed in order to maintain the same degree of precision both in open ocean and along the coasts. As it will be demonstrated, ALES performs only marginally worse than the Brown-Hayne retracker over waveforms that comply with the Brown-Hayne model, but it outperforms the Brown-Hayne retracker for the vast majority of open ocean waveforms affected by bright targets, as well as in coastal waters. One of ALES strengths lies in the fact that it does not involve any change in the retracking method, hereby avoiding any source of potential internal bias. It succeeds in retracking waveforms where the trailing edge is contaminated, but a distinct leading edge is still observable.

The rationale for ALES comes from recent studies on leading edge retrackers, but also from concepts deeply embedded in the design of the first altimetric missions. The tracker system designs of the SEASAT, GEOSAT and TOPEX missions, while using the rising leading edge as the basis of precise height measurement, estimated the height error (degradation of measurement precision with increasing wave height)

using a number of gates increasing with increasing wave height [59]. The variation in width of the fitting window with SWH makes ALES widely applicable to different environmental conditions as it will be shown in chapter 4 over two regions with very different sea state. Morevoer ALES is applicable to waveforms from different altimeters, as this research shows with data from Envisat, Jason-1, Jason-2 and AltiKa.

The model in equation 2.1 is fitted to the real signal in order to estimate the parameters of interest. [9] suggested the use of least squares rather than maximum likelihood estimation (MLE), because the latter assigns too much weight to portions of the waveform with low signal power, and is therefore unreliable due to unmodeled errors in the waveform samples. For Envisat, Jason-1 and Jason-2 the optimal parameters are found at each iteration by developing the total cost function in a Taylor series at first order, which involves the computation of weighted partial derivatives; the method is also known as minimum mean square estimator (MMSE) [16, 60].

ALES adopts an unweighted least-square estimator whose convergence is sought through the Nelder-Mead (NM) algorithm. NM is a simplex optimization method that does not use the derivatives of its cost function, whilst it searches for the minimum in a many-dimensional space. Specifically, considering m parameters to be estimated, given that a simplex of dimension m is a polytope of the same dimension and with $m+1$ vertices characterised by $m+1$ cost function values, NM generates at each step a new point whose cost function is compared with its value at the vertices. If it is smaller, the point becomes a vertex of the new simplex and a new iteration is generated [61]. Convergence is reached when the diameter of the simplex is smaller than a specified tolerance, set at $1 \times 10^{(-10)}$ in this study. For ALES, 600 is the maximum number (Nmax) of iterations allowed to reach the tolerance. As already demonstrated in [32], the method is also very effective in terms of speed: the average time needed to process each oceanic waveform with the MATLAB code generated for ALES is of the order of 0.1 seconds; the drawback of avoiding a waveform classification is that it can take up to a few seconds for each waveform where no clear leading edge is detectable, such as on land.

Previous studies such as [62] have shown the properties of NM, and [32] examined the root mean square error in the parameter estimation for Brown retracking and found better performances compared with the Newton-Raphson strategy, which is also an iterative method based on the derivatives such as MMSE. The downside is that NM does not provide the Fisher information matrix to assess the confidence interval of the fitted parameters, nevertheless an evaluation can be performed by

comparing the reconstructed waveform with the original returned echo [32].

3.1.1 ALES rationale

The retracking choices that have paved the way to the ALES concept and, in particular, the novelty of ALES compared to similar strategies (mentioned in section 2.3.1), are here discussed more in depth. The first choice to be made was whether opting for a modification of the Brown model or choosing a numerical method. In order to guarantee the comparability with the standard open ocean products and the homogeneity between open ocean and coastal approach, the first was chosen. Two of the most up-to-date methodologies were implemented and tested: the “Brown+Gaussian Peak” (BGP) and the “OceanCS” retracker [25, 26]. The implementation revealed how BGP was able to capture the peak in the trailing edge, but this was not always sufficient to fit the leading edge appropriately, as shown in the example of figure 3.1. The addition of multiple and/or asymmetric peaks in the waveform model would have significantly increase the amount of unknowns, moreover the number of needed peaks is unclear due to the complexity of coastal waveform. The “OceanCS” method showed significant fitting capability and therefore the subwaveform strategy was chosen as starting point of the design of a new retracker. The weaknesses of a pure leading edge retracker such as “OceanCS” are described subsequently.

Once a choice for a subwaveform retracker has been made, there are several ways to choose the width of the window to be fitted. Both [26] and [25] chose to carefully select the leading edge location, using an algorithm that ALES partially inherited. The “OceanCS” retracker described in [26], which essentially constitutes the first pass of ALES, does not go further than the end of the leading edge. This choice guarantees to maximise the number of retrievals, but the leading edge could be tracked even when the perturbation of the bright target is on it and the estimated parameters would be significantly noisier than the ones estimated by a full-waveform algorithm (as shown in figure 3.3). The algorithm in [25] goes a step further and defines the optimal number of gates of the fitting window. Nevertheless, this is computed only for one value of the sea state. The innovation of ALES lies in choosing this width depending on the sea state by means of a linear relationship, which is what is missing in the PISTACH strategy, which makes use of three pre-fixed subwaveforms [33]. In fact, up to ALES there has been no connection between the noise of the estimation and the width of the subwaveform to retrack, leading to variable performances compared to a standard full waveform strategy.

A possible addition for ALES could have been the use of different fitting models

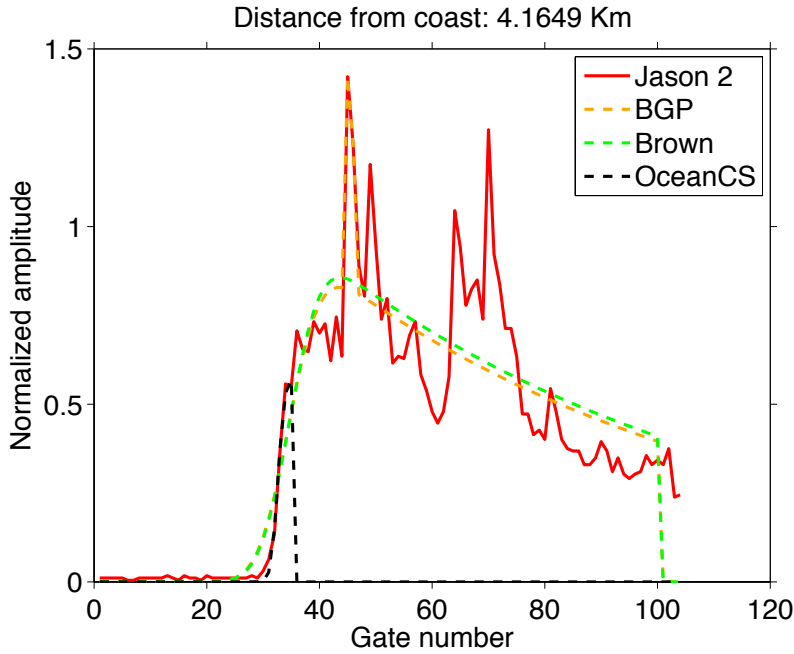


Figure 3.1: Example of a coastal waveform from Jason, fitted by the BGP, the OceanCS and the Brown algorithm implemented in MATLAB.

to be applied to the chosen subwaveform. Certainly, the use of a threshold retracker would have lead to a higher number of retracked waveforms, in particular in the last three km from the coastline, where waveforms often have multiple leading edges that hardly conform to the Brown model. Nevertheless, the use of different retrackers depending on the kind of waveform would have compromise the aim of the ALES strategy, which is to guarantee a stable retracking precision in the transition from open ocean to coast and to provide the users with a product that is easily comparable to the standards.

3.2 ALES strategy

Initially, each waveform is normalised by the maximum value of an 8-point average computed at each gate. Then, ALES performs the fitting in two passes; first it detects the leading edge of the waveform, as explained in 3.2.1 below, and computes a first estimate of τ , SWH and σ^0 by fitting the model in 2.3.1 to the leading-edge; the SWH value is used as explained in 3.2.2 to select a SWH-dependent subwaveform window on which to perform a more precise estimate of the three parameters in the second pass of the algorithm. A flow diagram of the main steps followed by ALES

to retrack each waveform is shown in figure 3.2. For brevity we will refer to the start gate number and end gate number of the sub-waveform window as the startgate and stopgate, respectively. A subwaveform will therefore be defined as the part of the waveforms whose first and last gates are identified by startgate and stopgate.

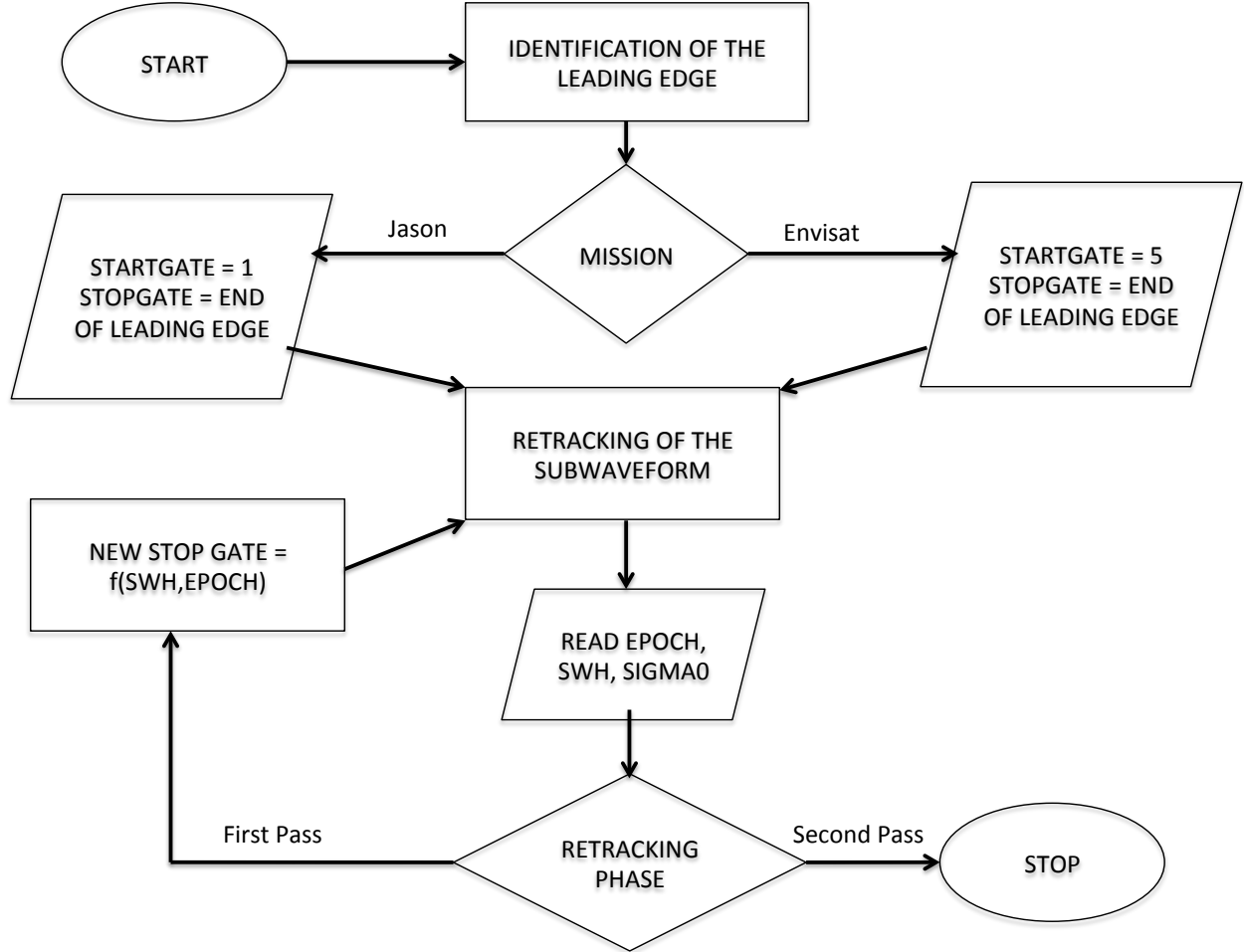


Figure 3.2: Flow diagram of ALES retracking procedure for each waveform. Startgate and stopgate refer to the starting gate number and end gate number of the sub-waveform window.

3.2.1 First pass: leading edge detection and fitting

The first estimation is performed on a window that includes the leading edge of the echo, entirely excluding the trailing edge.

Thermal noise is estimated from an average of the first few gates and removed from the signal. For Envisat, gates 5 to 10 are chosen, since the first gates are affected by aliasing due to the application of a digital filter that wraps around the

high frequency components of the received pulse into the low frequency waveform samples. In Jason-1 and Jason-2, the first and the last gates are already excluded from the waveforms (104 gates are given, rather than the full 128 as in Envisat), therefore we estimate thermal noise from the average of gates 1 to 5. For the same reason, ALES startgate is gate 5 for Envisat and gate 1 for Jason-1 and Jason-2.

The main leading edge detection is based on the difference between consecutive gates. The algorithm searches for the beginning of the leading edge (edge foot): this is taken to be the first gate where the difference of two consecutive gates is positive and greater than 1% of the normalization factor, i.e. when:

$$Dwf > 0.01 \quad (3.1)$$

where Dwf is the vector containing the differences between consecutive gates and numbers are expressed in normalised power units. The 1% threshold is arbitrary and it is defined to detect the reception of a return echo.

Then the algorithm finds the end of the main leading edge (edge top) at the first following gate where the difference of consecutive waveform values becomes negative, i.e. when:

$$Dwf < 0 \quad (3.2)$$

The stopgate for this first pass is taken as the edge top gate plus one. Due to noise, the exact location of the end of a leading edge is not precisely defined in a waveform. This can lead to a problem of inaccuracy in the case of a simple leading-edge retracker. However, the stopgate is here only used to define the subwaveform for the first estimation of Epoch and SWH, whose final values are the result of the second estimation, which is independent of the stopgate.

Small targets preceding the true leading edge (such as those due to ships) can be detected as the leading edge of a waveform. They are characterised by a very narrow return with low power compared to the signal reflected by the ocean surface. To avoid erroneous detections, edges whose power drops below 10% of the normalisation factor within 4 gates from the edge top are excluded.

The subwaveform is then fitted as in section 3.1. When convergence is not reached in N_{max} iterations, the estimation window is widened by increasing the stopgate (i.e. widening the window by one gate towards the waveform tail) until convergence is reached.

Epoch and SWH from the leading edge sub-waveform estimation are then used to select a wider sub-waveform for the second pass.

3.2.2 Second pass: selection of sub-waveform and precise final estimation

For best accuracy the subwaveform width for the second pass must be optimised such that it fully includes all gates comprising the leading edge, but with minimal contribution from the trailing edge, where artefacts such as bright target responses may prevent equation 2.1 from accurately describing the shape. In effect the issue is one of defining an appropriate stopgate for the second pass retracking based upon the SWH estimates from the first pass. The relationship between SWH and stopgate was derived from Monte Carlo simulations. For each value of SWH ranging from 0.5 to 10 m in steps of 0.5 m, 500 high-rate waveforms were simulated with the model described in section 2.3.1 adding realistic Rayleigh noise. The resulting waveforms were retracked using the classic Brown-Hayne model over the entire waveform, and then over sub-waveform windows with startgate=1 and variable stopgate, and the RMS errors (RMSE) computed.

The difference of the RMSEs between the "full waveform" estimate and the sub-waveform estimates is displayed in figure 3.3 as a function of the stopgate position. Upper left, upper right and lower left panels show the results for Epoch, SWH and amplitude estimation. The x axis is, in practice, the width of the sub-waveform, expressed as number of gates from the tracking point to the stopgate. The results for each SWH level are coded in different colours. For all three parameters, the curves converge asymptotically to the full waveform estimates, as expected for this idealised case of "pure-Brown" response of the ocean surface. The amplitude is the parameter that needs the smallest amount of gates to be properly estimated - and indeed in some cases its estimate can be marginally more accurate by discarding part of the tails, as indicated by the positive difference of RMSEs. Epoch and SWH estimations show similar patterns, although the curves are less smooth for the SWH. This is also expected, since SWH retrieval is normally noisier in the retracking of real waveforms. In the lower right panel, a linear relationship is derived between SWH and the number of gates needed using a 1 cm RMSE tolerance compared to the theoretical precision of a "full waveform" estimation. The choice of the 1 cm tolerance is a trade off between retaining an "open-ocean" level of precision and avoiding perturbations in the trailing edge. We consider 1 cm a good compromise since it is much less than the estimated noise on high rate range measurements found

in previous studies on Jason-1, Jason-2 and Envisat [63, 64].

The parameters h , θ_0 and σ_p change depending on the mission. Therefore the same Monte Carlo simulation was run for both Envisat and Jason, resulting in slightly different coefficients of the linear relationship derived (figure 3.3 refers to Envisat) . From these results, the stopgate of the ALES estimation window is calculated using the following equations:

$$\text{Maximum gate} = \text{Ceiling}(\text{ Tracking point} + 2.4263 + 4.1759 \times \text{SWH}) \quad (3.3)$$

for Envisat and

$$\text{Maximum gate} = \text{Ceiling}(\text{ Tracking point} + 1.3737 + 4.5098 \times \text{SWH}) \quad (3.4)$$

for Jason-1 and Jason-2.

where tracking point and SWH are from the first pass. The final estimation of the three parameters τ , SWH and σ^0 is made from this window width at the second pass.

Examples of three typical fittings of real waveforms (blue line) by ALES (dashed red line) are provided in figure 3.4 for open ocean with low SWH, coastal ocean with corrupted trailing edge and open ocean with high SWH.

3.2.3 Mispointing angle

Every radar altimeter has a degree of inaccuracy in pointing perpendicular to the ocean surface. The slope of the trailing edge in the theoretical Brown functional form depends on the mispointing angle, which measures how much the antenna pointing deviates from nadir. The most significant effect is in the estimation of the signal amplitude, reducing the apparent backscatter coefficient [65, 66].

In its current version, ALES does not estimate mispointing. Values are taken from the SGDR products. In standard three-parameter retracking, such as for Envisat, the angle is computed from the slope of the logarithm of the trailing edge [67]. In the current version of Jason-1 and Jason-2 SGDR, the mispointing is estimated in the retracking process (from the MLE4 retracker) together with Epoch, SWH and amplitude. We use this output as input for our three-parameter model, and this should not influence the correct range retrieval for angles smaller than 0.3° [68]. Where no estimate from the SGDR is available, for example where SGDR retrack-

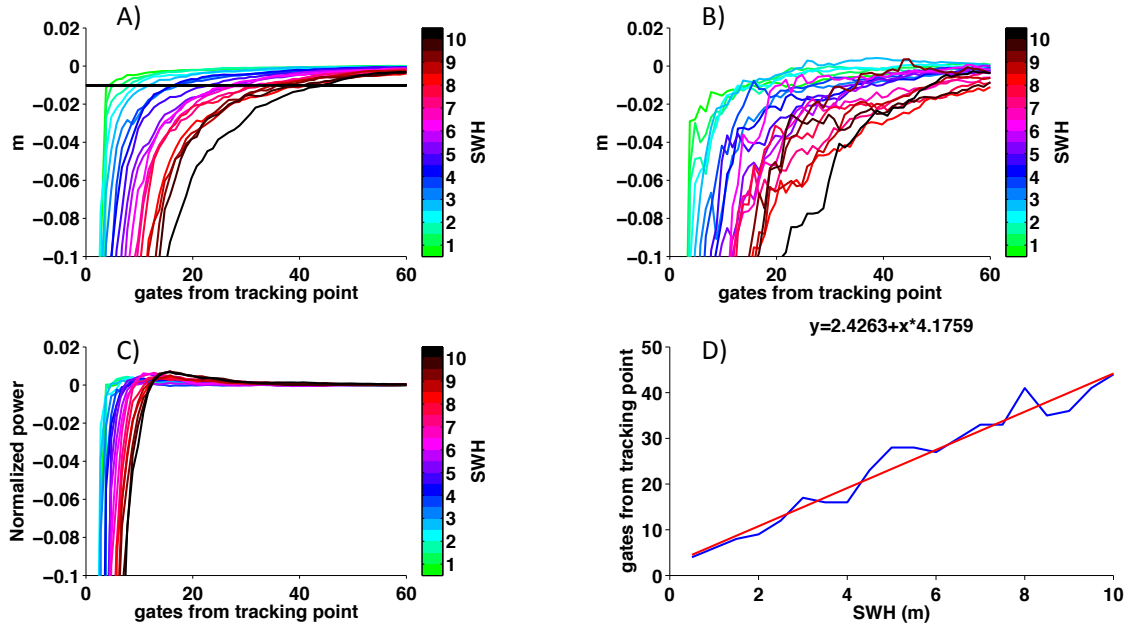


Figure 3.3: Monte Carlo simulation (500 waveforms \times gate \times SWH value) using Envisat parameters. From upper left to lower right: RMSE difference between Brown full-waveform and subwaveform retracking at different SWH for A) Epoch, B) SWH and C) amplitude estimation; D) relationship between SWH and number of gates needed to estimate the Epoch with a 1 cm tolerance w.r.t. the full subwaveform retracker.

ing failed, we take the last valid measurement. The mispointing values are then smoothed over 3 seconds. These are reasonable approximations considering that [67] suggested that a smoothing over 30 seconds should be applied when mispointing is calculated from the waveform. It is therefore appropriate to always smooth the value for the mispointing to avoid features in the trailing edge affecting ALES performance through the mispointing values used.

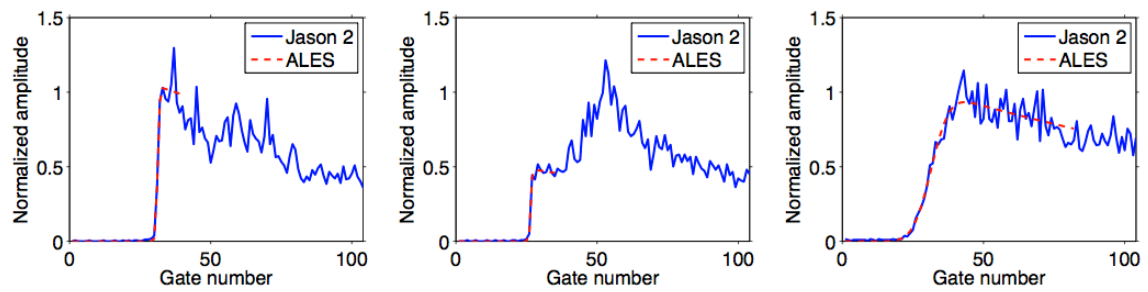


Figure 3.4: Examples of ALES retracking of Jason 2 waveforms for open ocean with $\text{SWH}=0.75 \text{ m}$ (left), coastal ocean with corrupted trailing edge (centre), open ocean with $\text{SWH}=9.48 \text{ m}$ (right).

Chapter 4

The retracking strategy: ALES validation

4.1 Methods for validation

This chapter presents a regional validation of ALES range and SWH retrievals, performed in coastal areas with different characteristics and considering in-situ data as the ground truth, i.e. tide gauges (TGs) for sea level and buoys for SWH. The validation is performed by comparing the time series of Total Water Level Envelope (TWLE) and SWH generated along consecutive satellite passes with the time series generated by in-situ measurements in the locations described in sections 4.2.1 and 4.3.1.

To create an altimetric time series, data points along the satellite tracks need to refer to the same geographical location along-track for all cycles. The altimeter data from SGDR and ALES for each cycle were therefore linearly interpolated along the nominal tracks defined by the Centre for Topographic studies of the Ocean and Hydrosphere (CTOH) and available from <http://ctoh.legos.obs-mip.fr/altimetry/satellites>, neglecting the across-track displacement of different passes along the same track, which is normally less than 1 km.

The difference between ALES and SGDR retrievals and in-situ measurements is analysed in terms of correlation, mean bias and standard deviation (std) at the point nearest to the in-situ data and at all other points along-track. For the along-track correlation analysis, a new statistics is introduced with the aim of determining for each latitude-longitude location the maximum percentage of cycles of data that could be retained whilst guaranteeing a correlation with the in-situ time series of at least 0.9. The test is performed in an iterative way: first of all for each location the correlation of the in-situ time series with the entire set of altimetry retrievals

is checked; if the correlation coefficient is lower than 0.9, then the cycle with the maximum discrepancy (quantified as the maximum of the absolute value of the difference) between in-situ value and altimeter retrieval is excluded. This exclusion is iterated until the correlation rises above 0.9, at which point the percentage of cycle left indicates the general quality of the retracked altimetry values against the available SGDR product and will be referred to as the Percentage of Cycles for High Correlation (PCHC) throughout the following sections.

To check the data quality of range retrievals in section 4.2, the variable that is extracted for the comparison with the TGs is the Total Water Level Envelope (TWLE), defined as:

$$\text{TWLE} = \text{Orbit altitude} - \text{Corrected Range} - \text{Mean Sea Surface} - (\text{Solid Earth Tide} + \text{Load Tide}) \quad (4.1)$$

where

$$\begin{aligned} \text{Corrected Range} = & \text{Range} + \text{Instrumental corrections} + \text{Dry tropospheric correction} + \\ & \text{Wet Tropospheric Correction} + \text{Sea State Bias} + \text{Ionospheric correction} \end{aligned} \quad (4.2)$$

TWLE represents the combined effect of ocean tides and atmospheric forcing in addition to the sea level anomaly with respect to the mean sea surface. It is therefore particularly useful for applications that need an estimate of the total sea level above the mean, such as the analysis of storm surges.

To check the data quality of SWH retrievals in section 4.3, the effect of the two different values of σ_p described in section 2.3.1 for Envisat is tested on ALES estimations. Moreover, using the estimates of SWH^2 available in the SGDR product (only for Envisat), an adjusted SGDR SWH field is generated with $\sigma_p = 0.53r_t$, where r_t is the time resolution of each waveform gate, through the following relationship:

$$SWH_{corrected} = \sqrt{SWH^2 + [(0.6567r_t)^2 - (0.53r_t)^2](2c)^2} \quad (4.3)$$

Any described statistics that involves a comparison with an external source (such as tide gauges) is here intended as a validation technique. The verification of the altimetry datasets, which involves statistics that do not rely on external input, is provided in section 4.2.6.

4.2 ALES sea level validation: Adriatic Sea and Mossel Bay

4.2.1 Dataset and area of study

Two areas of study were selected to verify and validate ALES sea level estimations: the Gulf of Trieste, in the North-West Adriatic Sea, and Mossel Bay, along the Indian Ocean coast of South Africa. The areas are representative of two different morphological and oceanic conditions.

The Gulf of Trieste is a small shallow bay with average depth: 17 m, maximum depth: 25 m and width: 20 km. The maximum tidal amplitude is 81 cm [69]. The cyclonic gyre (anticlockwise) that characterises the main circulation is induced by currents flowing northwards along the Istrian coast and is modulated daily by the local wind field [69]. The rest of the Northern Adriatic basin is also a shallow sea, less than 100 m deep. It is characterised by a weak cyclonic circulation that reaches peaks of 25 cm/s along the Italian coast of its western boundary [70].

Wind strength and direction is particularly important because of its influence on the sea surface roughness. The most important wind in the Gulf of Trieste in terms of frequency and intensity is called the Bora (from East-North-East), with further contributions to atmospheric circulation from Scirocco (direction South-East to South-South-West) and breezes from land and sea. The Bora is a strong katabatic wind which can reach speeds of over 10 m/s, especially during autumn/winter and has an annual mean velocity of 6 m/s (compared to 2.1 m/s for the other winds in the region) [71].

Mossel Bay is a much more open 25 km wide gulf, affected by the large circulation features of the South African coast. From the coast, the Agulhas Bank extends for roughly 200 km with depths that do not exceed 200 m and near-surface currents in the range of 0-0.5 m/s. Then the continental slope is found, where the prevailing westward warm Agulhas Current reaches velocities of 2.50 m/s and the depth rapidly reaches over 4000 m [72]. The amplitude of spring tide reaches 2.40 m [73]. Wind forcing is particularly important along the coast and influences the surface currents of the bank. Easterly winds prevail in the summer, causing coastal upwelling, while westerly winds predominate in winter [74].

In these two locations, waveforms from 5 tracks from 3 different altimetry satellites were retracked with ALES. The waveforms are provided as part of the SGDR product for each mission, which also includes the level 2 geophysical estimates of height, SWH and wind based on the Brown-Hayne retracker, together with atmo-

spheric and geophysical corrections to be applied to the data. They are distributed at 18 Hz rate for Envisat and 20 Hz rate for Jason-1 and Jason-2, representing a measurement every 300-350 metres.

The DTU10 mean sea surface [75] was subtracted from the retrieved sea surface height for all the tracks. In order to compare the altimeter data with the TGs, the effect of atmospheric pressure on the sea level was not applied to either ALES or SGDR dataset [76]. While Envisat and Jason-1 SGDR provide estimations of the range from a single oceanic retracker, the latest version of Jason-2 gives two estimations for each waveform, coming from MLE3 and MLE4 retrackers [64]. To be consistent with the comparison with Jason-1, only the MLE4 estimates for Jason-2 are used in this study.

As a reference and comparison, data from CTOH (Centre for Topographic studies of the Ocean and Hydrosphere, <http://ctoh.legos.obs-mip.fr/altimetry>) have been downloaded. In particular, the 1-Hz (a measurement approximately every 7 km) along track altimetry output from X-TRACK processor is used. At the time of this research, data were available for all the tracks except for Envisat pass 687. Data were developed, validated and distributed by the CTOH/LEGOS, France. The X-TRACK processor does not retrack the waveforms; it is a post-processing technique aimed at improving quality and quantity of coastal altimetry measurements through improved tidal and atmosphere forcing correction, data editing and filtering. A detailed description can be found in [77] and [78]. X-TRACK data are widely used and applications already include the Mediterranean Sea [3, 79, 80], the Spanish coast [38, 81, 82], the West Florida Shelf [83], Drake Passage [84] and the Solomon Sea [85].

Two TGs were used for validation of ALES output. They are located at Trieste (PSMSL Station ID 154, Latitude 45.647361° N, Longitude 13.758472° E) and Mossel Bay (PSMSL Station ID 910, Latitude -34.178611° N, Longitude 22.135278° E).

The Trieste TG belongs to the Italian national tide gauge network operated by ISPRA (High Institute for Environmental Protection and Research). The station is equipped with a gauge that records sea level referred to the zero level of the Italian altimetric network. The Italian altimetric network, created by IGM (Istituto Geografico Militare) is the vertical reference (datum) to which all heights are measured around Italy. The zero of the Italian altimetric network is the mean sea level, measured in Genoa during the years 1937-1946 [86]. For the Trieste station, it was possible to refer the sea level measurements to the WGS84 ellipsoid, since the Italian zero level at the TG is estimated to be 44.760 m above it [87, 88]. The sampling

frequency is adjusted to provide data every 10 minutes and/or hourly.

Hourly data for Mossel Bay are distributed by the GLOSS/CLIVAR (Global Sea Level Observing System / Climate Variability and Predictability) fast sea level data service. Since it was not possible to find sources referring those measurements to the ellipsoid, they have been used for relative calibration only.

Figure 4.1 shows the area of study, including the satellite tracks and TGs locations. It is relevant to point out the flight direction of each satellite as it flies over each region, since land-to-sea and sea-to-land transitions might influence the behaviour of the on-board tracker in different ways. In the Adriatic, Envisat pass 416 (Env 416) is a descending (North to South) track, as is Jason-2 pass 196 (J-2 196), while Jason-1 pass 161 in its interleaved orbit (J-1 161) is ascending (South to North). All three tracks cross part of the Gulf of Trieste and fly over the Istrian peninsula. For J-1 161 and Env 416, the stretch of land in Istria accounts for a few km along-track, while J-2 196 flies over the full extent of the peninsula. J-2 196 is particularly challenging because it also flies over Marano Lagoon (classified as inland water), which is less than 3 m deep, and then crosses a 0.5 km wide sandbar before entering the Adriatic Sea [89].

Of the two tracks along the coast of South Africa, Envisat pass 687 (Env 687) is an ascending track, while Jason-2 pass 198 (J-2 198) is descending. J-2 198 flies over the same bay where the TG is located, while Env 687 passes over the other side of Mossel Bay peninsula.

Table 4.1 summarises the characteristics of the dataset and in particular the number of waveforms that were missing from the along-track data and the number of waveforms for which no altimetry parameter estimation was available in the SGDR. The number of missing waveforms is obtained by checking how many times there are no waveforms that fall in the interval between each latitude-longitude point of the nominal tracks. Missing waveforms are more frequent in the Jason missions due to failures of the on-board tracker, an event that particularly occurs near the transition from land to sea [90], which explains why the loss is concentrated in the first 10 km from the coast for the two descending tracks of Jason-2, with up to 70% of data missing for the latitude-longitude points located closest to the coast.

The Envisat altimeter was designed to operate at different bandwidths over different surfaces. The bandwidth preferred for the ocean was 320 MHz, in order to guarantee the highest possible resolution. Nevertheless in the transition zone it can happen that returned echoes are acquired using a different bandwidth. For Envisat data, only SGDR output when operated at 320 MHz bandwidth are considered valid. ALES only retracks these waveforms.

	Env 416	Env 687	J-1 161	J-2 196	J-2 198
Tide Gauge	Trieste	Mossel Bay	Trieste	Trieste	Mossel Bay
Min Dist	11.78 km	10.72 km	8.23 km	30.60 km	13.37 km
Num SGDR cycles	57	58	99	165	126
Num CTOH cycles	56	N/A	77	152	126
Missing wf	325 (2.71%)	0	1483 (4.77%)	5253 (15.45%)	1267 (2.53%)
Missing SGDR	518 (4.32%)	384 (2.74%)	5966 (19.19%)	17653 (51.94%)	2981 (5.95%)

Table 4.1: Data availability for this study. Row 2: the TG to which the tracks specified in each column are compared. Row 3: Minimum distance between the TG and the closest point on each satellite track. Row 4: number of reprocessed SGDR cycles; all the cycles where data in the area were available have been taken into account; the number refers to the number of cycles during which TG data were also available. Row 5: number of CTOH cycles available. Row 6: number and percentage of 18 Hz (20 Hz) along track points where no waveforms from the SGDR of Envisat (Jason) were available. For Envisat, this also includes cases where waveforms were present, but the bandwidth in use was not 320 MHz. Row 7: number and percentage of along track points where no estimation of altimetric parameters was available in the SGDR, despite the availability of corresponding waveforms.

A detailed list of all the cycles reprocessed for each satellite track and the related time interval is provided in table 4.2.

4.2.2 Validation of raw data

The first validation test on the PCHC was performed on all the available along-track range estimations from both SGDR and ALES. The output assesses the general quality of the retracked altimetry values against the available SGDR product. It is important to perform the analysis before any outliers exclusion, in order to quantitatively evaluate whether ALES, compared to standard products, can provide a higher number of accurate estimations at each location. The same analysis was performed for CTOH 1-Hz locations.

Figure 4.2 and 4.3 show the results for the tracks in the Adriatic and the tracks near South Africa. Land areas are shaded in grey. The x-axis represents the along-track progression of each track in latitude. The latitude of the TG is specified by a black dot. Red squares characterise the ALES dataset, while SGDR products are in blue squares and CTOH points are seen as cyan dots. The distance from the closest coastline is specified by a green line which refers to the y-axis on the right.

Env 416 height retrieval is particularly problematic in the gulf area, between

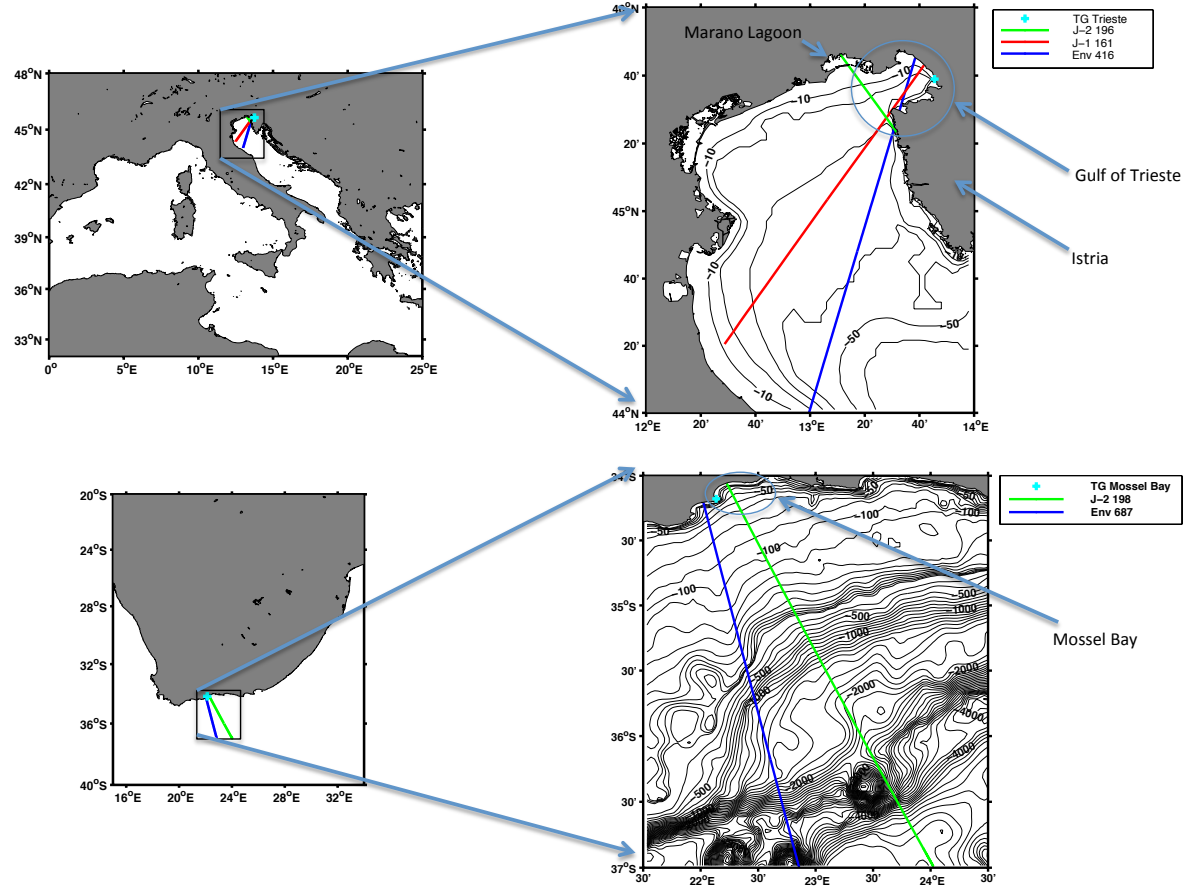


Figure 4.1: The areas of study and the extent of the retracked altimetry passes. Top: Northern Adriatic and Gulf of Trieste. Bottom: Mossel Bay, along the South African coast. Bathymetry is shown by means of contour lines: they are drawn every 10 m.

45.5 and 45.8° N. Here ALES shows improvements particularly in the sea-to-land transition, with over 60% of cycles highly correlated in locations closer than 2.5 km to the coast, where PCHC in the SGDR product decrease significantly. After roughly 3.7 km from the stretch of land in Istria, both ALES and SGDR have more than 80% of PCHC, but along the rest of the track ALES constantly maintains a higher percentage.

The improvement of data quality in the gulf area is even more evident when considering J-1 161. ALES PCHC is constantly well above 60%, a threshold that is hardly overtaken by SGDR in the same locations. Before the Istriian stretch, availability of good ALES data is constantly over 80% of the cycles until 2.5 km from the coast, while the percentage for the SGDR drops below 80% by 7 km from

	Valid cycles	Time interval
Env 416	10 [12,14] 16 19 27 30 [42,45] 47 [49,52] [54,58] [60,72] [74,93]	15/10/02 - 26/09/10
Env 687	[14,17] [19,21] [23,26] 29 31 32 44 45 [47,50] [52,58] [62,73] [75,93]	13/03/03 - 7/10/10
J-1 161	[262,283] [285,292] [295,303] [306,340] [342,349] [351,363] [366,370]	16/02/09 - 23/01/12
J-2 196	[1,165]	19/07/08 - 31/12/12
J-2 198	[1,8] [12,14] [18,30] [32,35] [37,42] 45 46 [48,80] 82 83 [85,91] [95,100] [102, 109] [111,132] [138,146]	19/07/08 - 26/06/12

Table 4.2: List of cycles. Column 2: list of the cycles used in this study for each satellite track. Cycles where satellite data were missing and/or coincident TG data were not available have been excluded. The squared brackets indicate a closed interval between the two endpoints. Column 3: time interval in day/month/year format.

the Istrian peninsula. For both J-1 161 and Env 416 in the Gulf of Trieste, CTOH had no data for any cycle. The first available measurements are situated more than 10 km along-track from the Istrian peninsula and several cycles contained empty data, as evident by the low percentage in the figure.

Along the descending J-2 196 track, ALES retrieves more than 80% of highly correlated cycles within 7 km along-track from the islet that marks the beginning of the lagoon (visible on the plot as a dashed black vertical line), while the SGDR data take 13 km (along-track distance) to get to a comparable level. It is particularly striking how ALES is also able to capture more valid data also inside the lagoon, showing that ALES could potentially be used for inland water sea level measurements.

In the tracks that pass over South Africa, which fly over a wide open ocean area, the results for SGDR and ALES are extremely similar. Nevertheless the performances of SGDR slightly decrease at 11 km from the coast, while ALES points are highly correlated to within 1.5 km. Along J-2 198, the parallel degradation of the two datasets in proximity to the coast is explained by failure of the Jason on-board tracker, an event that particularly occurs in the transition from land to sea [90].

4.2.3 Outlier detection

In order to further analyse the correlation and the RMS between in-situ sea level observations and ALES estimations, outliers have been detected and excluded. Validity does not imply accuracy and therefore the number of valid points does not correspond to the total number of "correct" estimates; nevertheless the outlier detection is applied to exclude extreme values of ALES output which would alter the

correlation and RMS analysis performed on the full time series.

For the sake of comparison, the same flagging criteria have been used for both SGDR and ALES data. It is preferable to use separate quality control for each of the three retracked parameters (TWLE, SWH and σ^0) in order to exclude as many poor estimations as possible. Although a flag on TWLE is not suggested in the SGDR and ocean tides are not removed from this quantity, tidal signal is available from the TGs. Therefore a specific flag has been derived for this research taking into account the suggested flag for sea level anomaly in the Envisat product. SWH and σ^0 suggested flagging criteria are the same as the ones used for both Envisat and Jason products [91, 22]. Table 4.3 lists and describes the adopted limits. Since Envisat SGDR product does not provide the high-rate values of SWH and σ^0 , only the flag on TWLE could be applied.

Figures 4.4 and 4.5 show the along-track distribution of outliers in the two considered regions. The most problematic area is the Gulf of Trieste and the reason lies in the fact that a large part of these tracks is closer than 10 km from the coastline (with multiple transitions from land to sea and sea to land), where the majority of

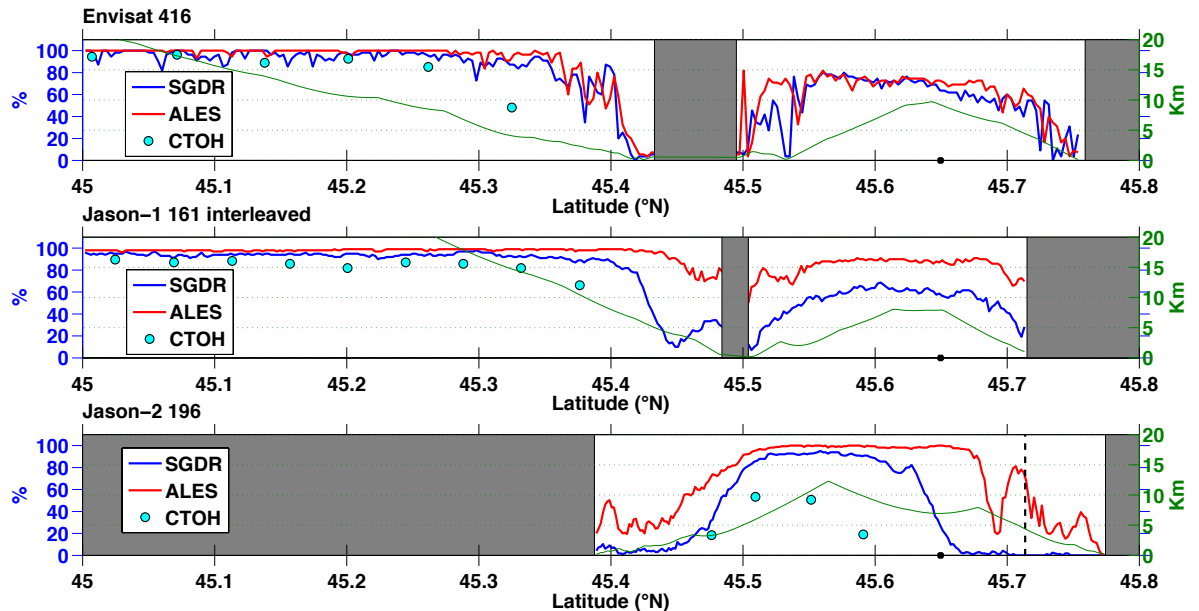


Figure 4.2: North Adriatic: PCHC for Env 416 (top), J-1 161 (centre) and J-2 196 (bottom). On the x-axis the along-track latitude of the nominal tracks are shown. Land is shaded in grey. The distance from the closest coastline is specified by a green line which refers to the y-axis on the right. For J-2 196, the latitude of the islet which separates the gulf from the lagoon is represented by a vertical dashed line.

	Min	Max
TWLE (m)	- 2 - min TG value	+ 2 + max TG value
SWH (m)	0	11
σ^0 (dB)	7	30

Table 4.3: Valid points: minimum and maximum values of TWLE, SWH and σ^0 .

Jason SGDR estimations are outliers. Envisat has the smallest number of outliers among the different missions. It must also be noticed that SGDR in the Adriatic has more valid points than ALES. Considering the low correlation of SGDR (see section 4.2.4) along this track in the locations where the outliers are less than for ALES, it is understood that some of the SGDR poor estimations are not extreme enough to be eliminated by the outliers detection.

Since in Jason missions the outlier detection can be extended to SWH and σ^0 , this comparison is assumed to be more meaningful. In J-1 161 ALES succeeds in keeping the outliers below 25% even very close to the coastline, where SGDR exceeds 60%. In J-2 196 the number of ALES outliers is almost always less than the number of SGDR outliers, and between 45.6 and 45.7 °N there are less than 20% outliers,

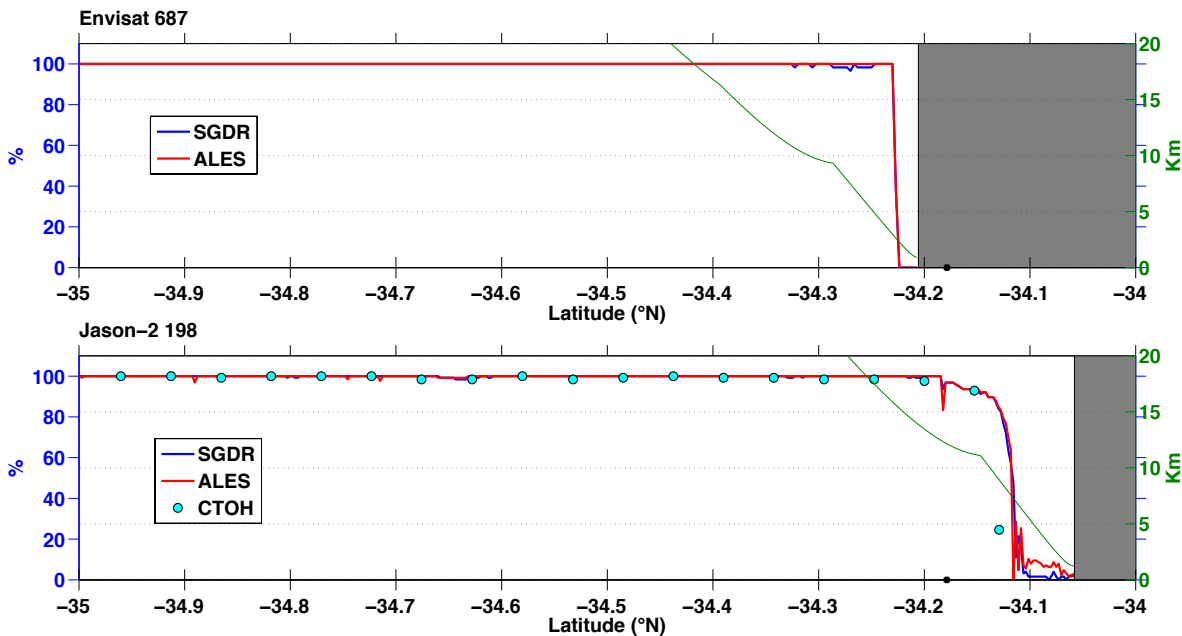


Figure 4.3: South Africa: PCHC for Env 687 (top), and J-2 198 (bottom). On the x-axis the along-track latitude of the nominal tracks are shown. Land is shaded in grey. The distance from the closest coastline is specified by a green line which refers to the y-axis on the right.

whereas SGDR reaches over 60%. In J-2 198 the percentage of outliers rises in the last 6 km from the coastline, at the same pace both in SGDR and in ALES. Here waveforms are highly corrupted and a leading edge is difficult to recognise, as a result of the problematic land-to-sea transition of the Jason altimeter.

It has already been said that erroneous estimations are due to waveforms that do not conform to the Brown model, among which those with a moving bright target in the trailing edge are common in coastal areas, as shown in previous studies such as [32], where waveforms are classified according to their shape. This study argues that the higher percentage of outliers in the Gulf of Trieste compared to Mossel Bay is connected with the shape of the coastline and its influence on the sea state. Depending on wind intensity and direction in the Gulf of Trieste the rugged coastline can create patches of sheltered calm water visible as bright targets in the radargrams, such as the ones of figure 2.2. Further explanation must be found in the analysis of the wind direction, frequency and intensity, but also of the wave height and in the interaction between wind and currents, since all these factors affect the sea surface roughness [92]. Moreover, film slicks on the sea surface are common in the coastal ocean and are mainly related to surfactant accumulation and upwelling fronts [93, 94]. They can extend for many kilometres in calm conditions and create patches of very low surface roughness that can be seen as bright targets in the radar signal. Oil slicks from ships are also to be investigated as a source of highly reflective water: both North Adriatic and South African coasts have high shipping activity, but the slow surface currents of the Adriatic and in particular of the Gulf of Trieste might enhance the permanence of the slicks in that area. Phytoplankton blooms can also have a strong effect, but their signal would be highly seasonal and more sporadic than the observed recurrence of bright targets.

4.2.4 Correlation coefficient

Once the outliers were removed, the correlation between ALES TWLE and TG was computed. For comparison, the correlation coefficient (r) was also computed for SGDR output from the same waveforms. As table 4.1 shows, SGDR data display missing values in locations where waveforms are present. For each location, in order to produce an unbiased comparison, correlation is considered only when both SGDR and ALES estimates are available.

Along-track spatial variation of r for the different tracks is displayed in figures 4.6 and 4.7. ALES improvement in correlation compared to SGDR is widespread. In the open seas, r for ALES is constantly over 0.8, with a few drops that may be due to undetected erroneous TWLE estimations, but may also be due to imprecise

corrections when the drops are seen also in r for SGDR. In the Gulf of Trieste, r for ALES is always higher than for SGDR for distances greater than 2.5 km from the coastline, and it is always above 0.6 for J-1 161 and J-2 196. The low values of r for Env 416 suggest that a more careful quality control of the estimations will be necessary in a post-processing phase; for example, separate quality control of the SWH and σ^0 estimations, which has not been done in this study for Envisat due to the lack of 20Hz estimations in the SGDR product.

Env 687 in South Africa presents a steady high correlation of over 0.9 until within 2.5 km of coastline, but the SGDR data have a significant drop between 10 km and 5 km from the coastline, a degradation that is not seen in ALES data. Along J-2 198 SGDR data also have a drop at 10 km from the coastline, while ALES maintains r above 0.8. ALES presents a single low r value in the open ocean, a closer investigation of this case revealed the presence of a false leading edge, indicating a future area for improvement in the routine described in section 3.2.1.

The comparison with CTOH data is extremely promising: ALES data have the same level of correlation with the TGs despite being a high-rate non-filtered prod-

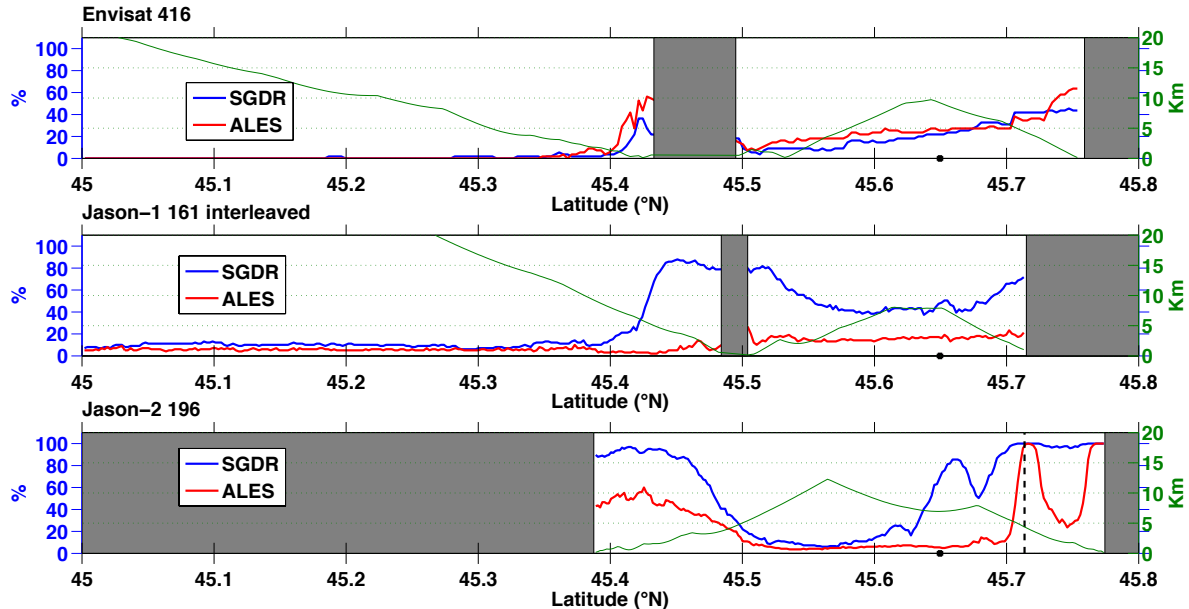


Figure 4.4: North Adriatic: percentage of outliers for Env 416 (top), J-1 161 (centre) and J-2 196 (bottom). On the x-axis the along-track latitude of the nominal tracks is shown. Land is shaded in grey. The distance from the closest coastline is specified by a green line which refers to the y-axis on the right. For J-2 196, the latitude of the islet which separates the gulf from the lagoon is represented by a vertical dashed line.

uct. A higher correlation of the TGs with CTOH 1-Hz data was expected as these data have already been post-processed and therefore outliers have been excluded in the calculation of 1-Hz mean from the 20 Hz measurements. Reaching the same correlation as CTOH values without any filtering or selection means that high rate values with appropriate flagging can be effectively used to produce altimetric data at finer resolutions and in addition in areas where no CTOH output is available, such as the innermost part of the Gulf of Trieste, can still be described by ALES with unprecedented accuracy.

4.2.5 Root Mean Square Difference

The absolute validation against coastal TGs in terms of sea level can help to assess whether the comparability between in-situ data and altimetry is increased by the use of improved retracking strategies. Figure 4.8 shows the RMS of the difference (RMSD) between the time series of the absolute sea level height above the ellipsoid WGS84 (major radius $a=6378137$ m, flattening $f=298.257223563$) for the tracks in the North Adriatic and the equivalent time series at Trieste TG. Since the reference

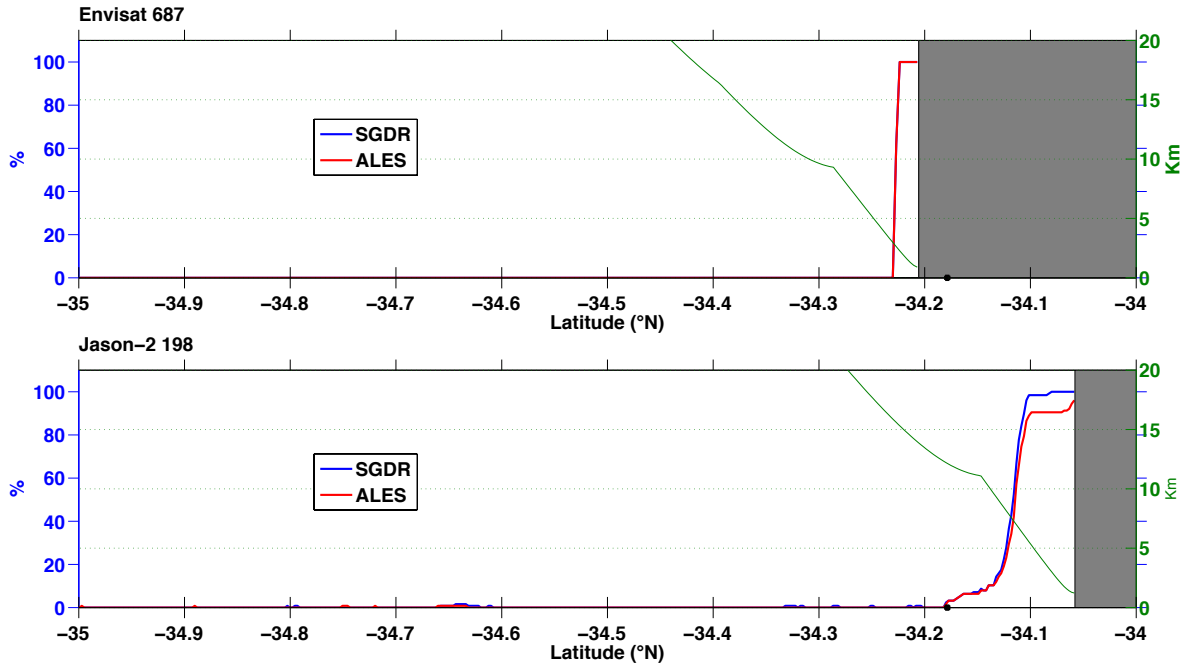


Figure 4.5: South Africa: percentage of outliers for Env 687 (top), and J-2 198 (bottom). On the x-axis the along-track latitude of the nominal tracks is shown. Land is shaded in grey. The distance from the closest coastline is specified by a green line which refers to the y-axis on the right.

ellipsoid of the satellite altitude in Jason and DTU10 mean sea surface is TOPEX ellipsoid (major radius $a=6378136.3$ m, flattening $f=298.257$), values are corrected for the difference between the two ellipsoid models in order to refer each parameter to WGS84. The heights from satellite altimetry are also corrected for the absolute biases found in [95].

Minimum RMSD values are expected to be found using the along-track point nearest to the TG, although this depends on the slope of the local geoid and local currents. Heights measured by the TGs and by the altimeters are always different since the altimeters do not fly exactly over the TG and the TG is a point measurement, while a radar altimeter considers the entire footprint. For a more precise estimation, altimetry calibration processes take into account the difference in geoid height between the track and the TG, but this is done only at dedicated sites where regional high-resolution geoid models are available [2]. Moreover even presently available high-resolution global geoid models (such as EGM08) are not suitable for this purpose in proximity of the coast (within 20 km) [96]. This comparative anal-

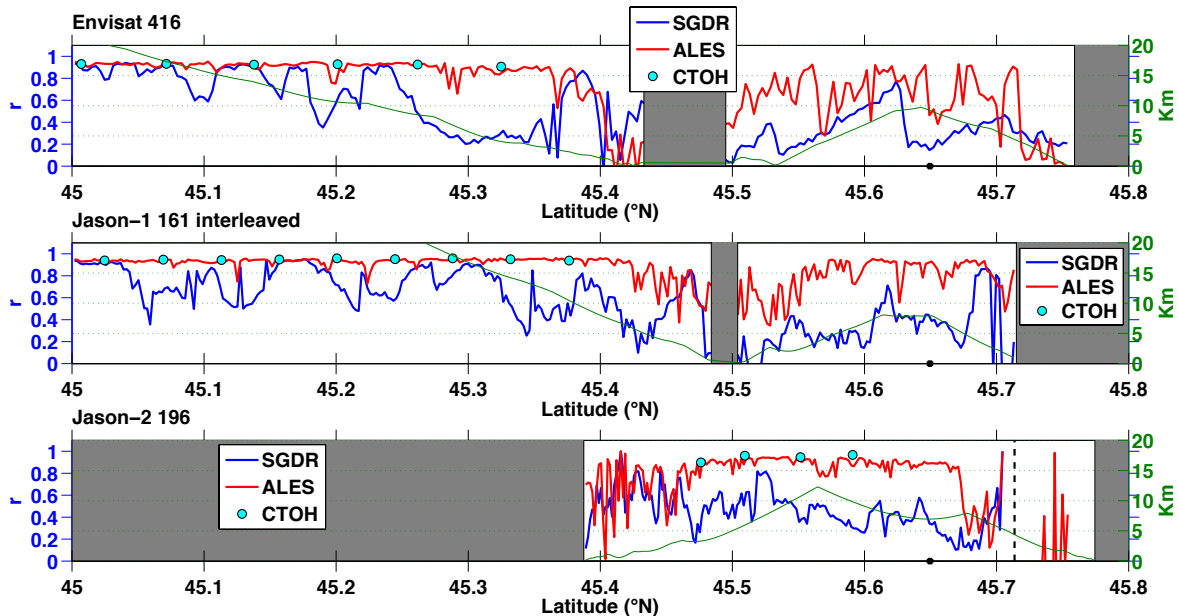


Figure 4.6: North Adriatic: correlation coefficient between Trieste TG and Env 416 (top), J-1 161 (centre) and J-2 196 (bottom). On the x-axis the along-track latitude of the nominal tracks is shown and the latitude of the TG is highlighted with a black dot. Land is shaded in grey. The distance from the closest coastline is specified by a green line which refers to the y-axis on the right. For J-2 196, the latitude of the islet which separates the gulf from the lagoon is represented by a vertical dashed line. Negative values and correlation computed for less than 10 points in the time series are not shown.

ysis does not aim at calibrating a sensor and a correction for geoid gradient is not applied. However, to help the evaluation, figure 4.8 also includes the difference between the DTU10 mean sea surface at the TG and the along-track.

In the open Adriatic, ALES RMSD values decrease steadily towards the TG for Env 416 and for J-1 161, with worsening performances for Env 416 in the last 2.5 km. In the gulf, RMSD values are more variable, in particular for Env 416, but the comparison with the SGDR output for the same waveforms highlights the improvements of the retracking system. For J-2 196, the absolute RMSD is more difficult to evaluate, because of the greater distance (over 30 km at the closest point) from the TG. ALES RMSD accurately follows this shape from 4 km of distance from the Istrian coast until the proximity of the lagoon, in locations where SGDR values are extremely different from the TG measurements.

Since the ellipsoidal height of Mossel Bay TG was not available, a relative analysis was performed by computing the RMS of the difference between TWLE and TG values. The results are shown in figure 4.9 and are very comparable to the correlation analysis.

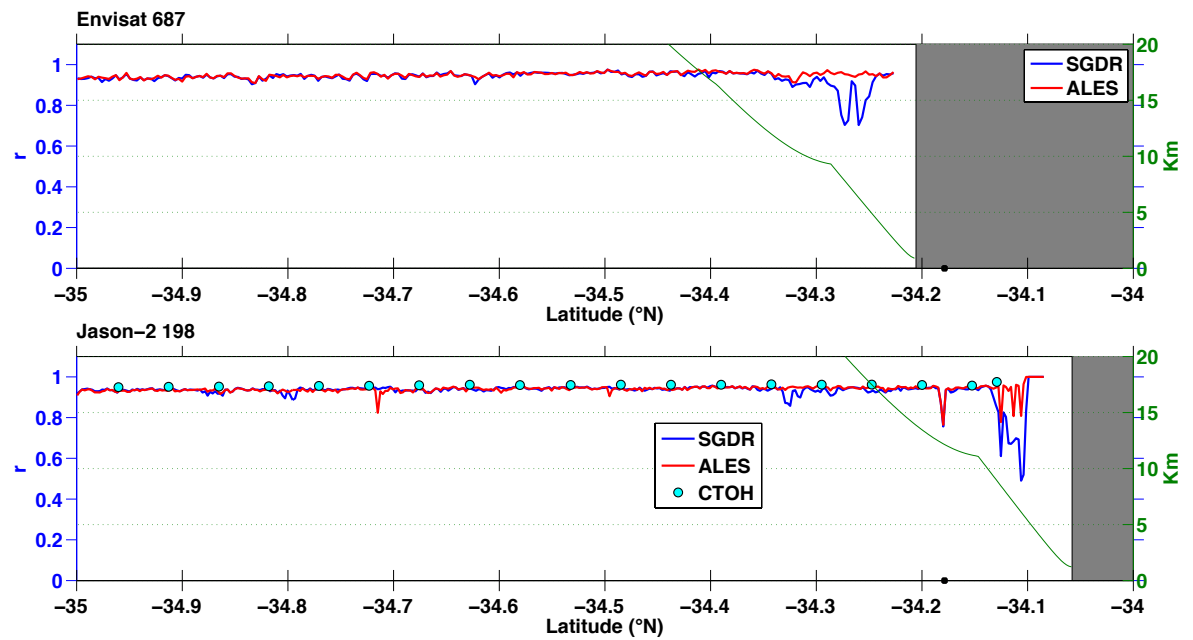


Figure 4.7: South Africa: correlation coefficient between Mossel Bay TG and Env 687 (top), and J-2 198 (bottom). On the x-axis the along-track latitude of the nominal tracks is shown and the latitude of the TG is highlighted with a black dot. Land is shaded in grey. The distance from the closest coastline is specified by a green line which refers to the y-axis on the right. Negative values and correlation computed for less than 10 points in the time series are not shown.

4.2.6 Distribution and bias analysis

One of the main aims of this study was to assess the validity of the same retracker for both open ocean and coastal data. It is important therefore that the high rate estimations of the new retracker are not noisier than the standard SGDR product. The differences between consecutive high-rate TWLE values are considered a good estimation of noise, since TWLE is not supposed to change significantly in 300 to 350 metres, which is the distance between one measurement and the next.

TWLE consecutive differences were computed for ALES, once the outliers had been removed. For comparison, the same calculation was performed for SGDR for the same waveforms. The histograms of consecutive absolute differences of TWLE are shown for each track in figure 4.10. Table 4.4 describes the characteristics of the distributions in terms of mean, std and percentiles (1st and 99th of the whole

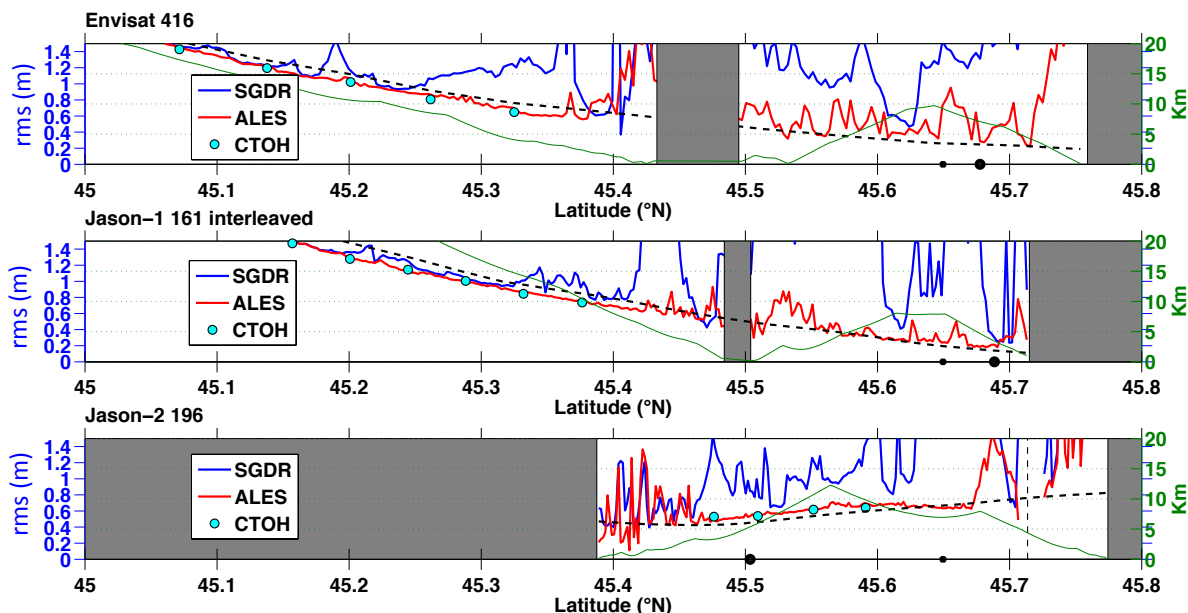


Figure 4.8: North Adriatic: absolute RMS difference between Trieste TG and Env 416 (top), J-1 161 (centre) and J-2 196 (bottom). On the x-axis the along-track latitude of the nominal tracks is shown. Black dots on the x-axis highlight the latitude of the TG (big dot) and of the closest point along track (small dot). Land is shaded in grey. The distance from the closest coastline is specified by a green line which refers to the y-axis on the right. A black dashed line marks the difference between the along track mean sea surface (DTU10) and the mean sea surface DTU10 at the TG. For J-2 196, the latitude of the islet which separates the gulf from the lagoon is represented by a vertical dashed line.

probability density function).

The majority of consecutive differences for both SGDR and ALES are below 10 cm, which is in agreement with the high rate noise figures found in previous studies, such as [60]. In the Adriatic Sea, ALES is less noisy than the SGDR, an improvement that becomes significant in J-2 196, due to the fact that most of the considered short track passes over coastal waters, where SGDR performances are degraded, as seen previously. Considering the tracks near South Africa, the situation changes because this is an area where high significant wave height are often observed: the consequence is a lower percentage of consecutive differences below 10 cm for both SGDR and ALES compared to the tracks in the Adriatic Sea. ALES is slightly more affected by high SWH conditions compared to the SGDR product in terms of noise, particularly for J-2 198. This is also observable in the percentile interval, which is 3 cm wider for ALES in the same track.

The percentile interval is significantly wider for SGDR in the Adriatic sea, which

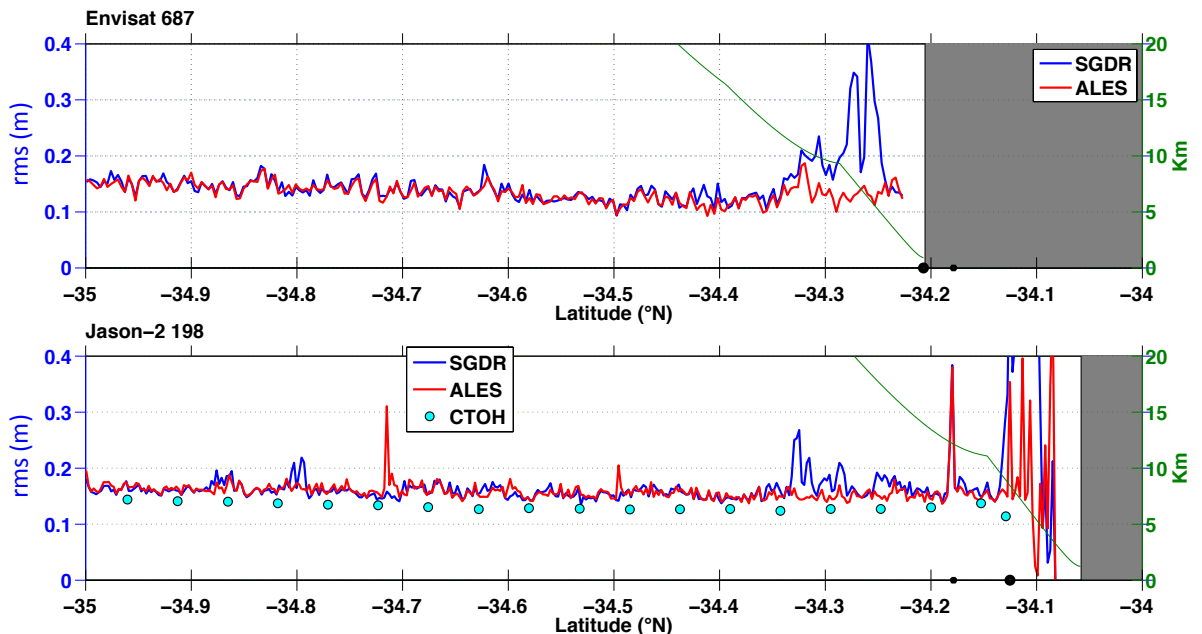


Figure 4.9: South Africa: RMS of the difference between Mossel Bay TG values and Env 687 TWLE (top), and J-2 198 TWLE (bottom). The mean of the difference for each along track location was removed. On the x-axis the along-track latitude of the nominal tracks is shown. Black dots on the x-axis highlight the latitude of the TG (big dot) and of the closest point along track (small dot). Land is shaded in grey. The distance from the closest coastline is specified by a green line which refers to the y-axis on the right.

confirms that the outliers detection performed on ALES successfully eliminates most of the incorrect estimations. ALES mean and std of the distributions also show values similar to SGDR, with an improvement for J-1 161 and J-2 196, which are the two tracks where SGDR output showed the most significant degradation.

Biases between SGDR and ALES were also estimated for each track. Values were averaged only at those along-track points where raw data showed a correlation with the TGs higher than 0.9 for both SGDR and ALES TWLE and at least 50% of valid points were available for both the datasets, therefore no bias was computed for J-2 196, where no SGDR along-track points were so well correlated. Results are presented in table 4.5. Biases are of the order of 1 cm, with stds of the order of 2 to 5 cm. These low values show how ALES constitutes a coastal-dedicated improvement of the standard oceanic product without a significant loss of comparability with the SGDR estimation.

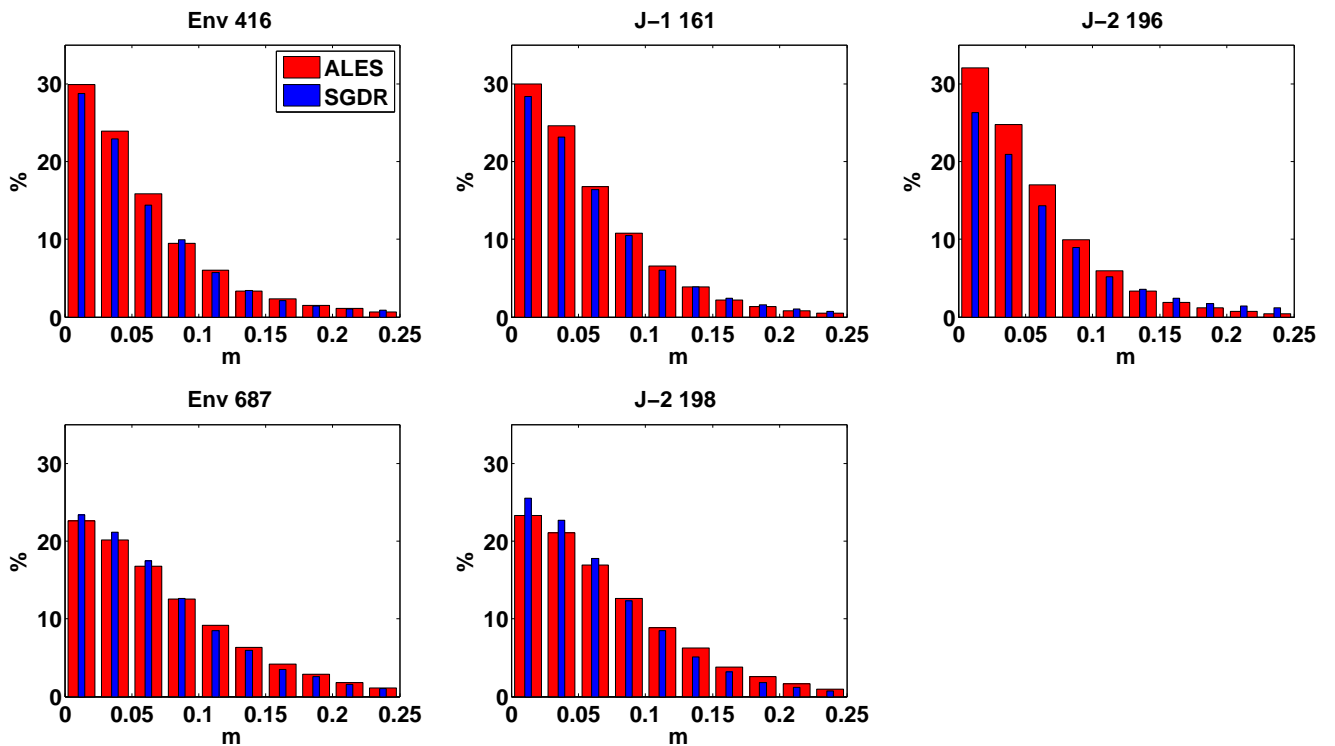


Figure 4.10: Histograms of consecutive TWLE differences in modulus for each track for SGDR (blue) and ALES (red). Columns of SGDR are thinner in order to facilitate the distinction.

		Env 416	Env 687	J-1 161	J-2 196	J-2 198
Mean	SGDR	0.3 cm	0.1 cm	-0.4 cm	-2.2 cm	0.0 cm
	ALES	-0.4 cm	0.0 cm	-0.1 cm	-0.2 cm	0.1 cm
StD	SGDR	38.5 cm	10.1 cm	31.9 cm	47.6 cm	9.7 cm
	ALES	31.4 cm	10.1 cm	15.6 cm	17.5 cm	10.5 cm
1-99%	SGDR	[−108.0 +94.7] cm	[−25.3 +25.5] cm	[−78.9 +70.5] cm	[−1.8 +99.8] cm	[−22.4 +22.1] cm
	ALES	[−93.5 +77.9] cm	[−26.1 +26.1] cm	[−28.8 +29.4] cm	[−34.5 +28.5] cm	[−25.00 +25.2] cm
Obs		10569	13594	24394	15721	46662

Table 4.4: Mean, std and percentiles (1st and 99th) of TWLE distributions for ALES (outliers removed) compared with SGDR. The total number of valid sea level observations for each track is reported in the last row.

	Env 416	Env 687	J-1 161	J-2 198
Bias TWLE (cm)	-1.3 ± 3.5	-1.7 ± 2.6	-1.2 ± 4.4	-0.3 ± 3.4

Table 4.5: Mean biases with std between SGDR and ALES TWLE estimations. Biases were computed using only along-track points where correlation coefficient with TG was higher than 0.9 and more than 50% of valid points were available for both SGDR and ALES. No such points were found for J-2 196, whose bias is therefore not computed.

4.3 ALES Significant Wave Height validation: the German Bight

4.3.1 Dataset and area of study

This second validation exercise is performed by comparing SWH from retracked altimetry data with in-situ observations from buoys located in the German Bight (North Sea), which have already been compared with wave model outputs in [97] and with model and altimeter data in [98]. The area is a particularly challenging testbed for satellite altimetry: it is dominated by tides ranging from 2 to 4 m and characterised by shallow water and large exposed tidal flats during low tide [99]. Other peculiar targets in the area are patches of still water in the tidal flats and the land of the numerous islets, both impacting the radar return when they enter the satellite footprint.

One track from Jason-1 and Jason-2 (J-2 213 and J-1 213) and three tracks from Envisat (Env 543, Env 474 and Env 85) have been reprocessed and waveforms at 20 Hz for Jason and at 18 Hz for Envisat have been retracked by ALES. The SWH estimations for Jason were corrected using the instrumental corrections described in [100] and [64]. The choice of more tracks for Envisat is justified by the different experiments undertaken and the fact that the results were less clear than with Jason. A comparison with data coming from different buoys was therefore necessary and possible thanks to the high density of tracks, which was not the case for Jason. On the other side, the high amount of Jason available cycles, thanks to the 10-day repetition rate, was a sufficient proof of robustness for the results. In-situ data come from three buoys which deliver a measurement every 30 minutes: Helgoland, Elbe and Westerland. The data are provided by the Bundesamt fuer Seeschiffahrt und Hydrographie (BSH).

Figure 4.11 shows the area of study, including the satellite tracks and buoys' locations. It is relevant to point out the flight direction of each satellite as it flies over each region, since land-to-sea and sea-to-land transitions might influence the behaviour of the on-board tracker in different ways: Env 543, Env 85 and J-2/J-1 213 are ascending tracks (South to North), while Env 474 is descending. The minimum distance between a satellite track and a buoy is 3.2 km, while the maximum distance is 16.5 km. It is here assumed that these distances are acceptable for a meaningful comparison. As a reference, [101] estimated a SWH difference of 0.15 to 0.2 m for a separation of 14 km, but this was based on a global dataset. The extended stretches of high correlation found in the along-track analysis in section 4.3.5 will however

serve as a confirmation that the assumption is valid in the coastal region object of this study.

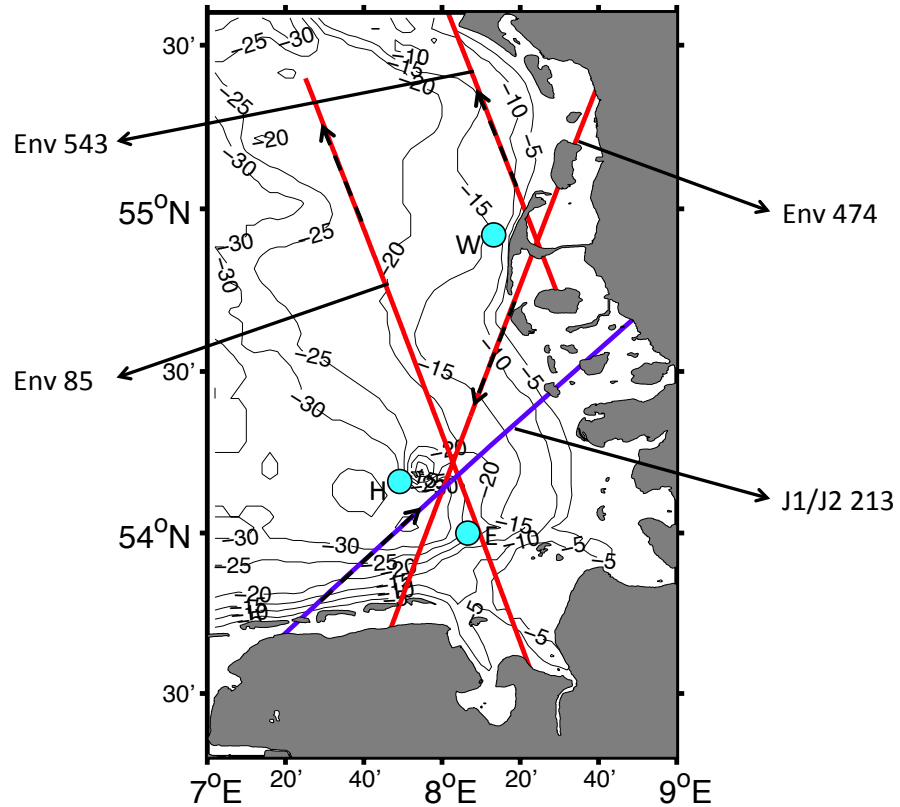


Figure 4.11: The areas of study and the extent of the retracked altimetry passes. Bathymetry is shown by means of contour lines: they are drawn every 5 m.

Table 4.6 summarises the characteristics of the dataset. For every track, all the cycles for which there was a simultaneous in-situ measurement (within a 30-minutes time window) were considered. [101] estimated that when the average temporal separation between buoy and altimeter is 15 minutes, the effect in the difference between the two measurements will be of about 0.1 m. In order to limit the impact of the temporal separation between the two measurements, the buoy data are resampled in time onto a 1-minute grid by means of linear interpolation. Following the resampling, the value closest to the satellite overpass in time is taken as the ground truth.

A peculiarity of the German Bight lies in the variable extension of the dry areas depending on the tidal phase. This needs to be accounted for to correctly interpret the output of the retracking and can be appreciated from the radargrams in figure 4.12. The two radargrams for each of the three considered Envisat tracks show the

	Buoy	Min Dist (km)	Dist from coast (km)	Num of cycles	Time (mm-20yy)
Env 85	Elbe	3.2	17.3	53	09-03 to 09-10
Env 85	Helgo	16.1	8.9	48	10-02 to 09-10
Env 474	Helgo	12.2	7.8	55	12-02 to 09-10
Env 474	Elbe	11.1	16.5	62	10-02 to 09-10
Env 543	Wester	12.3	0.3	50	05-03 to 10-10
J1 213	Helgo	10.7	9.1	141	02-02 to 02-09
J2 213	Helgo	10.7	9.2	112	07-08 to 12-12

Table 4.6: Dataset characteristics. Column 2: buoy used for validation. Column 3: minimum distance between the satellite track and the buoy. Column 4: distance (of the closest point between satellite track and buoy) from the coast; in parentheses, the minimum distance of the same point from Helgoland islands where relevant. Column 5: number of cycles considered in the validation (cycles where satellite data were missing and/or coincident buoy data were not available have been excluded). Column 6: time interval between the first and the last considered cycle in month-year format.

waveforms for both low- and a high-tide events. The y-axis corresponds to the gates number and the x-axis to different waveforms identified by their latitude. ALES is capable of retracking waveforms with a distinct leading edge and a decaying trailing edge, even if corrupted by bright targets. However, particularly in the low-tide phase, waveforms present a single very high spike, which is typical of specular reflections from a flat surface, which could either be land or isolated patches of water. The location of specular returns in the low tide phase can be used as a trace to detect the extension of the tidal flats.

4.3.2 Outliers detection and 1-Hz averages

From high-rate waveforms, ALES retracked SWH is then averaged to generate 1-Hz estimations. A check is performed in order to eliminate outliers on every block of 20 high-rate values X : the median value and the scaled median absolute deviation (\widehat{MAD}) are computed. Each estimation x is considered valid if:

$$x < \text{median}(X) + 3 \times \widehat{MAD}(X)$$

or

$$x > \text{median}(X) - 3 \times \widehat{MAD}(X)$$

where

$$\widehat{MAD}(X) = 1.4286 \times \text{median}(|X - \text{median}(X)|)$$

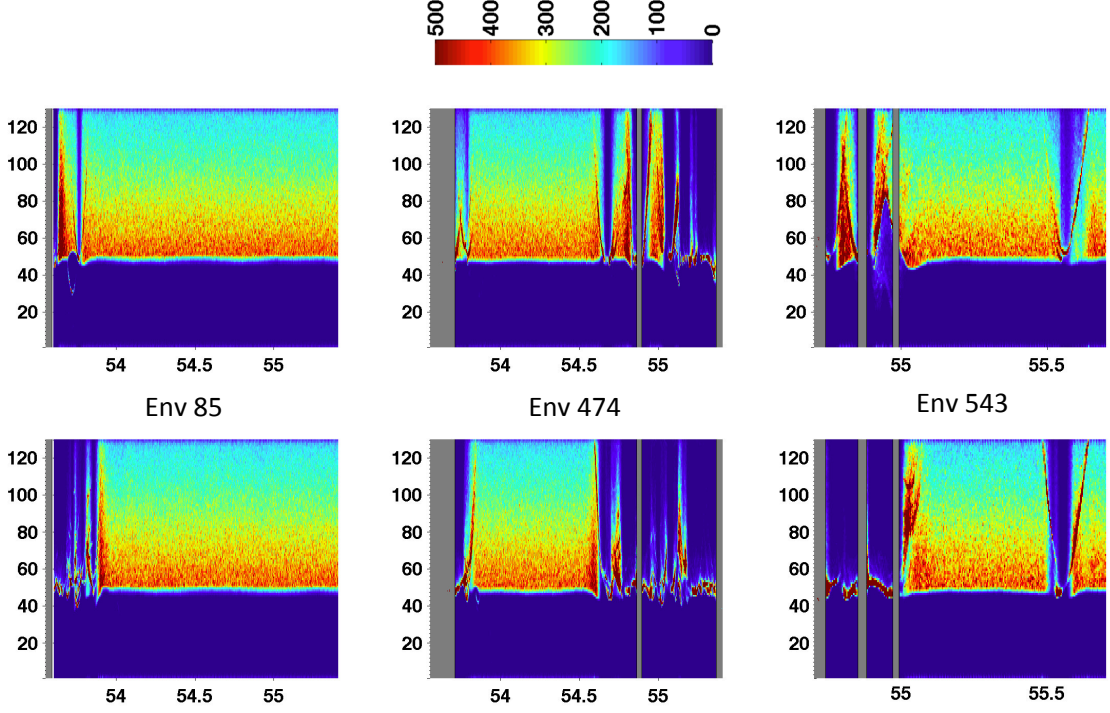


Figure 4.12: Two examples of radargrams for each Envisat track: the upper panels correspond to times of high tide, while the lower panels refer to a low-tide situation. Each column corresponds to a high-rate waveform along a satellite track. The horizontal dimension corresponds to the latitude of each waveform. The intensity of the return is colour-coded from blue to red. The area of the tidal flats is recognisable by the presence of specular waveforms (single narrow peak and no gradual decay in the trailing edge), particularly evident at low tide, when more land lies above the sea level.

The \widehat{MAD} scaled using the factor 1.4286 is approximately equal to the std for a normal distribution. Statistics based on the median are more robust and suitable for outliers detection and have been already applied to satellite data [102]. Once the outliers have been excluded, the median of the remaining points is computed in order to generate the 1-Hz estimation.

4.3.3 Preliminary analysis of DFT gates and σ_p impact in SWH estimation

As mentioned in section 2.3.1, The Envisat SGDR processing used different σ_p values depending on the version and provided additional DFT gates to describe the leading edge of the waveform. The validation against in-situ buoys gives the chance to test the impact of these differences, which affect SWH estimation. This prelim-

inary analysis is performed in order to define the ALES choices that will be used throughout the rest of the validation.

For Envisat, the 20 nominal high-rate locations closest to each buoy are considered. The points along Env 543 close to the Westerland buoy, which is located at 0.3 km from the coast, are not included in this analysis due to the inaccuracy of the corresponding altimetry estimates.

The difference between ALES SWH retrieval and the in-situ data is analysed in terms of mean bias and std for different values of SWH. When the modulus of the difference is bigger than one metre, the measurement is considered to be an outlier and is not included in the computation of bias and std. The results of the analysis are displayed in figure 4.13. Results are shown for varying SWH at intervals of 50 cm, i.e. the 0.25 m point on the x-axis includes all the data for which the corresponding in-situ SWH estimations are between 0 and 50 cm.

Panel D shows the number of available observations for varying SWH. Most of the observations are at low sea states ($\text{SWH} < 2.5 \text{ m}$) and only very few measurements are available for more extreme situations. This limits the validity of the study to low sea states, which are nevertheless considered particularly challenging to be detected by retracking algorithms, since a sharp leading edge in a waveform is described by fewer gates and therefore the derived estimate of the rising time is less accurate as a percentage.

Concerning the choice of σ_p , panel A shows that a higher σ_p produces a lower SWH estimation (roughly 20 cm of difference for low sea state). Compared to in-situ data, the higher σ_p leads to a marked underestimation. Similar conclusions were found by [21].

Looking at the addition of the 2 DFT intermediate gates (referred as ALES+2 in figure) it is seen from the std (panel B) that this strategy has a positive effect in terms of noise reduction. Moreover for SWH smaller than 0.5 m, a lower std is shown for the estimations that adopt the $\sigma_p = 0.6567r_t$. This is due to the fact that several estimations of σ_c are smaller than σ_p and therefore show up as zeroes in the SWH value, which in this case is derived from the square root of a negative value (as seen in section 2.3.1). Setting $\text{SWH}=0$ for every negative value of SWH^2 is a practice adopted in the current versions of the official products. If on one side it generates anomalous low std values, it must also be said that, given that a negative SWH cannot be a physically plausible sea state, a null SWH represents the closest realistic estimation. Using $\sigma_p = 0.53r_t$ significantly reduces the null estimations and therefore the statistics show a much more realistic std value.

Overall, ALES+2 with $\sigma_p=0.53$ is the retracking scheme with the best perfor-

mances, including the smallest percentage of estimations which have more than 1 m of difference with the ground truth (indicated as outliers in panel C).

Although this section is focused on SWH retrieval, it is important to note that the insertion of the 2 DFT gates does not change significantly the range estimation. Experiments carried out along Env 85 in the open sea interval between 54.4° and 55.2° of latitude showed that the range estimations with and without the 2 DFT gates are 99.97% correlated, with a 2 mm bias and a 1 mm std.

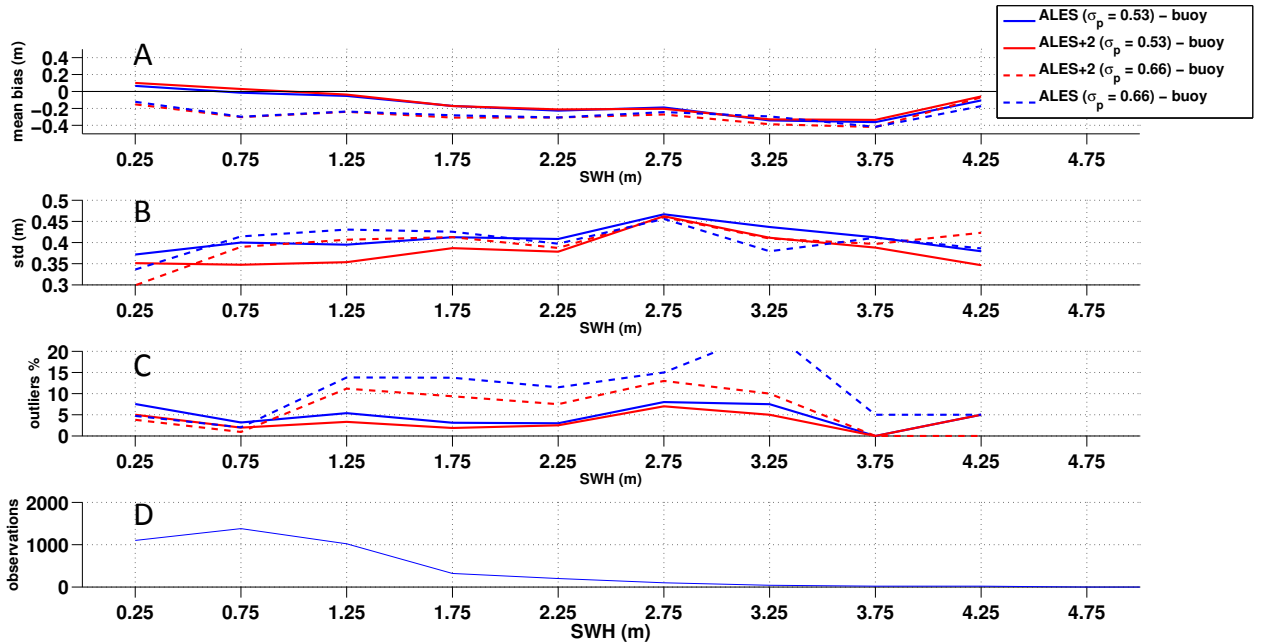


Figure 4.13: Analysis of 4 different retracking strategies for Envisat. Statistics are produced considering the 20 nominal high-rate points from Env 474 and Env 85 closest to the Helgoland buoy and the high-rate points from Env 85 closest to the Elbe buoy. The difference between ALES SWH retrieval and buoy measurements are analysed in terms of A) mean bias, B) standard deviation (std), C) percentage of outliers and D) number of available observations for varying SWH.

4.3.4 Analysis at the closest locations

The next stage of the SWH validation against in-situ data is the analysis at the closest point between the buoys and the corresponding satellite tracks. Figure 4.14 shows the results for the three Envisat tracks, with the upper two plots showing the comparison of Env 85 with two buoys at the respective closest points. Each circle (red for ALES, blue for SGDR) shows the retracked SWH value corresponding to the ground truth (on the x-axis) at a specific cycle. The SWH from Envisat adjusted

by using $\sigma_p = 0.53r_t$ is shown in black squares. In the same way, figure 4.15 shows the results for pass 213 from Jason-2 (plots on the left) and Jason-1 (plots on the right). For Jason, the analysis is performed for high-rate estimations (upper plots) and 1-Hz points (lower plots).

The straight lines are the best fit of the data. A summary of the results in terms of correlation coefficient, slope, bias and std w.r.t. the buoy estimations is reported in Table 4.7 for Envisat and Table 4.8 for Jason. All the points are considered and no outlier is removed, in order to give the best possible evaluation of the available dataset. For Envisat, statistics for SGDR adjusted with $\sigma_p = 0.53r_t$ are shown in brackets. Given the similarity of the results, only one "double comparison" of the same track with two buoys is shown in the plots (Envisat 85 against the Helgoland and the Elbe buoy), while the comparison of Envisat 474 with the Elbe buoy is reported only in the table.

Envisat

For the Envisat tracks, the analysis is performed on the 1-Hz data, since high-rate SWH is not available in the SGDR. The point of Env 543 closest to the Westerland buoy presents particularly bad estimations for both SGDR and ALES datasets. As previously mentioned, the reason is that the point is located at a distance of only 0.3 km from the coast. At this distance there is often no clear leading edge in the waveforms and therefore even a subwaveform application of the Brown model is often inadequate. It is anyway relevant that ALES estimations are much closer to the ground truth than SGDR.

Considering all the tracks, the underestimation of SGDR is evident, with several estimations being zeroes, due to the fact that SGDR uses $\sigma_p = 0.6567r_t$. This underestimation, assessed as median bias, is never less than 20 cm, except for Envisat 474 compared to the Elbe buoy. The median bias of ALES is less than 10 cm for all the comparisons. The use of $\sigma_p = 0.53r_t$ in the SGDR product brings an improvement in terms of bias in four out of five comparisons, although the low wave heights are overestimated. The slopes suggest for both the datasets a progressive underestimation of SWH as the values of the buoy increase, but the number of observations at SWH>2 m is too small to draw a conclusion. All the statistics show a marked improvement in ALES. This is particularly true in the comparisons with the Helgoland buoy (correlation increases by ~ 0.3 and std halves). This is expected, since the calm coastal waters and the land of Helgoland islands produce bright targets visible in the radargrams, which corrupt the leading edge and have consequences on the estimations of the standard product. Considering the number of

samples that are used to compute the correlation, it is possible to test the significance of the difference in correlation between ALES and the standard product using the Fisher r-to-z transformation and subsequently evaluating the corresponding p-value to reject the null hypothesis, i.e the possibility that the two time series have no relationship with each other. Assuming as highly significant a correlation coefficient corresponding to a p value lower than 0.05, all the differences in correlation using SGDR or ALES are highly significant except for Env 85 with the Elbe buoy, where the correlation coefficient is the same for all the time series.

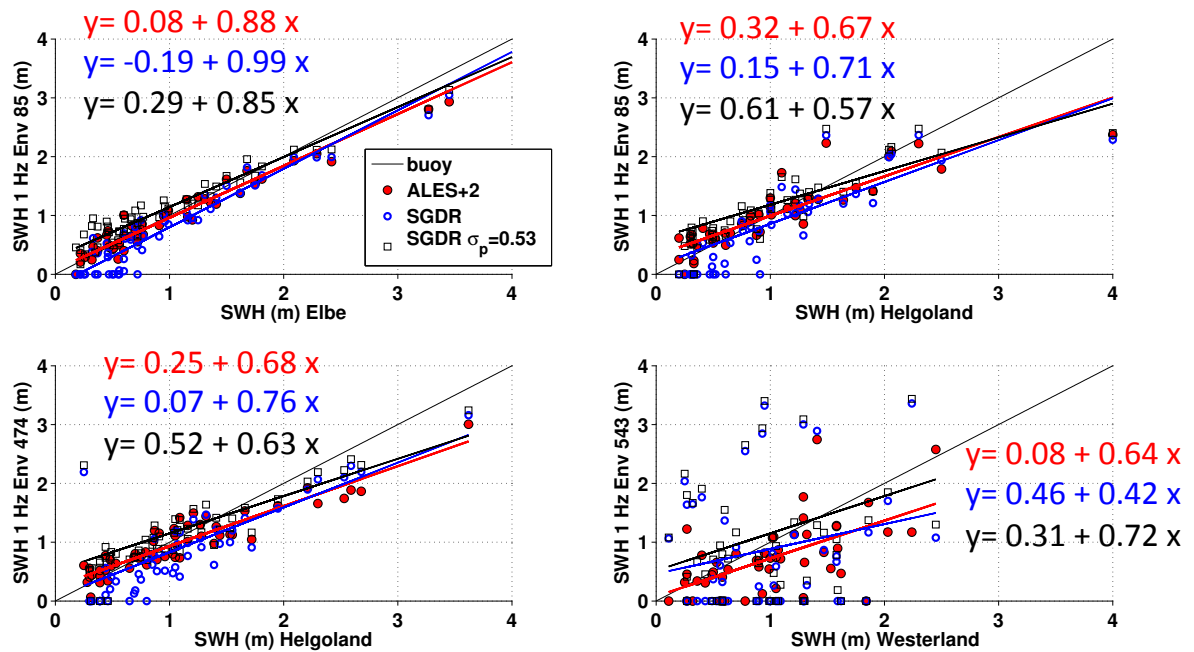


Figure 4.14: Scatter plot of Envisat retracked SWH against the corresponding in-situ estimations at the closest 1-Hz point of the satellite track to the buoy. Shown are the results with ALES with waveforms augmented by 2 gates (full circle), standard SGDR (open circle) and SGDR recomputed using a different σ_p (open square)

Jason

The statistics obtained from the ALES retracked dataset show significant improvements in all terms compared to the corresponding SGDR product. The most significant improvement concerns the std of the differences between altimetry estimations

and buoy values, which leads to a variance reduction by a factor of 5 at 1 Hz. Compared to Envisat, the slopes of the fitted straight lines are more correct, since values of SWH higher than 2 m are not underestimated. As in Envisat though, statistics are much more robust for lower SWH. No systematic bias is present, which means that the σ_p value in use (which in this case is the same both in ALES and in SGDR) is appropriate. The improvement in correlation from SGDR to ALES is verified as highly significant in both Jason-1 and Jason-2 at 1 Hz, while for the 20 Hz time series it is not possible to reject the null hypothesis.

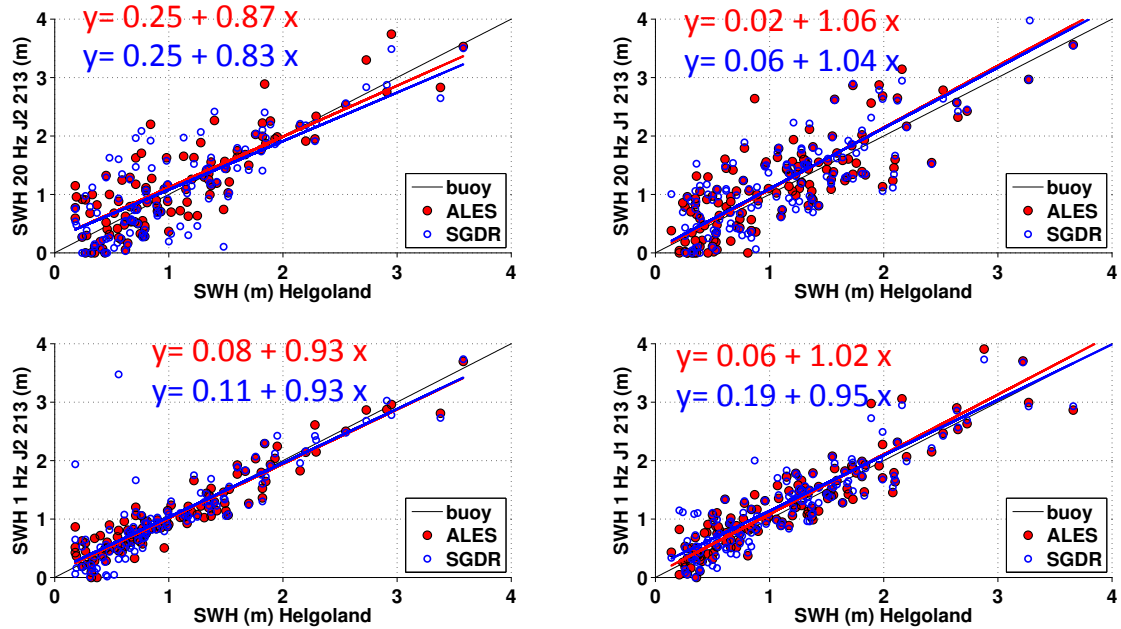


Figure 4.15: Scatter plot of Jason retracked SWH against the corresponding in-situ estimations at the closest point of the satellite track to the buoy. The upper plots refer to the 20-Hz data, the lower to the 1-Hz data. The plots on the left refer to Jason-2, the plots on the right to Jason-1. Shown are the results with ALES (full circle) and standard SGDR (open circle).

4.3.5 Along-track analysis

Along-track performances were computed for ALES and SGDR-retrieved SWH in terms of correlation at 20 Hz (18 Hz) and 1 Hz and median values of the std and the

		Correlation	Slope	Bias (m)	StD (m)
Env 85 (Helgoland)	SGDR	0.56 (0.52)	0.71 (0.57)	-0.23 (0.12)	0.69 (0.69)
	ALES	0.89	0.63	0.09	0.27
Env 85 (Elbe)	SGDR	0.97 (0.97)	0.99 (0.85)	-0.22 (0.13)	0.18 (0.15)
	ALES	0.97	0.88	-0.01	0.13
Env 474 (Helgoland)	SGDR	0.63 (0.60)	0.76 (0.63)	-0.31 (0.05)	0.56 (0.58)
	ALES	0.93	0.65	0.00	0.20
Env 474 (Elbe)	SGDR	0.91 (0.90)	1.06 (0.90)	-0.05 (0.23)	0.21 (0.22)
	ALES	0.97	0.97	0.09	0.08
Env 543 (Westerland)	SGDR	0.20 (0.15)	0.42 (0.63)	-0.48 (0.16)	0.67 (0.58)
	ALES	0.55	0.55	-0.01	0.41

Table 4.7: Validation results of the nominal satellite tracks (for Envisat) at the 1-Hz points closest to each buoy, in terms of: correlation (column 3), slope of the linear fit (column 4), median bias computed subtracting each buoy estimation from the corresponding retracked SWH (column 5), std w.r.t. the buoy estimations (column 6). Statistics for SGDR adjusted with $\sigma_p = 0.53r_t$ are shown in brackets. The buoy of reference is reported in brackets in the first column.

		Correlation	Slope	Bias (m)	StD (m)
J2 213 - 1 Hz (Helgoland)	SGDR	0.85	0.93	- 0.04	0.34
	ALES	0.95	0.90	-0.01	0.15
J2 213 - 20 Hz (Helgoland)	SGDR	0.80	0.83	0.07	0.67
	ALES	0.85	0.87	0.01	0.57
J1 213 - 1 Hz (Helgoland)	SGDR	0.81	0.95	0.11	0.52
	ALES	0.93	0.98	0.03	0.23
J1 213 - 20 Hz (Helgoland)	SGDR	0.86	1.04	-0.02	0.55
	ALES	0.87	1.06	-0.01	0.33

Table 4.8: Validation results of the nominal satellite tracks (for Jason) at the points closest to each buoy, in terms of: correlation (column 3), slope of the linear fit (column 4), median bias computed subtracting each buoy estimation from the corresponding retracked SWH (column 5), std w.r.t. the buoy estimations (column 6). The buoy of reference is reported in brackets in the first column.

bias at 1 Hz considering all the available cycles (all w.r.t. the buoys estimations). The results are shown in figure 4.16 for Env 85 against the Helgoland and the Elbe buoys, figure 4.17 for Env 474 against the Helgoland buoy and Env 543 against the Westerland buoy, figure 4.18 for J1 213 and J2 213 against the Helgoland buoy.

Envisat

Considering the PCHC, it is evident that in the open sea the steps followed to derive the 1-Hz estimations from the high-rate values and described in section 4.3.2 improve the correlation. It is also noticeable that the wave height signal is well correlated along the entire considered length of the satellite tracks (except close to the tidal flats), which suggests that the SWH field in the area is dominated by synoptic scales and confirms the validity of the assumption that a comparison between altimeter and buoys is meaningful despite the spatial separation. Looking at the same track (Env 85) compared to two different buoys (Helgoland and Elbe) reveals that high-rate estimations are more correlated with Elbe than with Helgoland in-situ data. This can be related to the position of the Helgoland buoy, which is located at 2 km of distance from an island and therefore the local sea state can also be influenced by small scale phenomena such as changes of wind patterns due to the sheltering caused by the land. The presence of the Helgoland island itself influences the high-rate data due to specular reflections that alter the standard shape of an oceanic waveform as explained in the previous section: this has an impact on the correlation, which is visible along tracks Env 85 and Env 474 for the latitude interval $54.1^\circ - 54.3^\circ$. It also leads to a lower PCHC for the 1-Hz points in the same area for the SGDR, while ALES data succeed in keeping more cycles to obtain the same level of correlation.

The areas of the tidal flats show drastic drops in PCHC. ALES 18-Hz estimations generally present a PCHC between 20 and 40 % in these areas (figure 4.16). Nevertheless, the values averaged at 1 Hz have a lower percentage, which is sometimes overtaken by the original SGDR 1-Hz product. It must be noticed that even at high tide the sea state in the tidal flats will be heavily influenced by the shallow water and therefore the correlation of the signal with an off-shore buoy is likely to be less significant. In the tidal flats, since the 1-Hz points for ALES have a lower PCHC than the corresponding 18-Hz estimations, it might be worth to perform a more careful screening of the dataset, for example considering the estimated sea level, the backscatter coefficient and the goodness of waveform fit to avoid considering wrong estimations. This is not done in this validation, which is focused on the quality of the raw data.

Considering the median of the stds at 1 Hz, ALES succeeds in keeping it below 0.5

m all along the track in the open sea showing a constant improvement if compared to the SGDR product. The bias of ALES for Env 85 and Env 474 reaches its minimum at the point closest to the buoy, as expected, while SGDR is constantly biased by about 20 to 30 cm all along the tracks. The SGDR product modified as shown in equation 4.3 overestimates the SWH compared to the ground truth and to the ALES estimates, despite the same σ_p approximation adopted. This suggests that the best value of σ_p can be different for different retracking algorithms and that the original σ_p approximation used in the previous SGDR version brings the best result when applied to a subwaveform retracker such as ALES.

Generally, for all the tracks the PCHC has a decay steeper in SGDR than in ALES when approaching the coast. It is therefore inferred from the plots that ALES is able to retrieve an unbiased estimation of SWH also when the trailing edge of an oceanic waveform is corrupted by highly reflective targets, and to increase the amount of good estimations in the coastal region close to the tidal flats.

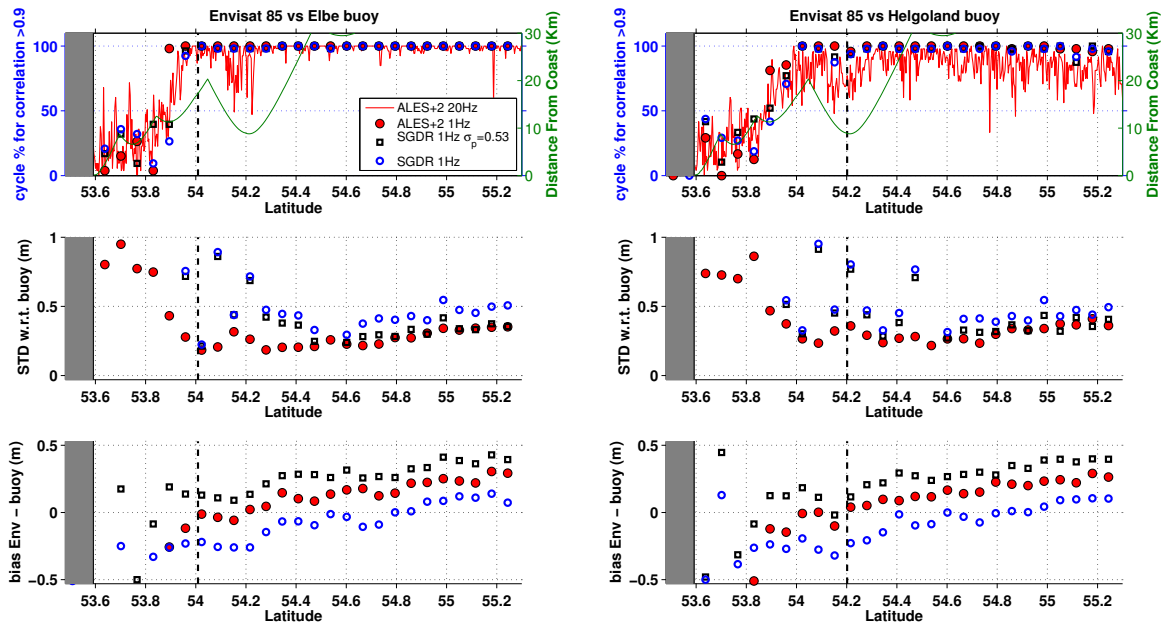


Figure 4.16: Along-track validation of SWH estimations for Envisat pass 85 against data from Elbe (left) and Helgoland (right) buoys in terms of PCHC at 1 Hz and 18 Hz (top), std of 1-Hz estimations from buoy values (centre) and median bias of 1-Hz estimations (bottom). On the x-axis the along-track latitude of the nominal tracks are shown. Land is shaded in grey. The closest point of the track from the buoy is highlighted by a black dashed vertical line. The distance up to 30 km from the closest coastline is specified by a green line which refers to the y-axis on the right.

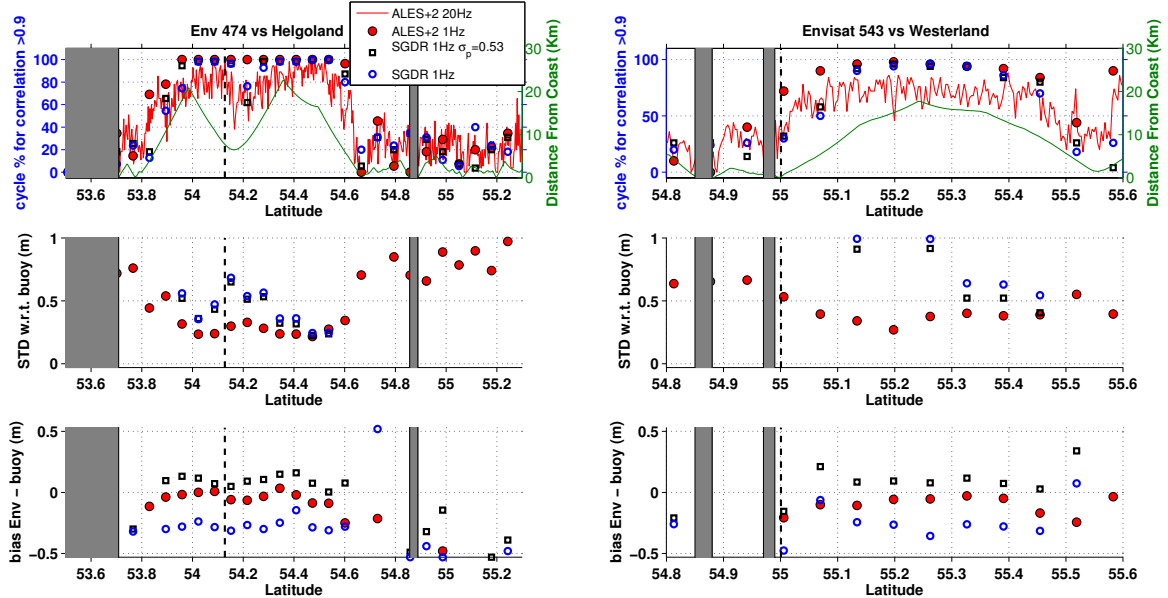


Figure 4.17: Along-track validation of SWH estimations for Envisat pass 474 against data from the Helgoland buoy (left) and Envisat pass 543 against data from the Westerland buoy (right) in terms of PCHC at 1 Hz and 18 Hz (top), std of 1-Hz estimations from buoy values (centre) and median bias of 1-Hz estimations (bottom). On the x-axis the along-track latitude of the nominal tracks are shown. Land is shaded in grey. The closest point of the track from the buoy is highlighted by a black dashed vertical line. The distance up to 30 km from the closest coastline is specified by a green line which refers to the y-axis on the right.

Jason

The comparison with Jason SGDR in terms of PCHC with the buoy estimations is even more reliable than the corresponding with Envisat data, since 20-Hz SGDR estimations of SWH are available (unlike in Envisat) and since each track has a higher number of cycles. ALES improves the quality of SWH estimations and is constantly more correlated than the original SGDR product. Not only it shows improvements when the satellite track is close to the tidal flats area, but it also succeeds to have a PCHC between 20 and 40 % in the tidal flats, where very few estimations from the SGDR are available. In terms of std w.r.t. the buoy estimation, there is a marked improvement brought by the ALES product, which keeps the values below 0.5 m until the tidal flats, with a slight improvement when considering Jason-2 compared to Jason-1. The improvements in Jason-2 are probably due to the smaller mispointing values compared to Jason-1, which improves the accuracy in the estimates of rise time of the leading edge and amplitude.

The results obtained in terms of bias are satisfactory, despite the fact that Jason-

1 range corrections are derived for a 4-parameter retracking algorithm (the off-nadir angle is added as an unknown value to be estimated in the Brown functional form) while ALES performs a 3-parameters estimation. From the along-track analysis there is no significant systematic bias between SGDR data and buoy estimations. This is attributable to the fact that the same σ_p approximation was used in SGDR and ALES, as opposed to what has been seen in the previous section for Envisat. It must be noted that the results in terms of bias and std for SGDR over the tidal flats are not significant, as less than 5% of the cycles contain an estimated SGDR value in those locations.

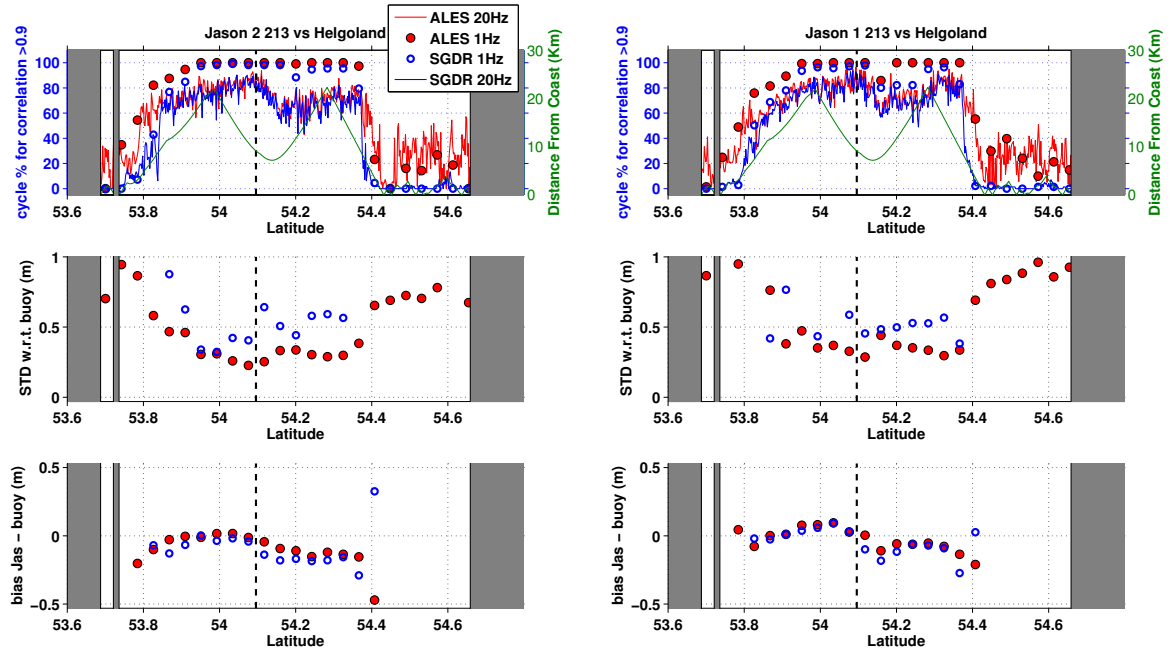


Figure 4.18: Along-track validation of SWH estimations for Jason-2 (left) and Jason-1 (right) pass 213 against data from the Helgoland buoy in terms of PCHC at 1 Hz and 20 Hz (top), std of 1-Hz estimations from buoy values (centre) and median bias of 1-Hz estimations (bottom). On the x-axis the along-track latitude of the nominal tracks are shown. Land is shaded in grey. The closest point of the track from the buoy is highlighted by a black dashed vertical line. The distance up to 30 km from the closest coastline is specified by a green line which refers to the y-axis on the right.

Chapter 5

ALES application: the sea level annual cycle in the North Sea/Baltic Sea transition zone from Envisat

The aim of this chapter is to verify whether the ALES-based coastal satellite altimetry product is able to improve the description of the annual cycle of the sea level in the coastal ocean on sub-basin scales (10 - 100 km) and, in combination with information from different sources, to identify the processes that drive the variability.

To answer this question, the chapter focuses on the transition zone between the North Sea and the Baltic Sea. The area is characterised by challenging conditions for satellite altimetry. The jagged coastline and several islands are potential sources of corruption for altimetry measurements, while shallow water areas are known to be particularly critical for tidal patterns (due to shallow water components and non-linear tides). Nevertheless, the high number of reliable TGs makes the area an ideal test for coastal sea level variability studies. Up to now, sea level description of the area has mainly focussed on in-situ data [103, 104]. The first attempt to use coastal altimetry in the area was performed by [6], although avoiding data closer than 10 km from the coast, while other studies limited the use of altimetry to the open sea [105]. More recently, [106, 107, 108] used Sea Level Height Anomalies (SSHA) extracted from a multimission global gridded data product in the open Baltic and North sea, underlining that further developments in coastal altimetry could lead to improvements in the description of the sea level variability. The chapter follows this path, including and evaluating the contribution of along-track measurements in the coastal zone.

This research is based on ALES reprocessed Envisat data in comparison with the up-to-date sea level product generated by the ESA Sea Level Climate Change Initiative (SL_cci) community, which is an international effort to provide the most reliable and freely available information on sea level, but which has not specifically generated coastal products yet.

5.1 Area of study

The area of study is shown in figure 5.1. The area has been divided into sub-basins, based on different oceanographic characteristics. To the west, it includes the Skagerrak Sea, characterised by a mainly cyclonic circulation influenced by the topography [109]. The southernmost part of the sub-basin (D Skagerrak) is shallow, like most of the North Sea, but the northern area (N Skagerrak) is characterised by the deep Norwegian Trench [110]. A wide surface current coming from the west carrying waters from the Atlantic and the German Bight (Jutland Current) turns northward when it encounters the brackish water from the Baltic Sea and follows the Norwegian coast, being named Norwegian Coastal Current (NCC). To the south, the Kattegat Sea is a shallow sea characterised by estuarine processes, namely the mixing of salty Atlantic water with brackish water from the Baltic Sea and fresh water from rivers [110]. The inflow and outflow of water through the Danish straits (the Belts sub-basin) depends on the sea level difference between the Kattegat Sea and the Arkona basin (the westernmost part of the Baltic Sea)[111]. The mean flow condition across the straits, i.e. an upper brackish water layer flowing from the Baltic Sea to the Kattegat Sea and an opposite flow in deeper waters, can be altered by local wind conditions and larger atmospheric circulation patterns [112]. In this study, the easternmost strait (Oresund) is left out due to the lack of altimetry tracks in the area. Finally, the Arkona Basin is mainly characterised by a decreasing salinity from west to east [113]. More detailed descriptions of the circulation in this area can be found in [114, 115, 116].

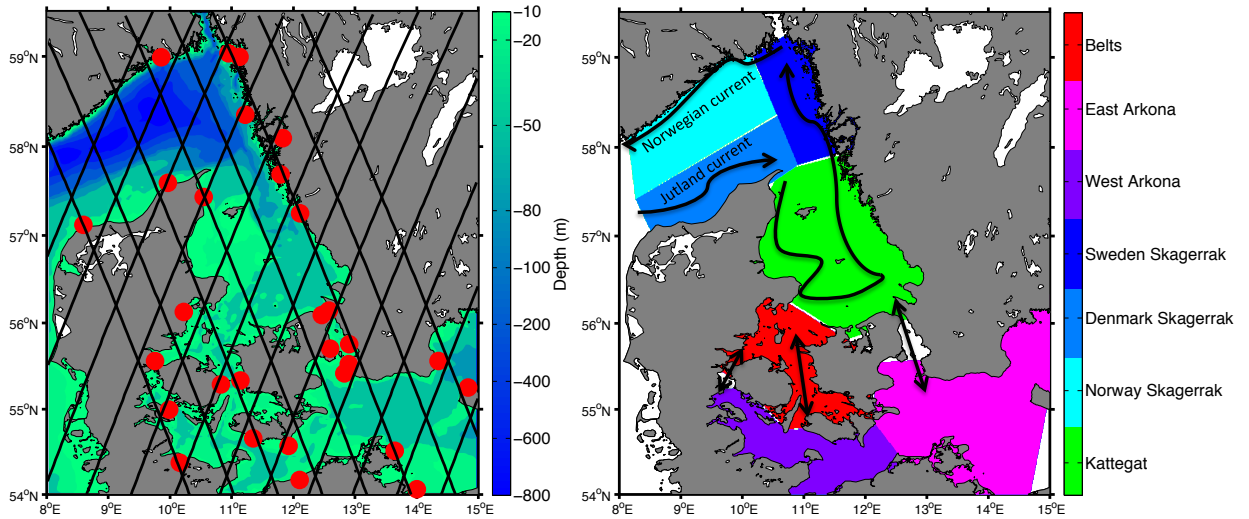


Figure 5.1: The area of study. On the left, the red circles are the locations of the TGs and the black lines are the Envisat tracks. On the right, the sub-basin are defined and colour-coded and the main circulation pattern is shown. Colorscale is linear between 0 and -100 and then linear but with different slope between -100 and -800.

5.2 Dataset

The main source of data used in this study is satellite altimetry. Here, the focus is on the data from the ESA Envisat mission, which have been reprocessed with ALES. The data cover Envisat orbital Phase B, from autumn 2002 to the 22nd October 2010, the date on which the Envisat orbit was changed. Tracks are repeated every 35 days. This limits the amount of data along repeat tracks, but makes the Envisat mission particularly suitable for regional studies of seasonal phenomena, due to the high spatial coverage of the tracks (see figure 5.1) compared to the Jason series, which have a 10-day repeat time, but a larger distance between the tracks.

The wet tropospheric correction obtained by microwave radiometer measurements is not reliable in the coastal zone (see section 2.4.2). In the SGDR, a modelled correction is available, based on the European Centre for Medium-Range Weather Forecasts (ECMWF) model, but its resolution is suboptimal: the temporal resolution is 6 hours, but the tropospheric water content can vary at shorter temporal scales, while the maximum spatial resolution (from the operational model) is $0.12 \times 0.12^\circ$, i.e. coarser than the altimeter resolution [46]. For this study, the GNSS-based Path Delay (GPD) wet tropospheric correction has been used.

The tide correction and the mean sea surface (MSS) already available in the SGDR have been substituted with validated up-to-date products: the DTU10 global

tide model, particularly suitable for shallow seas, and the DTU13 mean sea surface [75, 117]. MSS choice was driven by the need to harmonise the set of corrections applied in the products: since the DTU model was already the choice of the validated ALES product as well as of the SL_cci product, this choice was kept. DTU10 tide model was preferred to GOT 4.8 (model of choice in the gridded SL_cci) and applied to ALES and SL_cci along-track data due to the less favourable statistics of GOT against shallow tide gauges and erroneous values of the correction in the Danish seas, as well as the good performances of the DTU model, as recently shown by [118] and [41].

In order to isolate the response of the ocean to atmospheric forcing in terms of sea level, both the low frequency response to variations in atmospheric pressure (with periods of half a day or longer, known as the "inverse barometer correction") and the high frequency atmospheric forced variability (such as wind effects) have to be taken into account. This "atmospheric correction" has to be applied to both TGs and altimetry data and therefore a common source is needed. This is provided by the Dynamic Atmosphere Correction (DAC) [119]. In the version applied to ALES data, the MOG2D barotropic atmospheric model is forced by the ECMWF (European Centre for Medium-Range Weather Forecasts) operational analysis (with inputs every 6 hours) and has a spatial sampling of 0.25° .

In order to compare these results with the latest altimetry products, the same analysis described in section 5.3.2 has been applied to gridded altimetric data (Level 4) and to Envisat along-track data (Level 2) from the ESA SL_cci project. The gridded product consists of a 1/4-of-degree regular spaced grid with monthly sea level anomalies that combine all the available satellite altimetry data (Jason-1/2, Envisat, ERS-2, Topex/Poseidon and GFO missions in the same time span), while the along-track product is directly comparable with ALES data, since the two products refer to the same points in time and space.

In the DAC correction applied to the SL_cci dataset, MOG2D is forced by ERA-Interim atmospheric reanalyses, which guarantees stable performance over the time, but at a lower spatial resolution ($0.75^\circ \times 0.75^\circ$). Since the two corrections have generally equivalent performances from 2002 onwards and since higher spatial resolution is appropriate in the coastal ocean, the operational ECMWF-based DAC (downloaded from <http://www.aviso.altimetry.fr>) is applied in this study to both ALES and Envisat SL_cci datasets. The gridded SL_cci product provides sea level anomalies and therefore, given that a gridded version of the ERA-interim based DAC is not yet available, it was not possible to change its atmospheric correction. As previously mentioned, the gridded SL_cci applies a tide correction generated from the GOT

4.8 tidal model, while mean sea surface (DTU13) and wet tropospheric correction (GPD) are the same as in ALES.

To add further consistency to the improvements seen by ALES, which will be described in the next sections, the same analysis is also performed on the 1-Hz Envisat sea level estimations from the Radar Altimetry Database System (RADS, <http://rads.tudelft.nl/>) [120]. By doing so, it is possible to verify that the improvements are not, or not only, due to the fact that ALES does not apply post-processing techniques (such as filtering and merging) adopted in the SL_cci framework, which are suitable for open ocean, but may be not in the coastal environment. The same corrections as for ALES were applied to RADS estimations as well, without any further screening of the data. Although most of the plots and discussions of the next sections do not involve this dataset, the corresponding statistics are shown in tables 5.2, 5.3 and 5.5.

In-situ observations of sea level are provided by the TGs. Here, monthly mean sea level time-series from the Permanent Service for Mean Sea Level (PSMSL) are used at all available TG sites in the study area. Only tide gauges belonging to the Revised Local Reference (RLR) dataset are considered, since this guarantees that the monthly means are reduced to a common datum.

To derive the annual cycle of the steric component (section 5.3.2), the mean monthly temperature and salinity profiles have been computed using the in-situ observations from the KLIWAS gridded climatological dataset (downloaded from <http://icdc.zmaw.de/>) [121].

Wind stress is obtained from the monthly gridded data of NCAR/UCAR Simple Ocean Data Assimilation (SODA) reanalysis (version 2.2.4, downloaded from <http://dsrs.atmos.umd.edu/>). The information on wind stress comes from 20th century reanalysis (CR20 v2) and is provided on a 0.5° x 0.5° grid [122].

5.3 Methods

5.3.1 Data reprocessing

SGDR high-rate waveforms from Envisat missions have been reprocessed with the ALES retracker. Corrections for dry/wet troposphere, ionosphere, sea state bias, dynamic atmosphere effects and tides were applied to the resulting 18-Hz range estimations in order to extract the SSHA.

The high-rate measurements were interpolated onto nominal tracks, as described in [123]. From high-rate waveforms, ALES retracked sea level was then averaged to

generate 1-Hz estimations. Four checks were performed in order to eliminate outliers in the following order:

1. The coastal proximity parameter (CPP) corresponding to the Envisat nominal track points was extracted from the global CPP datafile computed at the National Oceanography Centre Southampton (NOCS) in the context of the ESA SL_cci project. This parameter quantifies the influence of land (taking in consideration not only the distance from the coast, but also its morphology) on the radar returned echoes, and varies from -1 (typical open ocean scenario with no land effects) to +1 (fully inland, no return from sea). In this study, points with a CPP value from 0 to 1 were excluded. A CCP of 0 can be considered as a 'virtual coastline' that delimits the point where, for retracking considerations, the returns from sea and land have equal effect (see [124] for a detailed description).
2. Every ALES retracked 18-Hz waveform is characterised by a fitting error on the leading edge. The fitting error is a measure of how close the fitted waveform is to the real signal and corresponds to the normalised square root of the difference between the modelled waveform and the real signal along the leading edge. Estimations that had a fitting error of over 0.5 (normalised power units) were excluded.
3. Considering that the tidal signal has been removed from the SSHA, 18-Hz estimations outside $[-3m, +3m]$ in absolute value were considered outliers and excluded.
4. The median value and the scaled median absolute deviation (\widehat{MAD}) were computed. Each estimation, x , was evaluated according to the criterion expressed in section 4.3.2.

Concerning the TG dataset, the following criteria were adopted for quality control:

1. Only the PSMSL TGs with data from 2002 to 2012 were used. Among those, only the TG identified by the ID number 1197 in the PSMSL dataset, located in the Western Arkona basin, had several missing values, in 2009 and 2010;
2. The data with a raised "flag for attention" (available in the PSMSL product) were excluded;
3. A maximum absolute value of 50 m was used as a threshold to eliminate clear outliers;

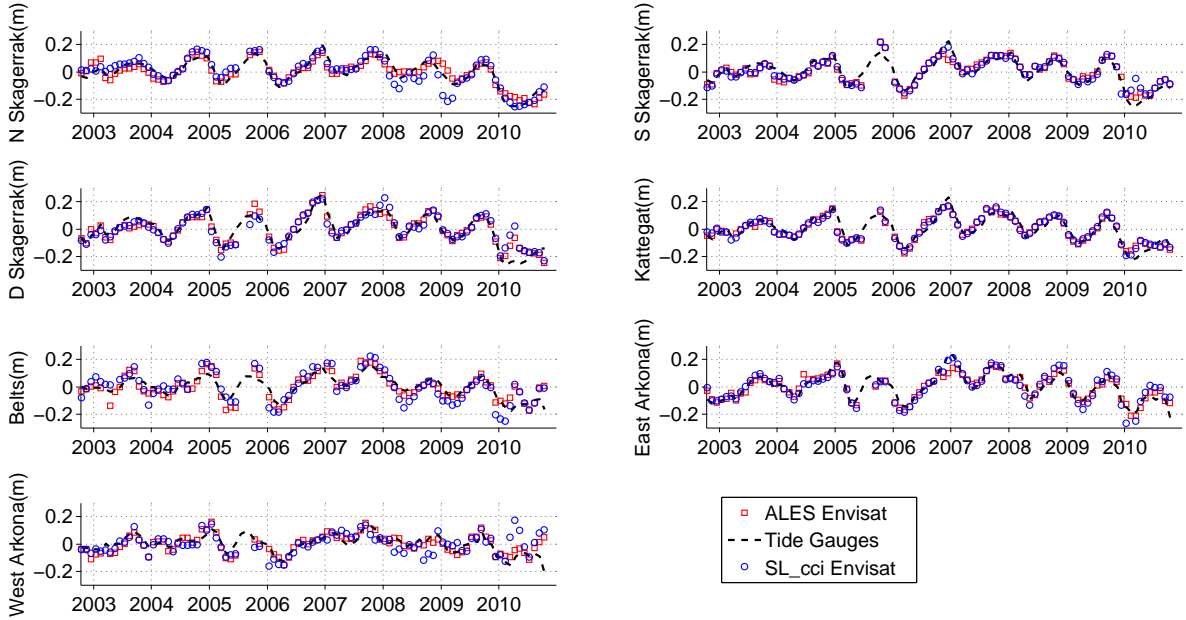


Figure 5.2: Monthly averages of SSHA (with 3-month running mean filter applied) grouped by sub-basin, from TGs (black dashed line) and satellite altimetry within 15 km of the coast for ALES reprocessed dataset (red squares) and Envisat SL_cci (blue circles).

4. The median value and the scaled median absolute deviation (\widehat{MAD}) were computed. Each monthly average, x , was evaluated according to the 3-sigma criterion expressed in section 4.3.2.

Throughout the study, SSHA altimetry time series are formed at various distances from the coast and grouped depending on the geographical definition of each sub-basin. Since the Envisat ground track velocity is about 7 km/s, the sea level measurements from the same cycle and pass are considered to be simultaneous. Therefore, each estimate in the time series corresponds to the median SSHA of all the 1-Hz points from the same pass that fall in the considered geographical interval.

TG data were also grouped depending on the corresponding sub-basin. Since the sea level measured at each TG is relative to a local benchmark, the mean value of all the estimations was subtracted from each monthly average. Time series of sea level from altimetry and PSMSL data are compared in figure 5.2. For this comparison, in order to remove the short-term fluctuations, altimetry data were grouped into monthly means and a 3-month running mean filter was applied to both the datasets.

5.3.2 Estimation of the annual cycle

Model equation

To estimate the annual cycle for all the considered datasets, a harmonic analysis of the time series was performed. The analysis consists of modelling the sea level variability as the sum of a constant, a linear term and a sinusoid wave with an annual frequency. The unknowns (parameters) of this model are the constant term, the slope of the linear term and the amplitude and phase of the sinusoid. Amplitude and phase of the annual frequency are not completely independent parameters, since they are estimated through the same fit, according to the following model:

$$y = A + Bx + C\cos(2\pi xf) + D\sin(2\pi xf) \quad (5.1)$$

where A-D are the coefficients to be estimated and f is the annual frequency. The amplitude (A_m) and phase (P_h) of the annual signal are then computed as follows:

$$A_m = \sqrt{C^2 + D^2} \quad (5.2)$$

$$P_h = \begin{cases} \arctan\left(\frac{D}{C}\right) & \text{if } C < 0 \\ \arctan\left(\frac{D}{C}\right) + \pi & \text{if } C > 0 \end{cases} \quad (5.3)$$

Estimator

The parameters are estimated by a least square minimisation analysis that compares the model with the time series. No running mean is applied to the time series, since this is not beneficial to the estimation, given that it increases the autocorrelation of the residual signal.

A formally correct estimator is needed to solve the minimisation problem. In statistics, the well-known Gauss-Markov theorem states that the Ordinary Least Squares (OLS) estimator is the best unbiased estimator for linear models, i.e. the estimator with the lowest possible variance. This is true if the following assumptions are true as well [125]:

- The expected value of the error is zero
- The error is homoskedastic (i.e. the variance of the error term is the same across all the observations) and not autocorrelated

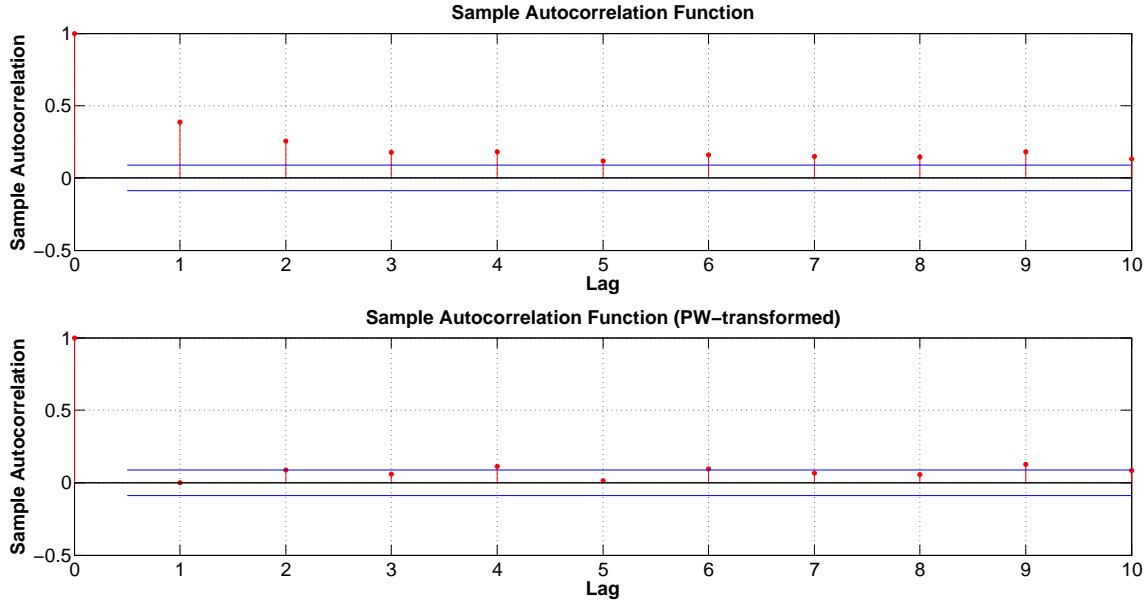


Figure 5.3: Autocorrelation function of the residuals after OLS (above) and PW FGLS annual cycle estimation for the time series of ALES reprocessed altimetry data in the Kattegat Sea within 15 km of the coast. The blue line indicate the 95% confidence bounds of the autocorrelation. The time lag on the x axis is in months.

- There is no perfect multicollinearity, i.e. the independent variables are not in a perfect linear relationship.

For geophysical time series, the autocorrelation of the residuals is a common phenomenon. The error of the model, or residuals, is defined as the difference between the observations and the estimated function values of the linear model at each time step. Figure 5.3 shows an example for the ALES-reprocessed altimetry data in the coastal zone of the Kattegat Sea. The upper plot shows the autocorrelation function of the residual sea level once the estimated annual cycle is subtracted from the 1-Hz sea level estimations in the area within 15 km of the coast. The autocorrelation is the correlation coefficient of a signal with a "copy" of it shifted by an increasing time lag, after the OLS estimation. The first lag on the x-axis indicates an autocorrelation of over 0.4. When the errors (i.e. the residuals of a least square regression) are autocorrelated, the variance-covariance matrix is not a diagonal matrix. Consequently, the OLS estimator is still consistent and unbiased, but is inefficient, i.e. it is not the estimator with the minimum possible variance. In this case the OLS is no longer BLUE (Best Linear Unbiased Estimator) and its standard error estimation is inaccurate.

To obtain a more efficient solution, it is possible to use a generalised least square

regression, in which case the user must make hypotheses about the structure of the unknown error covariance matrix. In standard practice, the so called 'FGLS' (feasible generalised least squares) methods are used. These methods, such as the Prais-Winsten (PW) estimator [126], apply a transformation to the dependent and independent variables in order to transform the problem into one that respects the Gauss-Markov hypothesis. The PW estimator is applied in the present study iteratively. Given a set of independent variables X , observations Y , error ϵ and parameters to be estimated β , the method finds the term ρ that expresses the correlation of the residuals. The steps followed are:

1. Ordinary least squares estimation of the model $Y = \beta X + \epsilon$
2. Ordinary least squares estimation of the model $\epsilon_t = \rho \epsilon_{t-1} + e$ in order to estimate the parameter ρ , which is related to the first order autocorrelation of the residuals
3. Ordinary least squares estimation of the transformed model $Q = \beta Z + e$, in which

$$Q_t = \begin{cases} Y_t \sqrt{1 - \rho^2} & t \equiv 1 \\ Y_t - \rho Y_{t-1} & t \equiv 2 : end \end{cases}$$

and

$$Z_t = \begin{cases} X_t \sqrt{1 - \rho^2} & t \equiv 1 \\ X_t - \rho X_{t-1} & t \equiv 2 : end \end{cases}$$

where t is the time index of the observations. The procedure is iterated until ρ converges to a value close to zero and therefore the errors of the transformed model are no longer autocorrelated. From the lower plot of figure 5.3, which shows the autocorrelation function of the residuals after the PW transformation, it is inferred that the residuals of the transformed problem are not significantly autocorrelated.

Uncertainty

The estimator associates a standard error to each of the estimates. The standard errors on C and D are then combined to provide a standard error on Am and Ph according to the theory of the error propagation. In order to derive the uncertainty, a t-score is computed considering a desired confidence of 95% and the number of degrees of freedom (4 in this case, since 4 parameters are estimated in the regression). The confidence intervals for each estimate are then computed by multiplying the t-score by the standard error.

The use of PW, applied in every estimation in this chapter and in chapter 6, allows for a correct estimation of the uncertainties by applying a least square estimation to PW-transformed time series of n samples that are not anymore auto-correlated and therefore can be considered independent.

A complete analysis of the uncertainty should also include errors coming from drifts in the corrections applied to the altimetry retrievals or residual annual periods caused by imprecise corrections of geophysical signals. The covariance of these errors cannot be inferred from the observations and therefore has to be modelled. Other more complex generalised least squares methods, such as the Bretherton analysis used in dedicated papers such as [127], can take these errors into account together with the autocorrelation issue, but this analysis goes beyond the current scope of this study.

5.3.3 Estimation of the steric height

In order to obtain the steric component of the annual cycle of the sea level, the steric height needs to be derived from the temperature and salinity data at each depth using a climatology. Applying the equation of state described by [128], a density profile at each sampled location was derived from the records of temperature and salinity.

The assessment of the steric sea level variations from the density profiles is based on the integral method, also followed by previous studies and described in detail by [129]. The steric height η_{st} is a measure of the vertical thickness by which a water column expands or contracts when its specific volume changes. Steric height and ocean density are related by

$$\begin{aligned}\eta_{st}(\lambda, \phi, z_1, z_2, t) &= \int_{z_1}^{z_2} \left(\frac{1}{\rho(\lambda, \phi, z, t)} - \frac{1}{\rho_0(z)} \right) \rho_0(z) dz \\ &\approx - \int_{z_1}^{z_2} \frac{\rho(\lambda, \phi, z, t) - \rho_0(z)}{\rho_0(z)} dz\end{aligned}\tag{5.4}$$

for $\frac{|\rho(\lambda, \phi, z, t) - \rho_0(z)|}{\rho_0(z)} \ll 1$ [130, 131]. Here $\rho_0(z)$ is a constant standard reference density (usually at temperature $T_0 = 0^\circ\text{C}$ and salinity $S_0 = 35$) and $\rho(\lambda, \phi, z, t)$ is the density as a function of geographical position, depth and time. The limits of the integration, z_1 and z_2 , are the depths of two pressure levels P_1 and P_2 with $z_1 = z(P_1)$ and $z_2 = z(P_2)$ respectively.

Following [130], a time-variable fraction η'_{st} can be separated from the mean steric

sea level change over the entire time span $\bar{\eta}_{st}$ by

$$\eta'_{st} = \eta_{st} - \bar{\eta}_{st} = - \int_{z_1}^{z_2} \frac{\rho(\lambda, \phi, z, t) - \rho_0(z)}{\rho_0(z)} dz + \int_{z_1}^{z_2} \frac{\bar{\rho}(\lambda, \phi, z) - \rho_0(z)}{\rho_0(z)} dz \quad (5.5)$$

$$= - \int_{z_1}^{z_2} \frac{\rho(\lambda, \phi, z, t) - \bar{\rho}(\lambda, \phi, z)}{\rho_0(z)} dz. \quad (5.6)$$

The mean density $\bar{\rho}(\lambda, \phi, z)$ is obtained by averaging the observations at all pressure levels for every grid square.

5.4 Results and discussion

5.4.1 Altimetry data quality

A preliminary analysis is conducted on the two along-track altimetry datasets. Figure 5.4 shows the improvements of reprocessed altimetry compared to the SL_cci dataset in terms of quantity and quality of the data. The upper plots show the number of the available cycles in both the datasets. It is important to stress that at this stage ALES data have already been quality-controlled and therefore the statistics represent the number of measurements that are then used in the sea level analysis. Envisat SL_cci has gaps in the Belts and Arkona basins, as well as within 15 km of the coast in the whole domain. ALES includes all the available cycles and the only missing points are due to passes where no waveforms are available in the SGDR files. The availability is uniform across the whole domain.

An increased amount of data is not helpful if the quality of the retrievals is poor. As a first evaluation, the lower plots of figure 5.4 show the standard deviation (std) of the SSHA time series at each 1-Hz location. In order to be consistent, the std of SSHA is expected to vary smoothly with no abrupt changes between consecutive 1-Hz points. This is verified in ALES with the exception of very few unrealistic values. The Envisat SL_cci dataset shows evident signs of corrupted estimations. The most problematic areas are again the Arkona basin, the Belts and the last 15 km from the coast, but unrealistic variability in the SL_cci SSHA values is seen also in the Skagerrak and Kattegat open seas.

The histogram in figure 5.5 shows the distribution of the RMS of the SSHA time series at each 1Hz-point in the area of study. The variability of ALES is slightly smaller than the Envisat SL_cci. Overall, SL_cci has more locations where the RMS level is higher than the average variability in the area and in particular more than 7% of the points with an unrealistic RMS larger than 40 cm. The histogram shows

also the RMS from RADS dataset, which performs worse than the others, proving that dedicated retracking and post-processing are able to increase the overall quality of the estimations.

The comparison is helpful to understand what are the issues that dataset meant for open ocean applications have to face in the coastal ocean. At the current stage, the SL_cci does not involve any specialised coastal retracking strategy. The SL_cci sea level estimations come from the standard products of each mission (i.e. from the fitting of the full waveform Brown model optimised as explained in Section 3.1). Figures 5.4 and 5.5 demonstrate that despite the quality control, which eliminates several 1-Hz points close to land, there are several unrealistic estimations left, although the number of outliers is halved if compared to the RADS archive, which uses the same data of SL_cci, but does not initially involve any special quality control. Of course and as seen in the previous validation, most of the estimations coming from the standard ocean retracking are still valid, which explains why the data distribution is nearly the same of ALES. The added value of this coastal altimetry strategy is indeed to provide a more reliable product, while maximising the number of retrievable sea level heights.

5.4.2 Time series of sea surface height anomaly

Averaged time series of SSHA from TGs and 1-Hz altimetry locations within 15 km of the coast are shown for each sub-basin in figure 5.2. There is good agreement between the in-situ and the remotely sensed sea level. Correlation coefficients between the time series are listed in table 5.1. ALES data are better correlated with TGs than Envisat SL_cci data across the whole area of study, except a 0.01 improvement in the correlation of Envisat SL_cci in the Kattegat sea. Nevertheless in this computation a 3-months running mean filter was applied and therefore the resultant time series are considerably autocorrelated. The difference in correlation might not be significant, since the samples of the time series are not independent. In order to test the datasets, as previously said, the following sections avoid the autocorrelation by using the PW FGGS estimation and by not applying any filtering.

The Skagerrak, the Kattegat and the East Arkona sub-basins show a very similar behaviour and the annual signal dominates their variability, while this periodicity is less evident in the Belts and the West Arkona sub-basins. Even in these two regions though, the TGs and ALES coastal altimetry time series show good agreement, with correlation coefficients above 0.8, while Envisat SL_cci data are poorly correlated with the in situ time series of West Arkona. In all the area of study, even over the short timescale assessed, there are significant interannual variations. In particular,

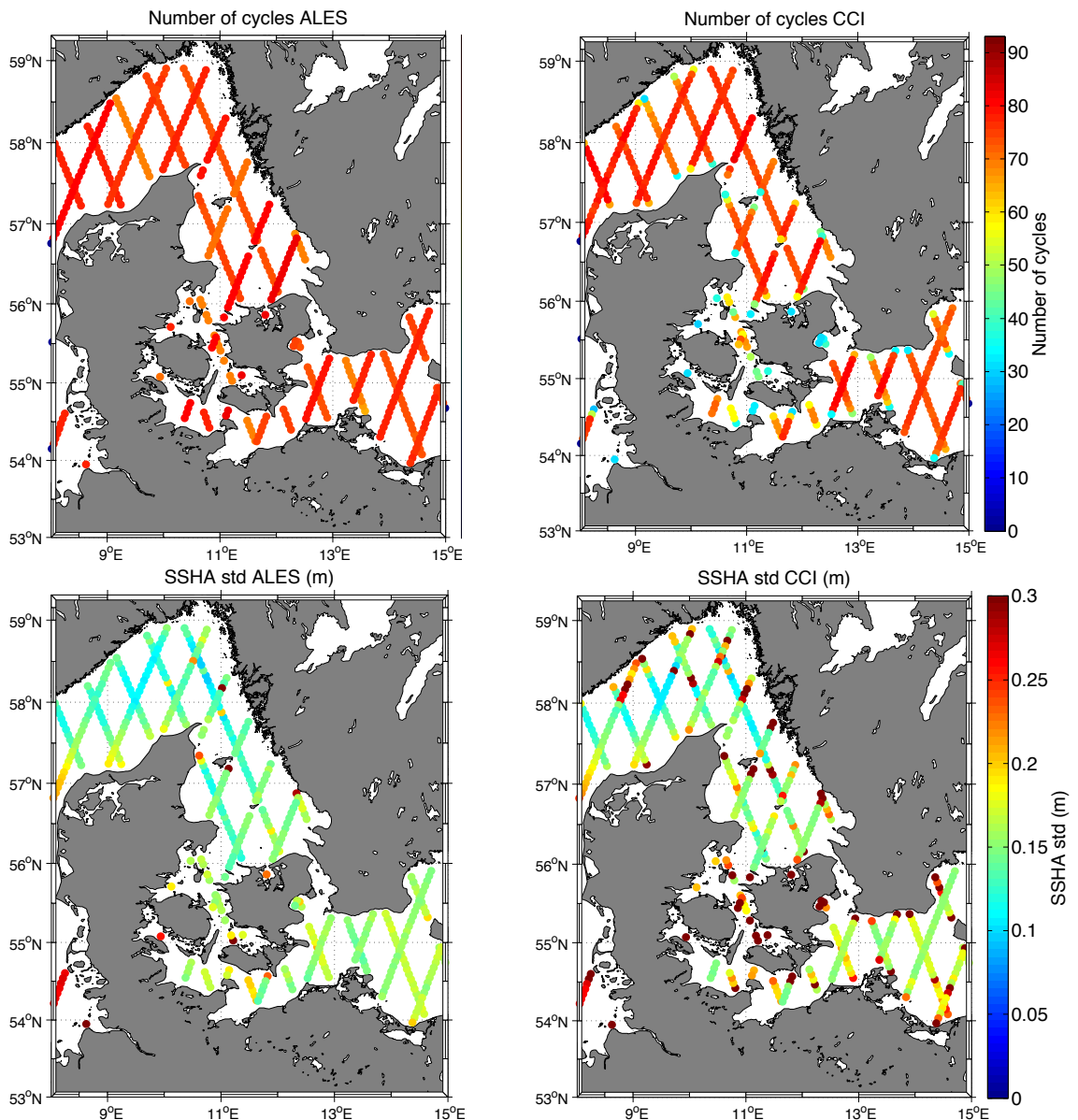


Figure 5.4: Comparison between ALES reprocessed (left) and Envisat SL_cci (right) datasets in terms of number of cycles available (upper plots) and standard deviation of the SSHA time series (lower plots) for each 1-Hz location.

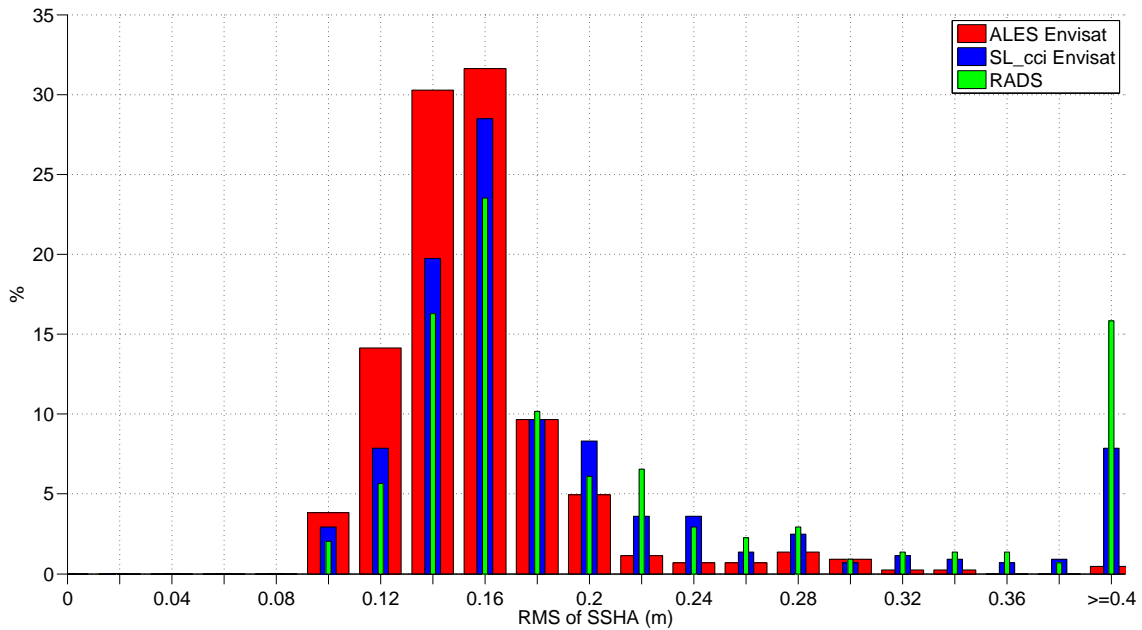


Figure 5.5: Histogram of the root mean square of SSHA computed at each 1-Hz location from ALES reprocessed (red), Envisat SL_cci (blue) and RADS (green) datasets.

Sub-basin	CORR ALES - TG	CORR SL_cci - TG
Kattegat	0.92	0.93
Norway Skagerrak	0.91	0.89
Denmark Skagerrak	0.92	0.86
Sweden Skagerrak	0.91	0.90
West Arkona	0.82	0.48
East Arkona	0.92	0.91
Belts	0.85	0.82

Table 5.1: Correlation (CORR) coefficient between altimetry and tide gauges (TG) sea level monthly-averaged time series for each sub-basin (3-months running mean filter applied).

from the middle of 2006 to the end of 2008 the anomalies are almost constantly of positive sign.

Past studies [104, 132, 106] have shown the importance of the wind patterns and their fundamental role in the transport of water masses. Winds in the area are westerlies, easterlies or southeasterlies but the westerly winds are predominant and reach their highest speed in autumn and winter, when the passing of low pressure systems increase the storm activity [133]. Westerlies bring water from the North Sea and the Atlantic into the Skagerrak and the Kattegat Sea, while easterlies drive the outflow into the North Sea. In this study, coastal altimetry data within 15 km from the coast confirm the variability of the sea level in the annual time scale due to persistent winds redistributing waters: Figure 5.6 provides a verification by comparing the monthly averaged ALES reprocessed SSHA of the Sweden Skagerrak coast with the monthly averaged zonal wind stress in the entire Skagerrak area. The two curves have a correlation coefficient of 0.63, which is a significant indication of the influence of wind patterns on sea level. All the maxima in the sea level coincide with strong westerly wind events and the lowest SSHA are found during easterlies. The time of appearance of strong westerlies act as a phase regulator for the sea level. For example, in 2004/2005 and 2006/2007 winters the time of high sea level and strong westerlies is December/January, while in 2008/2009 and 2009/2010 this happens in October/November. January of 2010 is the month with the strongest negative anomalies of sea level and coincides with the strongest easterlies found in the time series.

5.4.3 Pointwise estimation of the annual cycle

In this section the spatial variability of the annual cycle is assessed, as well as the ability of Envisat to capture it. Figure 5.7 shows the amplitude of the annual cycle derived at each 1-Hz point of the tracks for ALES reprocessed dataset and Envisat SL_cci and at each grid point of the merged SL_cci dataset. The corresponding estimates from the TG data are shown on the figure with squares. For the along-track altimetry, only 1-Hz points where at least 5 years of data are available (~ 50 Envisat cycles) have been included, which is why the Envisat SL_cci does not have some coastal estimations and there are voids in Belts and West Arkona.

Since for the pointwise analysis time series are generated with a frequency of one measurement every 35 days, the estimated annual cycle will include the contribution coming from any error in the tidal correction for the K1 constituent (which has an aliasing period of 365.24 days) [134]. The Rayleigh period computed for the K1 aliased frequency and the annual frequency, i.e. the minimum time span of a time

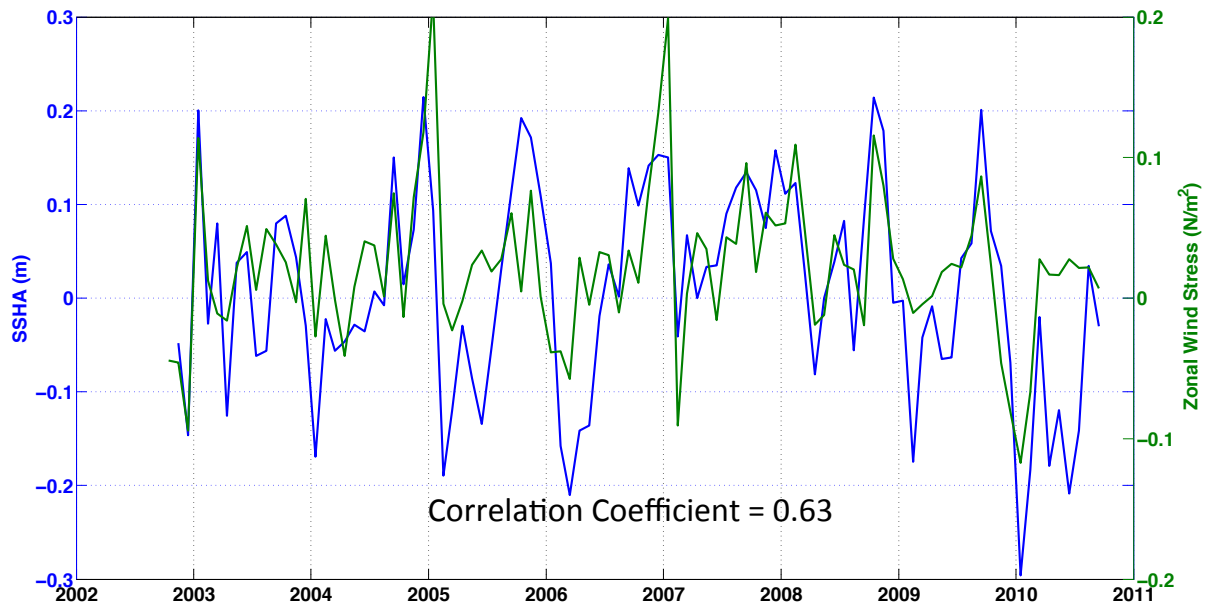


Figure 5.6: Monthly averages of zonal wind stress from 20 century (CR20 v2) reanalysis (in green) and of SSHA (in blue) from ALES dataset within 15 km of the coast in Sweden Skagerrak.

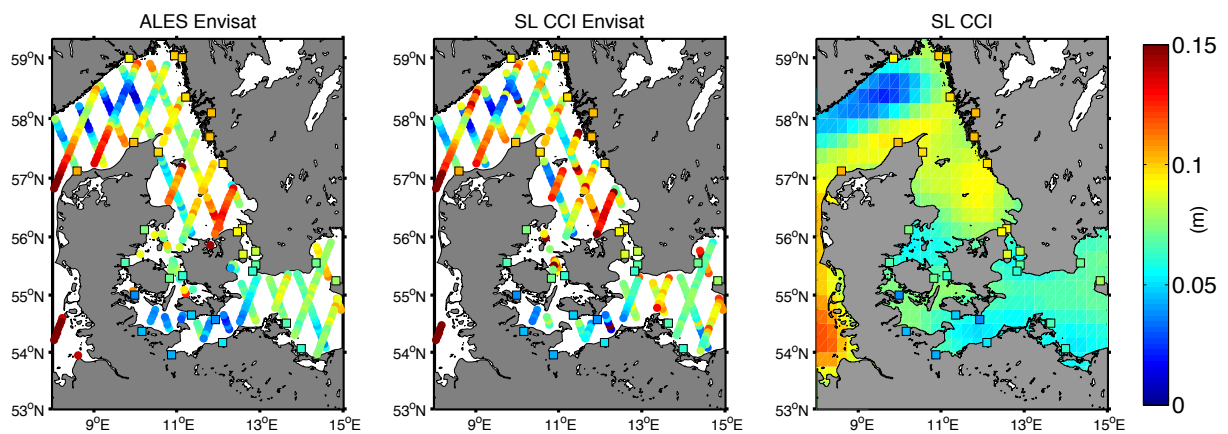


Figure 5.7: Estimates of annual cycle amplitude from TG data (squares) and 1-Hz altimetry points along the Envisat tracks for ALES reprocessed dataset (left) and Envisat SL_cci (centre). The plot on the right shows the estimates from gridded SL_cci.

Sub-basin	ALES (m)	SL_cci Env (m)	RADS (m)
Kattegat	0.024	0.056	0.053
Norway Skagerrak	0.037	0.035	0.037
Denmark Skagerrak	0.041	0.040	0.035
Sweden Skagerrak	0.001	0.031	0.031
West Arkona	0.040	0.022	0.057
East Arkona	0.012	0.016	2.767
Belts	0.008	0.022	0.003

Table 5.2: Mean crossover differences of the annual cycle of the sea level (amplitude) for each sub-basin.

series needed to separate two different periodic signals, is therefore virtually infinite and the two signals are indistinguishable in the pointwise analysis. Nevertheless, the estimations used for validation, coming from TGs that measure the sea level every few minutes, are not affected by this aliasing.

The annual signal in the Belts and Arkona regions shows a marked difference from the Kattegat/Skagerrak in terms of amplitude, which is well captured both in ALES and in the merged SL_cci, although the merged SL_cci data overestimate the amplitude in the westernmost part of the West Arkona area. As the merged product used a different tidal model, this discrepancy may be caused by unresolved tidal signal.

Table 5.2 shows, for each sub-basin, the average difference in the amplitude estimation of the annual cycle at the crossovers. ALES improves the statistics by a factor of two or more in the Kattegat and in the Belts; it is the only dataset to have a crossover agreement below the centimetre level (in the Sweden Skagerrak and in the Belts). The Envisat SL_cci improves the agreement by a factor of two in the only crossover point of the West Arkona. The table also shows the statistics for RADS, whose performances are generally worse than ALES and similar to SL_cci, although results are significantly worse in the Arkona Basin and marginally better (~ 0.5 cm) in the Denmark Skagerrak and in the Belts.

Areas of disagreement between ascending and descending tracks are present in both ALES and Envisat SL_cci datasets, particularly along the Danish coasts, where the ascending tracks estimate a higher amplitude compared to the descending ones. These differences are caused by the intrinsic problem of using a single point along an Envisat track to estimate the annual cycle: since Envisat has a sun-synchronous orbit, ascending passes and descending passes respectively cross the equator at 10pm

local time and 10am local time. Errors in the corrections that have a daily cycle can affect the crossover differences and this is particularly true for errors in the K1 tidal constituent, since they are aliased in the annual cycle [63].

Table 5.3 reports the mean difference in the amplitude estimation of the annual cycle estimated from the tide gauges and the closest 1-Hz altimetry point for each sub-basin. The estimates at each 1-Hz point are less accurate than the sub-basin averages, due to the relatively small number of repeated observations. Due to the uncertainty associated with the difference of the estimations, the following comparison will only be based on the best estimates, but cannot be considered statistically relevant. The multi-mission merged SL_cci scores slightly better, benefiting from the optimal interpolation of more measurements from missions with different sampling characteristics. ALES scores better than or equal to Envisat SL_cci in all basins except the Norway Skagerrak, although the comparison is affected by the fact that the Envisat SL_cci does not include some of the coastal 1-Hz locations due to the lack of data. The last column of the table reports the statistics for RADS. Performances are significantly worse in four sub-basins, with differences of over 10 cm compared to the tide gauges, while RADS scores better than ALES within a cm level in the Skagerrak Sea.

RADS performs particularly bad in Eastern Arkona. To understand the reason, the std of the RADS SSHA time series for each 1-Hz location is plotted in Figure 5.8. Two tracks with unrealistically high std are found in Eastern Arkona. Systematic errors are therefore present in some cycles of the RADS archive for these tracks, which are not due to problems in coastal altimetry. SL_cci performs better despite the use of the same retracking scheme of RADS because the 1 Hz data of SL_cci are post-processed and flagged: the systematic errors are not present, as evident from figure 5.4. Nevertheless, the aim of this study is to compare different datasets that are available to the users, without any further flagging.

In the along-track datasets, a slope in the amplitude of the annual cycle is visible in the Skagerrak Sea, with higher values near the coast and low values in the open sea. The change matches the change in bathymetry. The area of low amplitude of the annual cycle corresponds precisely with the extension of the Norwegian Trench. It is known that the annual cycle can show spatial complexity that depends on factors that include wind-driven barotropic processes in shallow semi-enclosed seas, and that coastal regions can be characterised by elevated amplitudes [53]. In this case, the evolution of the annual cycle amplitude with depth is in agreement with the circulation pattern of the region, characterised by a wide current in Denmark Skagerrak and a narrow coastal current along the coast of Norway, whose extension

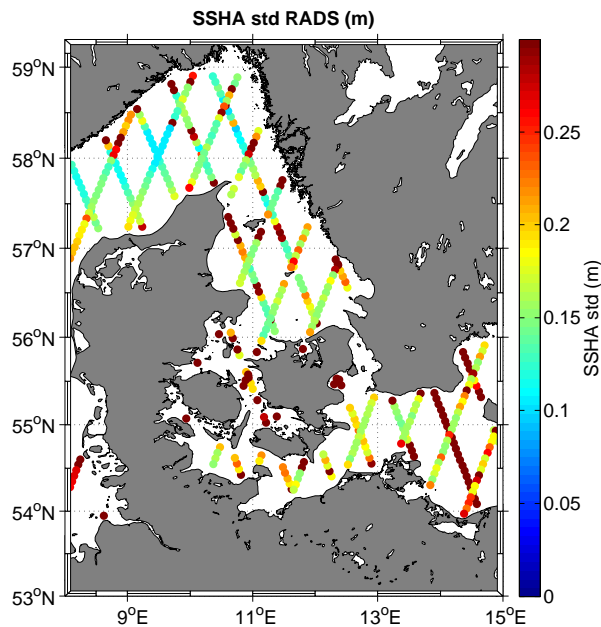


Figure 5.8: Standard deviation of the SSHA RADS time series for each 1-Hz location.

Sub-basin	ALES (m)	SL_cci Env (m)	SL_cci (m)	RADS (m)
Kattegat	0.026 ±0.021	0.067±0.070	0.016±0.010	0.153±0.128
Norway Skagerrak	0.027 ±0.038	0.013±0.064	0.021±0.025	0.012±0.070
Denmark Skagerrak	0.029 ±0.021	0.029±0.042	0.014±0.017	0.029±0.040
Sweden Skagerrak	0.023 ±0.012	0.023±0.017	0.020±0.013	0.016±0.016
West Arkona	0.022 ±0.020	0.020±0.030	0.022±0.007	0.211±0.131
East Arkona	0.012 ±0.017	0.028±0.039	0.008±0.007	1.630 ±1.138
Belts	0.013 ±0.024	0.015 ±0.045	0.007±0.008	0.093±0.093

Table 5.3: Mean difference of the annual cycle of the sea level (amplitude) estimated from the TG dataset and the closest 1-Hz altimetry point for each sub-basin.

in the open ocean is delimited by the presence of the deep Norwegian Trench. The high amplitudes of the annual cycle along the Norwegian coast of the Skagerrak Sea, captured also by the local TG, are less identifiable in the gridded product, probably due to its grid size.

5.4.4 Sub-basin estimation of the annual cycle

To get a more robust estimation of the annual cycle, the harmonic analysis has been performed by grouping the 1-Hz points of each track according to the corresponding sub-basin. By doing so, the time series of each sub-basin use multiple Envisat tracks and have a more frequent sampling, limiting the problem of the K1 aliasing period previously mentioned.

Figure 5.9 and table 5.4 show the results of the annual cycle amplitude estimation performed with the PW estimator in each sub-basin for the TGs, for Envisat altimetry at different distances from coast (from ALES reprocessed dataset and SL_cci), and for the gridded SL_cci product.

Statistically speaking, all the coastal estimations from any of the datasets fall within the error bars of the tide gauges estimate. The following discussion is based on comparisons of the best estimates and therefore is undermined by the issue of statistical significance.

The estimates from ALES altimetry points closest to the coast agree with the TG estimates to within 1 cm for all the sub-basins with the exception of Norway Skagerrak, showing a significant improvement w.r.t. the comparison between TG and closest 1-Hz point estimates shown in table 5.3. It is possible to conclude that on a sub-basin scale the ALES reprocessed dataset is able to give the most reliable coastal annual cycle amplitude estimations and the improvements are particularly felt in the East and West Arkona sub-basins. For the Norway Skagerrak, the increase of the annual amplitude from the deeper area to the coast is well represented by the transition from the ALES altimetry data to the TG.

The gradient of the amplitude of the annual cycle from the coast to the open sea is an important example of a characteristic that it is not possible to derive from a TG-based analysis. The gradient follows the bathymetry of the area, which drops from few metres to hundreds of metres of depth in a few km (see figure 5.1). The high coastal amplitude is very similar to the annual cycle of the Kattegat Sea and the shallow areas of the Skagerrak Sea. This is in accordance with the general circulation pattern, since the Norwegian Coastal Current is the returning flow of the Jutland current, which incorporates the outflow of the Kattegat Sea. The strong seasonal variability of the current has previously been noted in results from circulation models

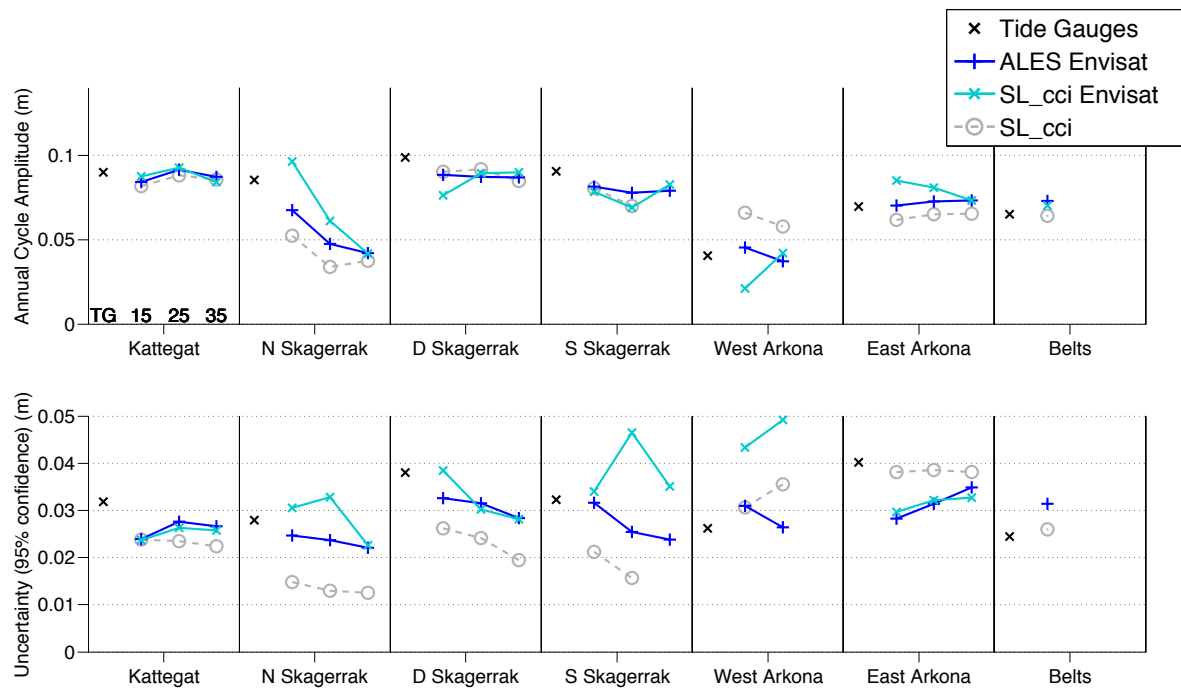


Figure 5.9: Estimates of the amplitude of the annual cycle of the sea level (top) and corresponding uncertainty at 95% level (bottom) for each sub-basin from TG data (black cross) and altimetry within 15 km of the coast, from 15 to 25 km and from 25 to 35 km (left to right in each sub-basin box). The estimation is performed with the PW method. The estimates come from ALES reprocessed dataset (blue), Envisat SL_cci (cyan) and gridded SL_cci (grey).

Sub-basin	Alt data set	TG (m)	within15 km (m)	15-25 km (m)	25-35 km (m)
Kattegat	ALES	0.090 ±0.032	0.084 ±0.024	0.091 ±0.028	0.087 ±0.027
	SL_cci Env	”	0.087 ±0.024	0.093 ±0.026	0.084 ±0.026
	SL_cci	”	0.082 ±0.024	0.088 ±0.024	0.086 ±0.022
N Skagerrak	ALES	0.085 ±0.028	0.067 ±0.025	0.048 ±0.024	0.041 ±0.022
	SL_cci Env	”	0.096 ±0.030	0.061 ±0.033	0.042 ±0.023
	SL_cci	”	0.052 ±0.148	0.034 ±0.013	0.037 ±0.013
D Skagerrak	ALES	0.097 ±0.038	0.088 ±0.033	0.087 ± 0.032	0.087 ±0.028
	SL_cci Env	”	0.076 ±0.039	0.089 ±0.030	0.090 ±0.028
	SL_cci	”	0.090 ±0.026	0.091 ±0.024	0.085 ±0.020
S Skagerrak	ALES	0.091 ±0.032	0.081 ±0.032	0.077 ± 0.026	0.080 ±0.024
	SL_cci Env	”	0.078 ±0.034	0.069 ±0.047	0.083 ±0.035
	SL_cci	”	0.081 ±0.021	0.070 ±0.016	/
West Arkona	ALES	0.0403 ±0.026	0.044 ±0.031	0.037 ±0.026	/
	SL_cci Env	”	0.021 ±0.043	0.042 ±0.049	/
	SL_cci	”	0.066 ±0.031	0.058 ±0.036	/
East Arkona	ALES	0.070 ±0.040	0.070 ±0.028	0.073 ±0.032	0.073 ±0.035
	SL_cci Env	”	0.085 ±0.030	0.081 ±0.032	0.073 ±0.033
	SL_cci	”	0.062 ±0.038	0.065 ±0.039	0.065 ±0.038
Belts	ALES	0.065 ±0.024	0.073 ±0.031	/	/
	SL_cci Env	”	0.070 ±0.050	/	/
	SL_cci	”	0.064 ±0.026	0.066 ±0.021	/

Table 5.4: Results of the PW amplitude estimation for the annual component of the sea level in the years 2002-2010 for each sub-basin. For each altimetry dataset, i.e. ALES Envisat, SL_cci Envisat and gridded SL_cci, the estimation is performed considering 1-Hz altimetry points within 15 km of the coast (column 4), from 15 to 25 Km (column 5) and from 25 to 35 Km (column 6). The same PW estimation is applied to the tide gauges and reported in column 3. All the uncertainties are referred to the 95% confidence level.

[115].

There is a clear border between the West and the East Arkona sub-basins in terms of different amplitude of the annual cycle. In addition, it is known that the exchange of water between the Arkona and the Kattegat is different in the two sub-basins, because they are well separated by the Darss Sill and, according to [116], the exchange of water between the Kattegat and the Baltic Sea is faster and more direct through the Oresund Strait than through the channels in the Belts and the West Arkona sub-basin. Further evidence of these differences is found in section 5.4.5 investigating temperature and salinity profiles.

Given the agreement of coastal data with tide gauge estimates, these results represent a step forward compared to previous analysis of the area, which avoided using coastal data due to the lack of validated products [6, 106, 108].

In the lower plot of figure 5.9, the uncertainties are shown with the 95% confidence interval, which corresponds to roughly twice the standard error. They are generally smaller, but still of the same order of magnitude as the estimates, due to the short time series considered. The estimates from Envisat SL_cci data in the Belts and the West Arkona regions are exceptions, since uncertainties are higher due to the limited amount of valid data. Uncertainties of the estimates for TGs could be reduced by using high frequency data rather than the monthly means provided by the PSMSL service. Concerning altimetry, the only feasible solution to increase the reliability is to extend the time series. The Jason series is currently the longest that it is possible to reprocess with the ALES retracker, but the coarser spatial coverage could affect the retrieval of differences between small sub-basins, such as the West Arkona area considered in this study. The availability of missions that improve the density of tracks and with enhanced coastal capabilities, such as AltiKa, CryoSat-2 and soon Sentinel-3, is promising in terms of future extensions. The very recently completed reprocessing of the ERS-1/2 missions via the REAPER ("Reprocessing of Altimeter Products for ERS" [135]) study calls for a similar assessment of the coastal capabilities of such sensors.

The results of the phase estimation are shown in figure 5.10. The points represent the period of the year when the maximum of the annual cycle occurs. As for the amplitude component, also the differences in the phase estimation are not statistically significant when considering the error bars and only a comparison based on the best estimates is here attempted. Coastal estimates from ALES and SL_cci products are in agreement with TGs estimates within a few days in every sub-basin. The maxima for all sub-basins happen in late autumn. Considering only the wind stress driver, the sea level maxima would be expected later in winter, at the end

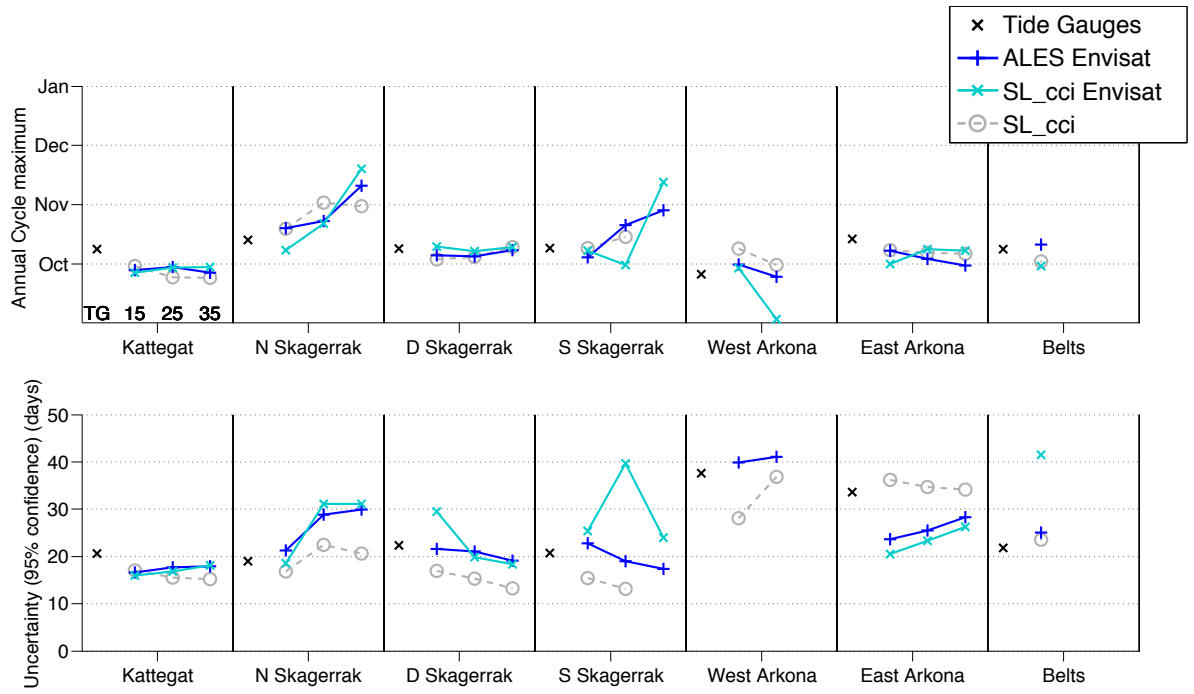


Figure 5.10: Estimates of the phase of the annual cycle of the sea level (top) and corresponding uncertainty at 95% level (bottom) for each sub-basin from TG data (black cross) and altimetry within 15 km of the coast, from 15 to 25 km and from 25 to 35 km (left to right in each sub-basin box). The estimation is performed with the PW method. The estimates come from ALES reprocessed dataset (blue), Envisat SL_cci (cyan) and gridded SL_cci (grey). The estimates correspond to timing of annual cycle maximum.

of the season of strong westerlies that push water mass in from the North Sea. On the other hand, the thermal expansion of the surface and sub-surface waters in the Northern Hemisphere is expected at the end of the summer season. It is here argued that the late-autumn maxima are a consequence of the phase shift between the mass and the steric component of the annual cycle and the verification is provided in the next section.

Table 5.5 shows, for each sub-basin, the RMS difference between the annual signal estimated by the averaged time series computed from the TGs and the annual signal estimated from the different altimetry datasets using the data within 15 km of the coast. As done previously, the TGs estimates represent the ground truth. In this way, it is possible to provide an objective evaluation that considers phase and amplitude at the same time. Taking in consideration the high level of uncertainty, the differences between the datasets are not statistically significant. Considering

Sub-basin	ALES (m)	SL_cci Env (m)	SL_cci (m)	RADS (m)
Kattegat	0.010±0.045	0.019±0.034	0.011±0.039	0.023±0.036
Norway Skagerrak	0.016±0.037	0.022±0.040	0.024±0.040	0.028±0.048
Denmark Skagerrak	0.009±0.060	0.008±0.040	0.009±0.049	0.012±0.039
Sweden Skagerrak	0.007±0.052	0.010±0.040	0.007±0.049	0.013±0.039
West Arkona	0.005±0.046	0.031±0.052	0.020±0.040	0.024±0.068
East Arkona	0.006±0.063	0.016±0.036	0.007±0.053	0.772±1.093
Belts	0.007±0.030	0.008±0.052	0.005±0.041	0.026±0.073

Table 5.5: RMS of the difference between the sinusoids corresponding to the annual cycle of the sea level estimated by the tide gauges and the sinusoids estimated from the different altimetry datasets for each sub-basin (only data within 15 km of the coast).

an evaluation based on the best estimates of the RMS, the sinusoids obtained from ALES coastal data are everywhere more similar to the signal derived from the TGs than the corresponding Envisat SL_cci estimations. Compared to the multi mission gridded SL_cci, ALES improves the estimations in the Norway Skagerrak and in the West Arkona, while the gridded dataset has a more accurate annual cycle estimation in the Belts. The sinusoids from ALES are the only data with an RMS difference that does not exceed 2 cm in every sub-basin. The last column of the table shows the same statistics for RADS, whose RMS is higher than any of the other datasets in every sub-basin, except for the West Arkona, where RADS scores slightly better than Envisat SL_cci. This proves that the improvements seen in the estimation of the annual cycle of the sea level from ALES are directly related to the quality of the retracked data and are not simply a consequence of different post-processing techniques.

[55] recently performed a similar study comparing the annual cycle from tide gauges and from AVISO gridded product in the same area (Figure 5 of the same article). In terms of RMS difference between the annual harmonics, they found agreement within ∼2 cm in the whole area, except in the West Arkona, where they found differences of over 4 cm. The present analysis in the same sub-basin demonstrates not only that the SL_cci gridded product obtains better results, which might be due to the different corrections applied and/or to the different time frame considered, but also the significative improvement in RMS difference brought by the use of ALES data, which brings the statistics below the cm level.

Overall, the results obtained from the altimetry dataset in this research stress the

Sub-basin	TG (m)
Kattegat	0.009±0.023
Norway Skagerrak	0.013±0.018
Denmark Skagerrak	0.016±0.028
Sweden Skagerrak	0.013±0.023
West Arkona	0.009±0.024
East Arkona	0.002±0.031
Belts	0.002±0.017

Table 5.6: Amplitude of the semiannual cycle of the sea level estimated by the tide gauges for each sub-basin.

importance of a dense data coverage in such high-variability areas. [106] condensed the annual cycle of the Baltic Sea detected by satellite altimetry to a single point in the open sea; This research argues that a sub-basin analysis from the coast to the open sea is reliable (as confirmed by the comparison with the tide gauges) and it highlights considerable differences in the amplitude of the annual cycle within different areas of the Baltic Sea (West Arkona, East Arkona).

The analysis of the seasonal signal in this chapter is incomplete because it lacks the estimation of the semiannual component in the time series. Table 5.6 shows how the amplitude of the semiannual component estimated from the TG time series in each basin is anyway statistically insignificant. It is therefore argued that the estimation of the semiannual component can be justifiably ignored.

5.4.5 Climatology and steric component of the annual cycle

The annual cycle of the steric height has been derived from in-situ observations stored in the KLIWAS climatologic dataset in order to further improve understanding of the mechanisms driving the annual cycle in sea level and to provide explanations to points raised in the previous section.

Figure 5.11 shows the annual cycle amplitude (left) and the month of the maximum in the steric height annual cycle (right) derived from climatological data.

The amplitude of the annual cycle for the steric component is higher in the Skagerrak Sea than in the rest of the domain and reaches the highest values in the transition zone between the Skagerrak Sea and the Kattegat Sea, where there are the strongest variations of the water column characteristics depending on the penetration of different waters (warmer and more saline from the Atlantic or colder

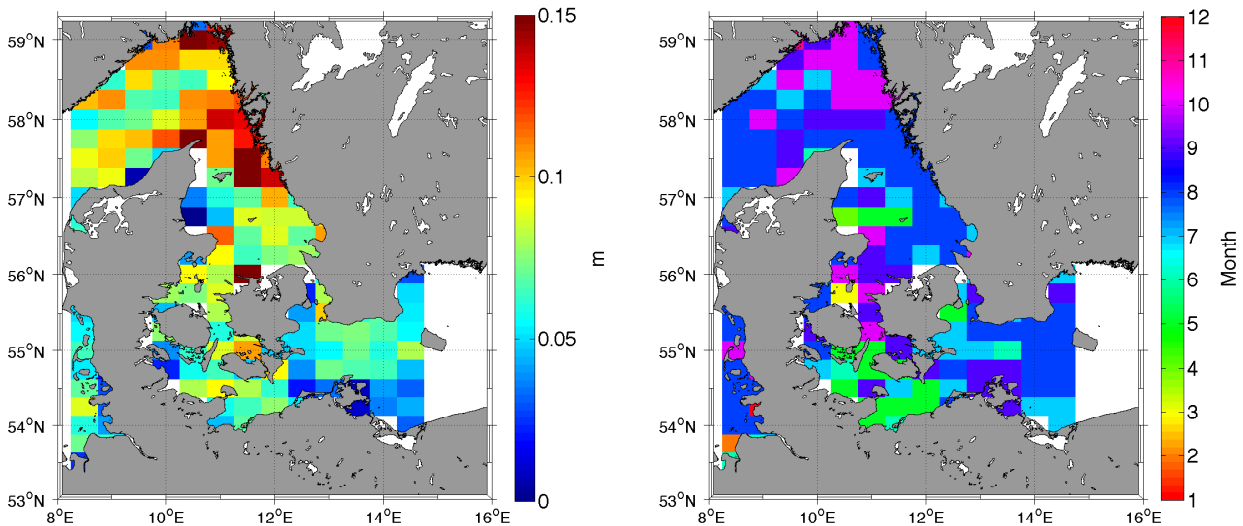


Figure 5.11: Annual cycle amplitude (left) and month of the annual cycle maximum (right) of the steric height derived from climatological data.

and brackish from the Baltic) into the area.

Despite the coarse grid, it is evident that the dynamics in the coastal zone of the Skagerrak Sea are different than in the Norwegian Trench, as already seen in the total sea level annual cycle: the areas with the strongest seasonality follow the circulation pattern of the Jutland Current and the NCC. Nevertheless it has to be noted that some strong shifts in amplitude and phase within adjacent gridpoints are unrealistic and may be a consequence of the unequal sampling of the dataset, both in time and space.

The steric height is maximum in August/September in most of the area, as a consequence of the warming of the top layers of water. The Arkona basin has a distinct phase shift in the steric height annual cycle from the west to the east. The average thermosteric annual cycle (not shown) in the whole Arkona basin has a maximum in August and an amplitude of about 3.5 cm. But the average halosteric component in the West Arkona has an amplitude of 6 cm and a maximum in May, compared to an amplitude of 3 cm and a maximum in late June in East Arkona. The halosteric component of the West Arkona is strongly influenced by the haline Kattegat water influx events, which are more common in autumn/winter[136]. In West Arkona therefore, due to the strong halosteric component, the phase of the

steric component is almost in opposition to the phase of the mass component: as a consequence, the amplitude of the total annual cycle in West Arkona is significantly smaller than in the other sub-basins, as seen in figures 5.7 and 5.9.

The information coming from the climatology gives us key information to interpret the annual cycle derived from satellite altimetry. It is evident that there is a strong mass component that influences the total annual cycle of the sea level, given that the steric cycle is not able to explain entirely the annual signal from altimetry, neither in phase nor in amplitude. By subtracting the steric annual signal from the total annual signal, the estimation of the mass component has been attempted. Figure 5.12 shows the three sinusoids for each sub-basin. The total annual signal was obtained using the ALES coastal time series within 15 km of the coast and the steric component comes from the climatological data just described. As expected, in all the sub-basins the mass component has a winter maximum, coincident with the season of strongest winds, with an amplitude ranging from ~ 7 to ~ 10 cm. The estimations farther from the coast are not shown because they have very similar values; an exception is made for Norwegian and Sweden Skagerrak, where the deeper areas of the Norwegian Trench have a later maximum. This could be due to the presence of an intermediate water layer between about 50 and 300 m, which is warmer in late autumn and early winter than in summer: this phenomenon has been described in [137] and is caused by the penetration of warmer mass from the Atlantic in the Skagerrak Sea and its longer residence time in the intermediate layer. The overall delayed steric height phase in a deep area such as the Norwegian Trench has a direct consequence on the total sea level phase from satellite altimetry, as shown in figure 5.10. The use of gravimetry-derived mass measurements by means of data from GRACE mission, which has recently been attempted in basins of similar scales (the Red Sea, in [138]) could quantitatively assess the mass contribution to the annual cycle and help in validating this attempt. Of course, the spatial scales detectable by GRACE are too large (>300 km), but the use of hydrological models could provide an estimate of the land contribution to mass changes and therefore, by subtraction from the total signal, allow the estimation of water mass variation in the coastal ocean.

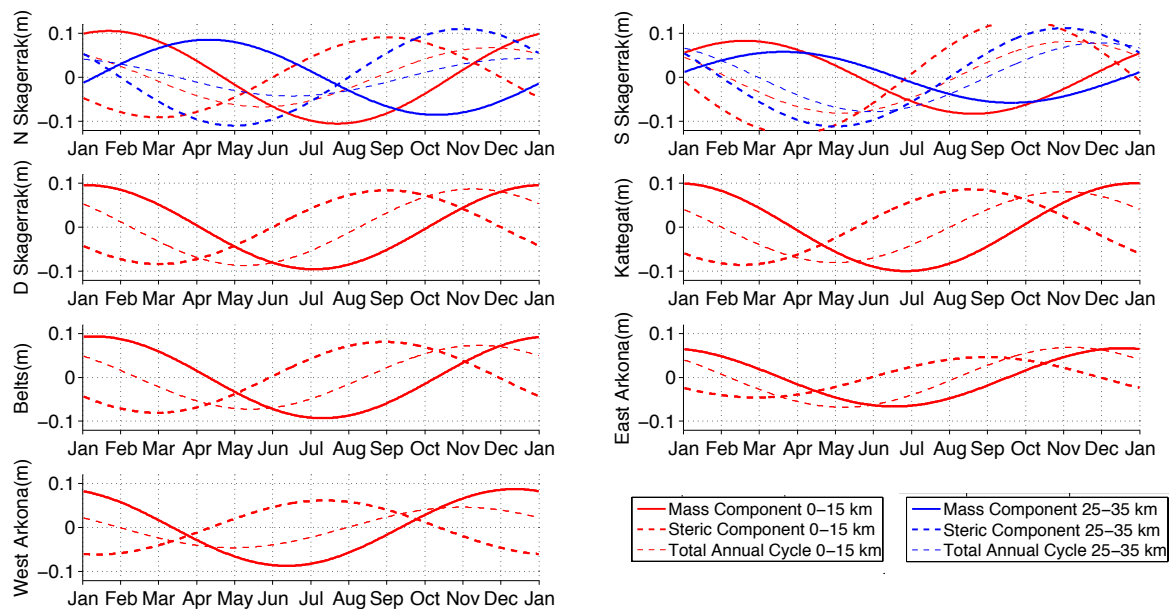


Figure 5.12: Estimates of the sinusoidal signal related to the annual cycle of the mass component of the sea level variability (thick line) for each sub-basin, obtained by subtracting the steric annual signal (estimated from climatology, thick dashed line) from the total annual signal (estimated from ALES dataset, thin dashed line). Estimates are computed from data within 15 km of the coast (red), and from 25 to 35 km (blue).

Chapter 6

ALES application: sea level analysis in the Indonesian seas and expansion to Cryosat-2

The aim of this chapter is to test the feasibility of a multi-mission coastal sea level analysis based on ALES-reprocessed standard altimetry and on the recently generated ocean product from CS-2 in the seas of Indonesia, an area that suffers from the lack of in-situ data despite being of key importance for climate dynamics and a hotspot for sea level rise. CS-2 is the first mission based on the SAR-altimetry principle and is expected to improve the precision of the measurements as well as the data availability in the coastal zone (see section 2.6). The SAR processing is not applied everywhere for CS-2, but part of the seas of Indonesia is included in a so called "SAR box". ESA is currently distributing an experimental ocean product through the SARvatore service. Therefore, the primary objective is to test whether the available product can successfully extend the Envisat-based sea level time series in the area of study on a basin scale.

To the author's knowledge, this is the first time that a SAR-altimetry ocean product is tested for sea level variability analysis and calibrated against a previous mission, while the SAR ocean product from CS-2 has already been cross-calibrated and locally validated against in-situ data and model data in [98].

In order to generate the multi-mission time series of the sea level, data from Envisat and CS-2 are inter-calibrated by means of statistics of crossover differences. Compared to the usual analysis of altimetric time series, this experiment is particularly challenging because of the orbit differences between the two satellites: Envisat had a 35-day repeat cycle, while CS-2 passes over the same ground tracks once every 369 days, with 30-day sub-cycles.

Several studies have pointed out how the sea level in the south-east Asian region is rising at rates higher than the global mean. Recently, [139] have argued that the fast-rising sea level trends of the last two decades in the area could not be the norm and could relax due to the fluctuations of trade winds. They have used reconstruction techniques in order to extend the altimetry analysis in time, but they did not consider any tide gauge located in the wide area that is considered in this chapter. The same authors found that trends increase from the west to the east of the geographical domain, which confirm what [140] have shown. The altimetry data which these studies rely on are gridded and interpolated, while this analysis is based on along-track data averaged according to the distance from the coast. Results based on a scarce number of validated tide gauges and on the interpolation of altimetry data that are not optimised for the coastal zone may cause gaps and lower quality of the measurements, as seen in the previous chapter. At the same time, given the highly populated coastal areas, it is beneficial to improve the quality of altimetry data in order to understand the dynamics of the sea level close to the coast and on smaller scales. An altimetry-based sea level study in the region is also particularly needed considering that [141] have proved that local tide gauge sea level records present discontinuities and the instability in the reference level due to strong vertical land movements prevents the use of tide gauge data for sea level change studies.

6.1 Area of study

The Indonesian seas act as a connection between the western Pacific Ocean and the eastern Indian Ocean and as a key feature of the global ocean circulation: Their straits and passages form the Indonesian throughflow, which advects north and south Pacific waters into the Indian Ocean.

The main inflow of the Indonesian throughflow is the Makassar Strait. Flowing south, the mass of water splits with one branch entering the Indian Ocean through the Lombok Strait and another flowing eastward through the Flores Sea and then through the Banda Sea, which has several narrow pathways that lead the water into the Indian Ocean. [142]

While on interannual timescales, El Niño (La Niña) triggers lower (higher) sea level anomalies, the whole area is mainly characterised by the annual cycle of the monsoon winds, which blow from the west from November to March (northwest monsoon), and from the east from May to September (southeast monsoon). In the Java Sea, characterised by shallow depths, the alternation of the monsoon winds

pushes low-salinity water from the South China Sea up to the southern Makassar Strait during the wet months and high-salinity water from the Pacific during the dry season [143].

At the eastern Indian Ocean boundary the monsoon winds reversing every six months induce Ekman transport that generates opposite geostrophic flows in the Northern and Southern Hemispheres [144]. Here, the circulation is characterised by the Java Coastal Current following the bathymetry slope; The direction of its flow changes depending on the monsoon wind direction [145].

A better understanding of the variability of the sea level in this area could lead to an understanding of the variability of the Indonesian throughflow, for example [146] argued that the surface layer seasonal mass divergence in the Banda Sea influences its timing and transport.

Figure 6.1 shows the geographical limit of SAR CS-2 data and defines two domains that were selected North and South of Java Island (NJ and SJ from now on). The domains were chosen in order to contain both data from Envisat and from CS-2 SAR and to be representative of two very different conditions of a coastal ocean environment: in NJ, a strong coastal current with pronounced bathymetry slope characterised by high waves and variability; in SJ, a shallow area with calmer sea state. In the crossover statistics (section 6.5) all the CS-2 measurements included in the latitude box of the map are taken into account.

In section 6.6, time series of averaged cross-calibrated sea level measurements are generated for Java Sea, Flores Sea, Banda Sea, Bali Sea and Ceram Sea, defined according to the *Limits of Ocean and Seas* published by the International Hydrographic Organization in 1953 (see figure 6.2), despite the limited geographical availability of SAR CS-2 data. Figure 6.2 shows the extension of each of the Indonesian seas.

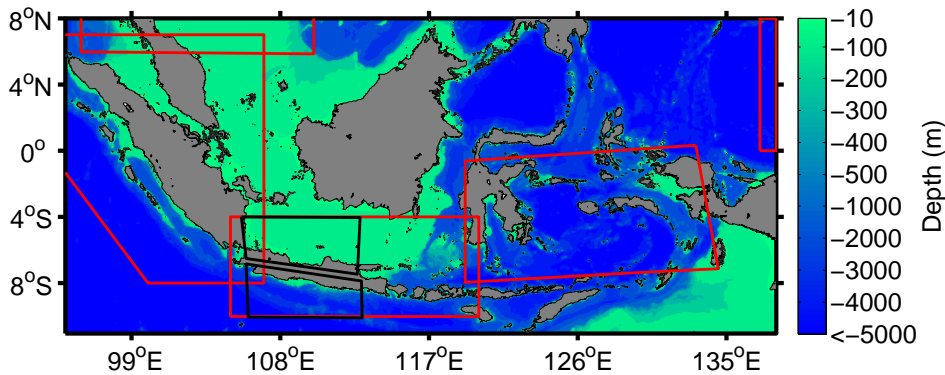


Figure 6.1: The domains selected North and South of Java Island (NJ and SJ) delimited by the black lines and the SAR boxes of CS-2 (delimited by the red lines).

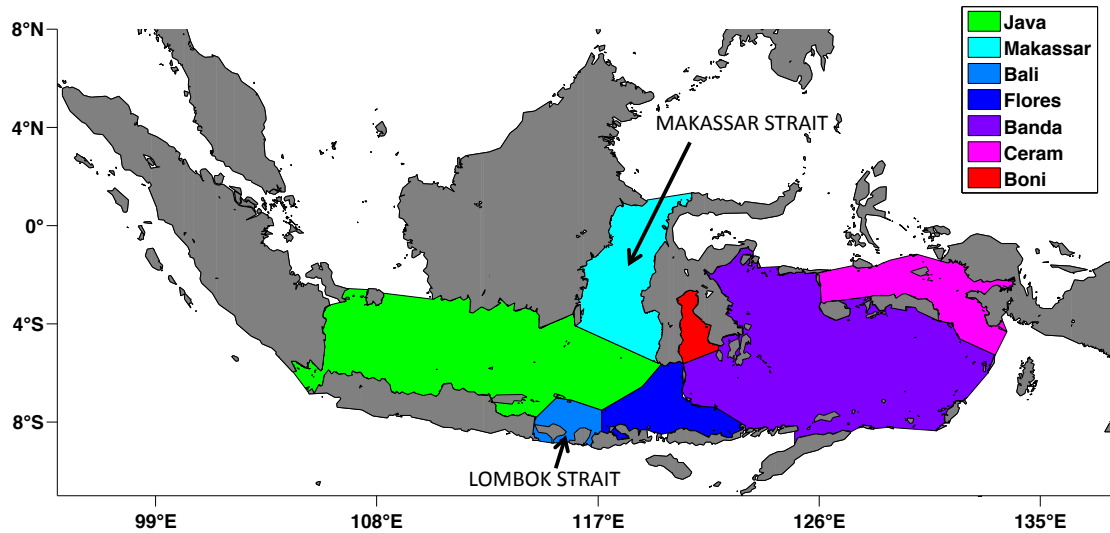


Figure 6.2: The basins of interest within the Indonesian seas, defined according to the *Limits of Ocean and Seas* published by the International Hydrographic Organization in 1953.

6.2 Dataset

This chapter uses altimetry data from Envisat reprocessed with ALES and from CS-2 SAR mode distributed with the SARvatore service. Envisat data cover orbital Phase B (from autumn 2002 to the 22nd October 2010) and orbital Phase C (from 23rd October 2010 to 8th April 2012, after which the contact with the satellite was lost). Envisat Phase C is characterised by a slightly shorter repeat cycle (30 days) compared to Phase B, since the satellite orbit was lowered by 17.4 km. Due to

the orbit change, ground tracks were also shifted in Phase C, which prevented the extension of the time series along the same repeated tracks until the launch of AltiKa satellite in 2013. In this chapter, when a distinction is needed, the two phases of Envisat will called Env B (Envisat Phase B) and Env C (Envisat Phase C).

CS-2 was launched in July 2010, which guarantees slightly less than 4 months of overlap with Envisat, and it is currently successfully continuing with the data acquisition. While over the vast majority of the ocean surface CS-2 operates in low resolution mode (LRM), i.e. as a standard pulse-limited altimeter that does not exploit the pulse-to-pulse coherency as described in section 2.6, "SAR" boxes are planned during the orbit, in particular when the satellite overpasses coastal oceans. Figure 6.1 shows that only a part of the Indonesian seas are covered by the SAR box. Nevertheless, given the focus of this chapter and the content of the SARvatore product, only CS-2 SAR data are used in the analysis. SARvatore data were downloaded using the GPOD ESA service (*gpod.eo.esa.int*) in May 2015. SARvatore processes the CS-2 raw data using the SAMOSA2 functional form described in [147]; the settings suggested for coastal areas are all applied, i.e. Hamming weighting window on the burst data, zero-padding and extended radar receiving window size (for details, see [148], freely available from GPOD).

CS-2 has a ground track spacing of 7.5 km at the Equator and a 369-day repeat cycle [149]: Although the latter prevents a repeat-track analysis of the data, the high density of the tracks makes it very representative for regional averages, as in the case of Envisat if compared to missions with more frequent repeat passes and larger ground track spacing.

In order to harmonise the set of geophysical corrections, MSS from DTU10, tidal amplitudes from DTU13 and ECMWF-force DAC are applied to both missions (for a justification of the choices, see section 5.2). Concerning the Wet Tropospheric correction, the issues arising in the coastal areas have already been discussed. While the GPD correction is available for Env B, the same could not be obtained for Env C. Moreover, the GPD correction includes valid measurements from the microwave radiometer on board Envisat, while CS-2 does not have such an instrument. For these reasons, this study applies the ECMWF-based wet tropospheric correction for the entire dataset.

Finally, two potential sources of error must be mentioned for future developments. Firstly, concerning CS-2 sea level estimation, it must be reminded that only a tentative SSB correction is applied in this study, equal to 4% of the SWH (see section 2.4.3), given that at the time of writing a SSB model for SAR altimetry has not been validated yet. An improvement of this tentative value is then proposed in

section 6.5. Secondly, concerning tidal amplitudes, the contribution of internal tides, which are very large in the Indonesian seas and can generate a surface signature up to few cm, is not yet fully understood and not yet implemented in the tidal models [150, 151].

6.3 Methods

The analysis is performed with the following strategy:

1. Data screening and detection;
2. Statistics of crossover differences and intercalibration;
3. Regional derivation of seasonal signals and trends in the sea level.

6.3.1 Methods for data screening and outliers detection

ALES Envisat 18-Hz sea level measurements were screened using the methodology already described in 5.3.1. CS-2 data in SARvatore are distributed in averages at 20-Hz and 1-Hz. In this study, 1-Hz points were recomputed starting from 20-Hz estimations using the same methodology as in Envisat, with the following exceptions:

- The Coastal Proximity Parameter (CPP) parameter is not available for CS-2 and, given the different footprint and antenna characteristics of CS-2, the Envisat CPP parameter cannot be used;
- The fitting error in SARvatore is computed on the whole waveform and provided in waveform power units. A maximum value of 4 power units in the fitting error is here adopted, considering that analysis on open ocean data have shown that $\sim 99\%$ of the waveforms are fitted within this threshold (S. Dinardo, personal communication).

Since the aim here is to cross-calibrate two missions rather than comparing products referring to the same mission as in the previous chapter, the following additional screening was added on the 1-Hz points in order to exclude noisy retrievals, non-representative averages and errors in the corrections. A 1-Hz point was excluded from the analysis if:

- The number of valid measurements within the 1-Hz block is less than 5.

-
- The standard deviation of the valid measurements within the 1-Hz block is larger than 0.20 m; this criterion is justified by the fact that such a high slope in sea level would be not plausible in an area of \sim 7 km.
 - The sum of the geophysical corrections, excluding ocean tides, is smaller than 1 m; such values would be unrealistic given that, for example, the dry tropospheric correction has a global mean of 2.31 m with only 2 cm std [36].

6.3.2 Methods for the statistics of crossover differences

To verify the precision and the agreement between Envisat and CS-2, a comparison of the sea level at the crossover points was performed. This is a standard practice in altimetry and has been used in several publications as a key indicator of the data quality for altimetric missions (see [152] for a comprehensive list of references). In the common practice, in order to reduce the impact of oceanic variability, crossovers are taken into consideration if the time lag between the two passes is shorter than 10 days. Moreover, coastal areas, shallow seas and in general high variability areas are avoided, while in this research they are explicitly taken into consideration. Crossovers are here defined as all the available 1-Hz points of two crossing tracks that are closer than 5 km. It is important to mention that both Envisat and CS-2 measurements have been referred to the same ellipsoid and the absolute bias found for Envisat (see [95]) was taken into account. Four crossover cases were considered:

- Envisat Phase B ascending versus Envisat Phase B descending passes (case EnvB-EnvB)
- Envisat Phase C ascending versus Envisat Phase C descending passes (case EnvC-EnvC)
- Envisat Phase C ascending and descending versus CS-2 ascending and descending passes (case EnvC-CS2)
- CS-2 ascending versus CS-2 descending passes (case CS2-CS2)

6.3.3 Methods for regional derivation of seasonal signals and trends in the sea level

Data were grouped depending on the corresponding basin and averaged every month. Given the stress on the evaluation of coastal performances, data in NJ and SJ were divided according to the distance from the coastline (0-50 km, 50-100 km, 100-150

km). Estimations of annual and semiannual cycles were performed using the PW FGLS estimation described in section 5.3.2. Subsequently, the seasonal cycle was removed from the time series and the trends were estimated using the same method.

6.4 Results and discussion

6.4.1 Comparison of performances between Envisat and CS-2

In this section, the test areas of NJ and SJ are used for comparison of the performances of Envisat and CS-2, with particular focus on the coastal zone. Plots A.1 and A.2 of figure 6.3 show the number of passes for each month: the amount of measurements available in the sub-basins in one month is similar in the time series of both missions. It is noted that in two months of 2005 several Envisat data are lacking and this holds also for the initial 3 months after the launch of CS-2. In order to keep the consistency, for each mission statistics are shown only for months where more than 10 passes are available.

In order to check the consistency of the dataset, plots B.1 and B.2 of figure 6.3 show the standard deviation of the retrieved SLA within 50 km of the coast. A single averaged sea level value for each pass of Envisat or CS-2 is assigned and each point on the plot corresponds to the monthly mean of the std considering all available passes. The plots show therefore the variability of the sea level within a month in the domain of interest. The coastal region of SJ has a higher variability than the corresponding area in NJ, as expected. In both regions, the average variability is consistent in all the three missions: in South Java there is an average monthly std of 9.2 cm for Env B, 10.0 cm for Env C and 9.5 cm for CS-2; in North Java the values are 7.0 cm for Env B, 7.8 cm for Env C and 7.2 for CS-2. In the 15 months when enough measurements from Env C and CS-2 were both available: the root mean square difference between the monthly std from Env C and CS-2 is 2.4 cm in NJ and 1.8 cm in SJ. The retrieved variability is therefore very comparable, despite the fact that the two satellites were sampling different areas in different days. In SJ, all the months with a std exceeding 0.15 cm are located in May or in November, i.e. during the expected onset of the monsoons.

Plots C.1 and C.2 of figure 6.3 reproduce the std statistics, but consider only the geophysical corrections, i.e. the sum of wet (WTC) and dry tropospheric correction (DTC), DAC correction, ionospheric correction and sea state bias. Envisat and CS-2 data use the same dataset for WTC, DTC and DAC. The std of the corrections

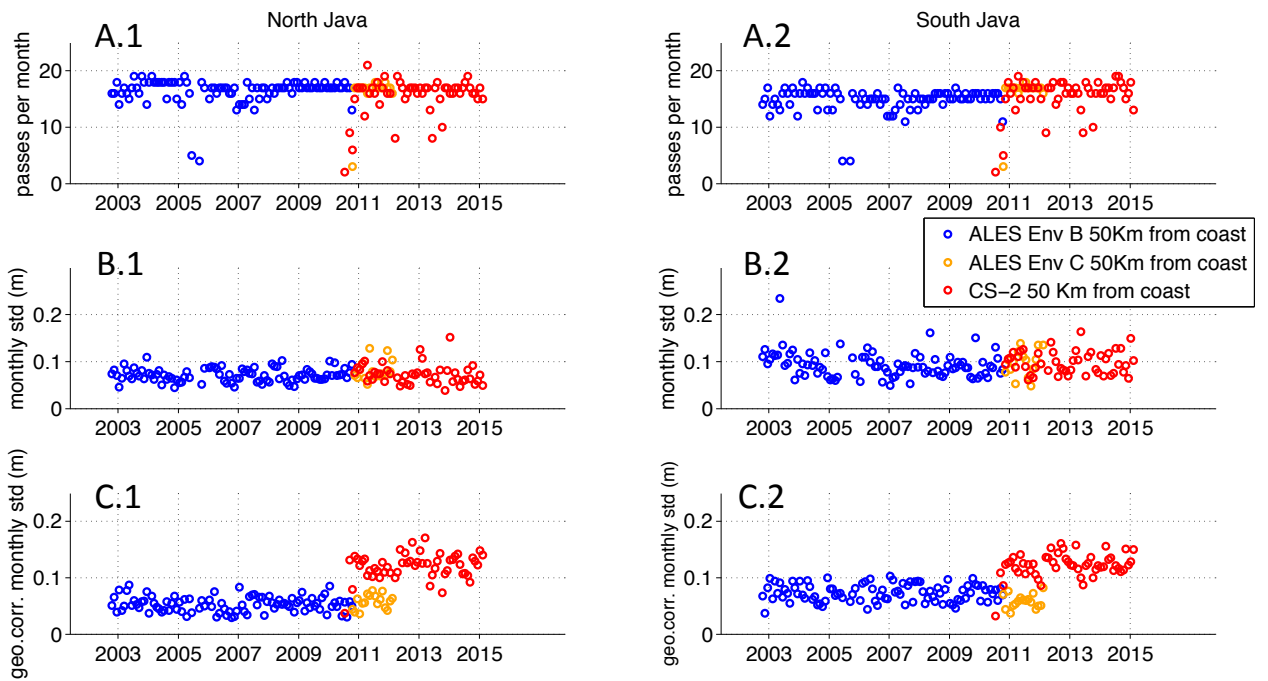


Figure 6.3: Statistics for the time series of Env B ALES (blue), Env C ALES (orange) and Cryosat-2 SARvatore (red) in North Java (left) and South Java (right). A.1 and A.2: number of satellite passes available in each month. B.1 and B.2: Standard Deviation of the monthly SLA values. C.1 and C.2: Standard Deviation of the monthly geophysical correction applied to the SLA estimations. Only data from months when at least 10 passes were shown.

applied to CS-2 is almost double than that of Envisat. This difference is explicable considering the orbit of the satellites. Envisat follows a sun-synchronous orbit, therefore the satellite flies over the same area at the same time. This is not true for CS-2, as it is shown in figure 6.4: depending on ascending and descending orbits, Envisat overpasses the area in two clearly defined sections of the day, while the measurements of CS-2 span the whole 24-hours time. In fact, all the geophysical effects have their own diurnal cycle linked to daily variation in the atmospheric pressure [153], ionospheric electron content [154] and wet and dry component in the troposphere [155].

Figure 6.5 shows the monthly average of the 20 (18)-Hz SLA measurement noise computed at each 1-Hz location for CS-2 (Envisat) within 50 km of the coast. In both NJ and SJ, the average retrieved SWH is plotted in green for each mission. The noise level of Envisat is consistent between Phase B and Phase C and ALES confirms its good coastal performances, already validated in section 4.2.6. This helps to highlight the differences between the sea state of the two areas and the relationship

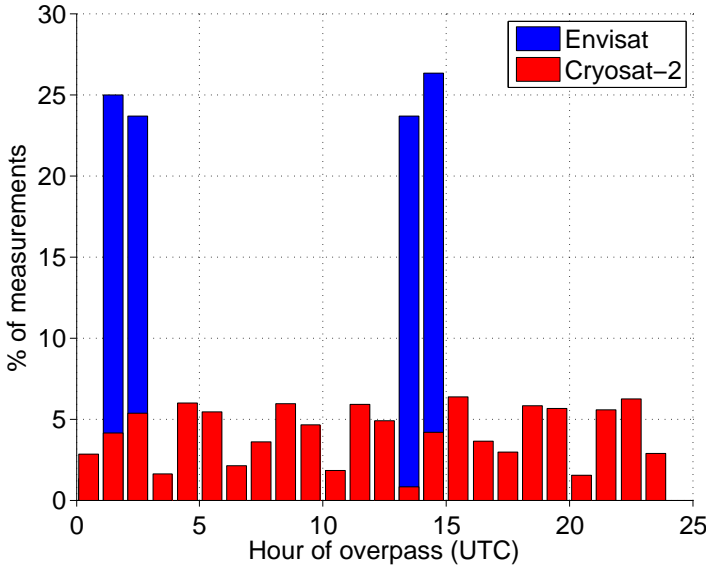


Figure 6.4: Overpass time in the Java region for Envisat (blue) and Cryosat-2 (red).

between measurement noise and sea state, since higher SWH corresponds to noisier data in all the datasets. Although the validation of CS-2 SWH estimation is not an objective of this research, it is remarkable that in both the areas CS-2 SWH is on average in very good agreement with the SWH measured by Env C. A significant improvement in precision, if compared to Envisat, is remarkable in CS-2, whose noise is up to 1cm lower than Env C in the same months for both NJ and SJ. This result confirms that SAR altimetry is intrinsically more precise than the standard processing.

Figure 6.6 shows the consistency of noise and variability w.r.t. the distance of the coast in NJ and SJ, by averaging in time the previous statistics. In both NJ and SJ, the variability maintains the same levels, which are almost indistinguishable among the different missions. This is particularly important considering that both Env C and CS-2 sample areas that were not sampled by previous missions, whose data are used to build the MSS models.

Compared to figure 6.5, the noise in the bottom plot is here scaled at 1Hz level, i.e. the high-rate noise is divided by the root mean square of the number of measurements in each 1 Hz block. The plot confirms the robustness of the improvement in precision brought by CS-2, quantifiable as roughly 0.3 cm at 1 Hz level w.r.t. Envisat regardless of the sea state.

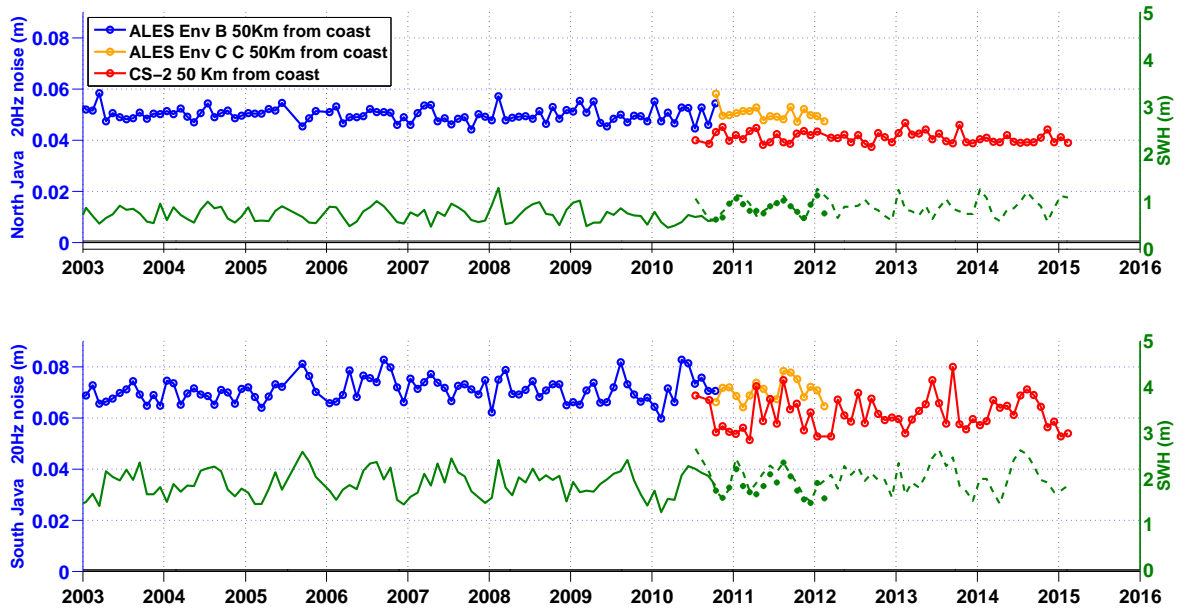


Figure 6.5: Average 20Hz noise of the SLA values in SJ and NJ within 50 km of the coast for Env B ALES (blue), Env C ALES (orange) and CS-2 SARvatore (red). Also shown is the average estimated Significant Wave Height for each mission (green curves).

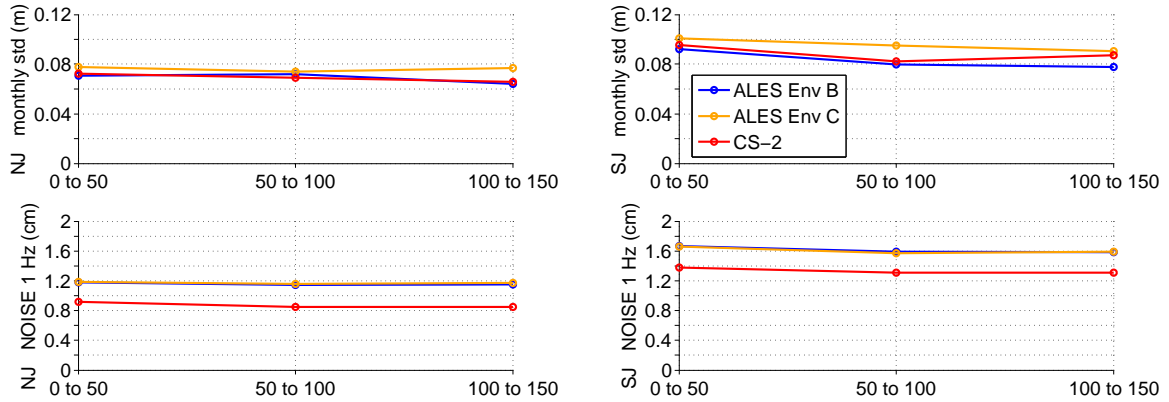


Figure 6.6: Variability of the parameters of interest in North Java (left column) and South Java (right column) depending on the distance from the coastline (in km on the x axis) for Env B ALES (blue), Env C ALES (orange) and CS-2 SARvatore (red). Top: Standard Deviation of the monthly SLA values. Bottom: Average 1Hz noise of the SLA values.

6.5 Statistics of crossover differences and cross-calibration

In this section, the analysis of the crossovers in the test areas of NJ and SJ is discussed, in order to cross-calibrate the two missions. Figure 6.7 shows the characteristics of the crossovers for each case in terms of time lag and distance from the coast. While crossovers in case EnvC-CS2 span the whole 10 days of permitted time difference, all the other cases, due to the orbit characteristics, are bounded to specific time lags. In terms of distance from the coastline, valid case CS2-CS2 crossovers were found only further than 70 km from the coast, while all the other cases were representative of both coastal and open ocean conditions.

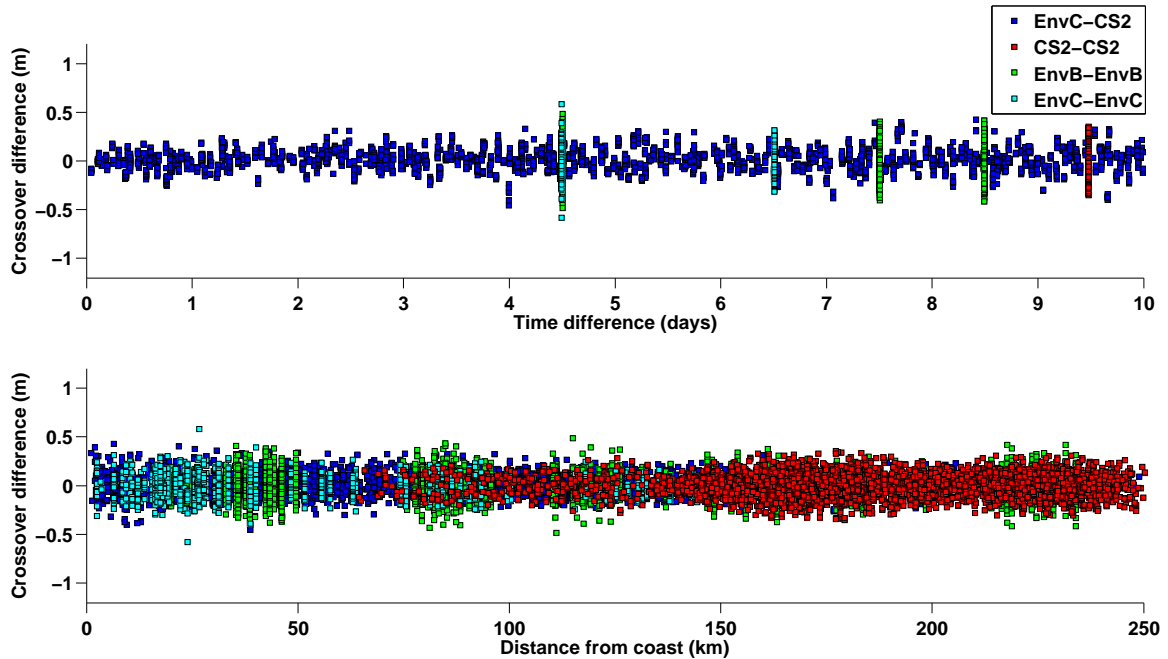


Figure 6.7: Upper plot: distribution of crossover differences depending on time difference between the satellite passes. Lower plot: distribution of crossover differences depending on distance from the coastline.

In order to have a fair comparison, the histogram on the left of figure 6.8 compares the four cases considering only points located further than 70 km of the coast. Performances among the same missions are extremely similar and unbiased, since the mean of the crossover differences is zero. Concerning single-mission crossovers, the small differences in the histogram of case CS2-CS2 compared to EnvB-EnvB and EnvC-EnvC could correspond to the time differences of the crossovers seen in figure 6.7. Concerning the case EnvC-CS2, the crossover differences have a mean

of 1.4 cm, which goes down to -0.6 cm when considering the crossover differences without applying any SSB correction in neither of the two missions (black histogram in the plot on the right). This is very significant, given that [152] showed a global mean crossover difference of 5.8 between Env B and CS-2 LRM mode considering only a month and only deep water and low variability region, while here shallow water data and regions with high variability are being tested.

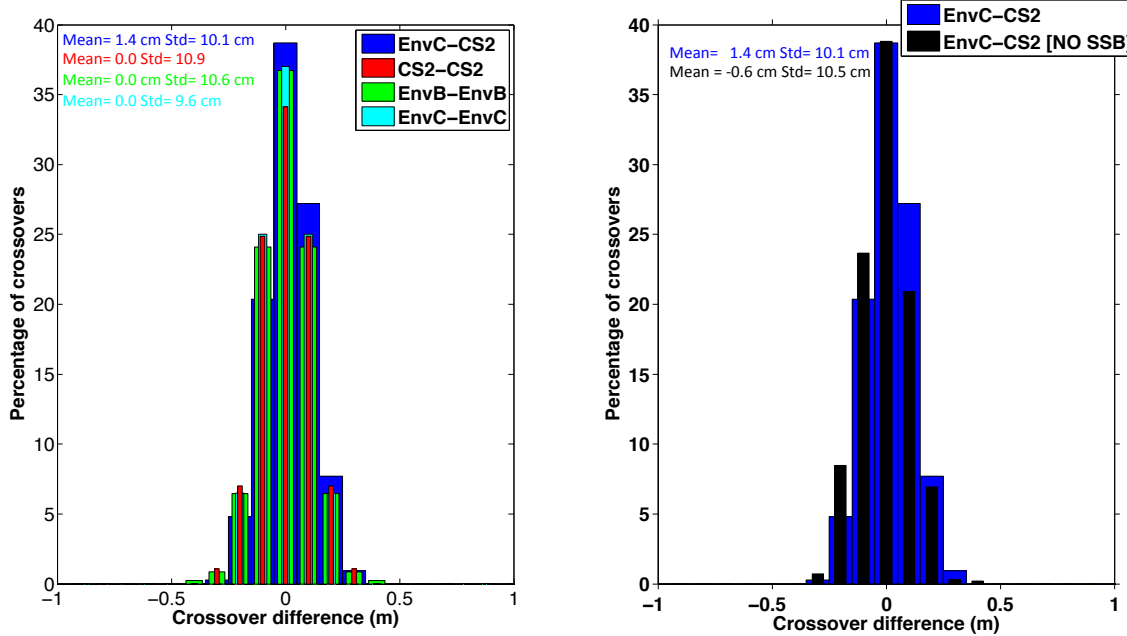


Figure 6.8: Left: Histogram of crossover differences considering only points farther than 70 km of the coast. Right: Same histogram with focus on the crossovers between Env C and CS-2 with and without applying a SSB correction in each dataset.

A clearer evaluation that considers both coastal and open ocean conditions is found in figure 6.9. The plots focus on the coastal zone, showing the statistics between 0 and 25 km and between 25 and 50 km from the coast, considering as "open ocean" anything beyond 50 km. Statistics for the case CS2-CS2 in the coastal zone are not present due to the lack of coastal crossovers in the area of study for CS-2. The upper plot shows the mean of the crossover differences. The cases of the same mission are centred on zero within half a cm. The EnvC-CS2 comparison shows a bias slightly higher than 1 cm in the area closest to the coast and in the open ocean. The standard deviation of the crossover differences is about 10 cm for all cases in the open ocean; it increases in the coastal zone, but is always less than 15 cm (figure 6.9, middle plot).

The scatter plot of the SLA differences at the EnvC-CS2 crossovers w.r.t. the

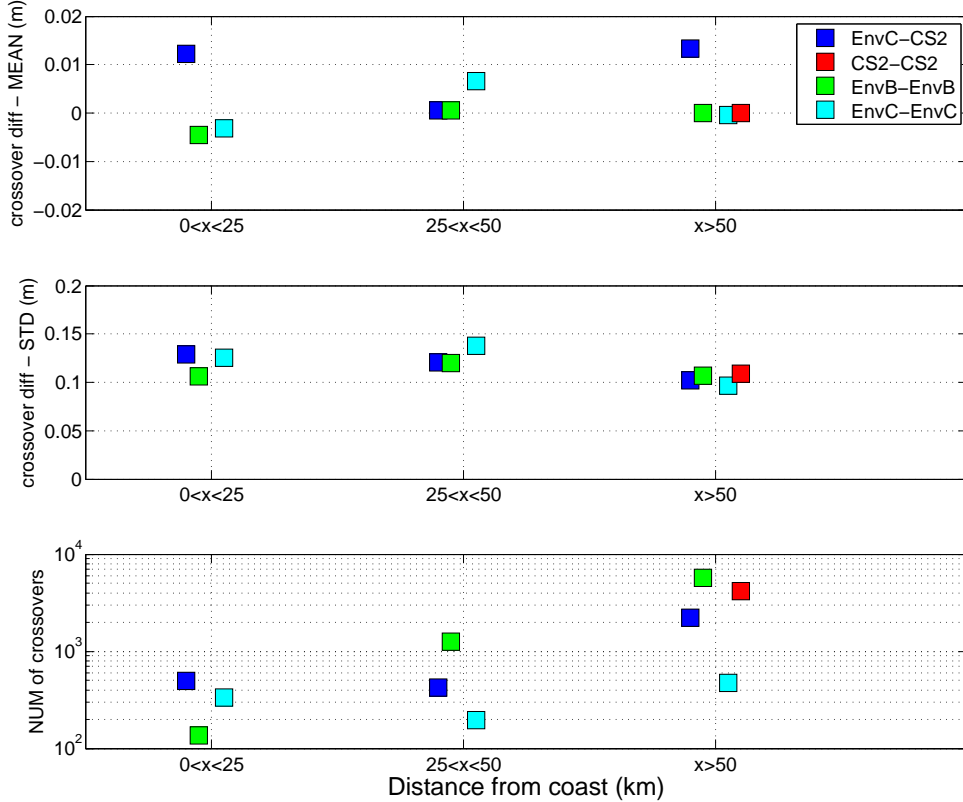


Figure 6.9: Mean (top), standard deviation (middle) and number (bottom) of crossover differences grouped according to the distance from the coast. The squares are horizontally displaced to facilitate the reading.

SWH estimated by CS-2 is shown in figure 6.10 for NJ and SJ. The difference of wave conditions encountered in the two test regions is immediately visible: NJ never encounters a SWH higher than 2 m in the observed period, while in SJ most of the retrieved SWH is above 1.5 m. The linear fitting gives the following relationship:

$$(EnvC-CS2) = -0.002 + 0.010 \times SWH \quad (6.1)$$

This relationship is therefore used to cross-calibrate the CS-2 SSHA estimations and a "bias-corrected" version of the dataset is produced. The SWH coefficient in equation 6.1 is equivalent to adding another 1% to the SSB correction. It is therefore concluded that an overall regionally unbiased cross-calibration between Envisat and CS-2 is achievable by approximating the SSB correction for SAR altimetry at 5% of the SWH, rather than the 4% originally recommended (see section 2.4.3).

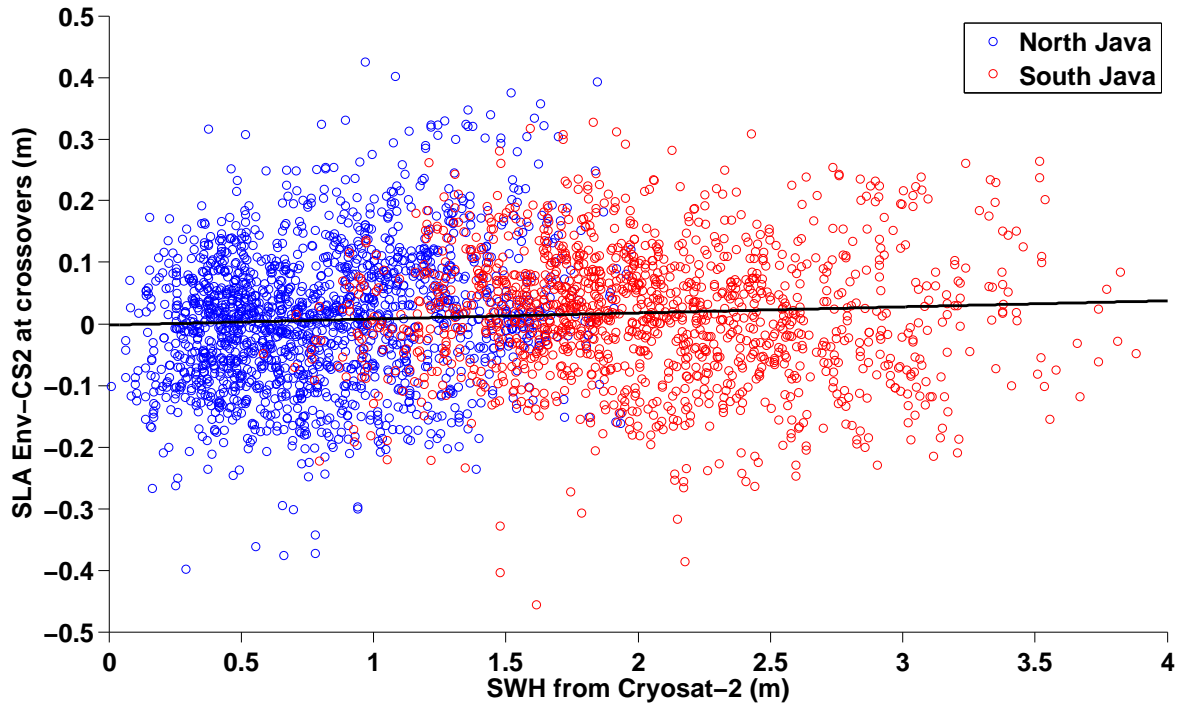


Figure 6.10: SLA difference at crossover points versus SWH estimation from Cryosat-2; the linear fitting shows a slope of 1 cm in 1 m and an intercept at -2 mm.

In order to test the validity of the cross-calibration across the test area, figure 6.11 shows the same statistics as 6.9 only for EnvC-CS2 case, separating the results according to the distance from the coast and the sub-basin of reference. Despite the overall unbiased statistics shown previously, small regional mean biases are still present, although they do not exceed 2 cm. The top plot shows the mean differences at crossover also without applying any SSB correction for any of the two datasets: also in this case, local biases are of the same order of magnitude.

Considering these results, it is important to stress that the SSB correction for Envisat is based on a parametric model that takes into account also the wind information derived from the backscatter coefficient estimated by the altimetric measurements [36] and that the SSB field is not yet being recomputed using ALES estimations. At the same time, the coefficients of a parametric SSB model can be mission-dependent and even the validity of this model has yet to be demonstrated for the SAR-altimetry observing principle. Future studies should address this issue, but for the present research it is found that the derived SSB correction equal to 5% of the SWH is an acceptable value and does not add further biases in the cross-calibration of the two missions that are being considered.

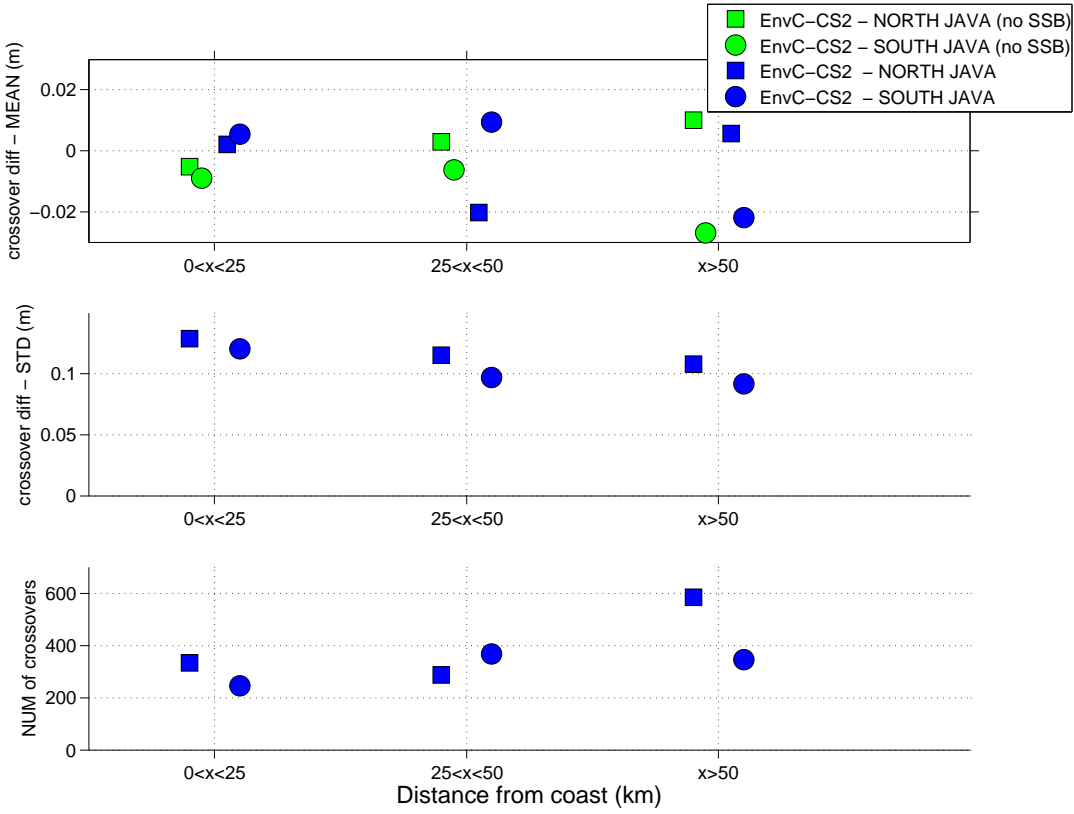


Figure 6.11: Mean (top), standard deviation (middle) and number (bottom) of crossover differences grouped according to the distance from the coast and sub-basin of reference. The squares are horizontally displaced to facilitate the reading.

6.6 Inter-calibrated time series

This section analyses the inter-calibrated multi-mission sea level time series. In the first part, the sea level variability of NJ and SJ is analysed in terms of distance from the coast and different datasets. Subsequently, the results for the different Indonesian Seas are presented and discussed.

6.6.1 North Java and South Java

The variability of the sea level is here analysed for NJ and SJ in terms of trend, annual cycle amplitude and semiannual cycle amplitude. Statistics are computed for different distance from the coast (0-50 km, 50-100 and 100-150 km) and time series are formed using data from:

- Envisat Phase B (Env B)
- Envisat Phase B and Envisat Phase C (Env B+C)

- Envisat Phase B and CS-2 up to the end of Envisat Phase C availability (Env B+CS2lim)
- Envisat Phase B and CS-2 (Env B+CS2)

Figure 6.12 shows the time series built by taking the monthly averages of Env B+C (in blue) and of Env B+CS2 (in red), considering the coastal points from 0 to 50 km from the coast. The limits are kept the same for both areas, in order to highlight the differences of the variability: SJ is characterised by a marked annual cycle, while the seasonal variations in NJ are much more limited. The linear fitting (solid straight lines) is also computed for the multi mission Env B+CS2lim time series (in green) considering the CS2 data only up to the end of Envisat Phase C availability.

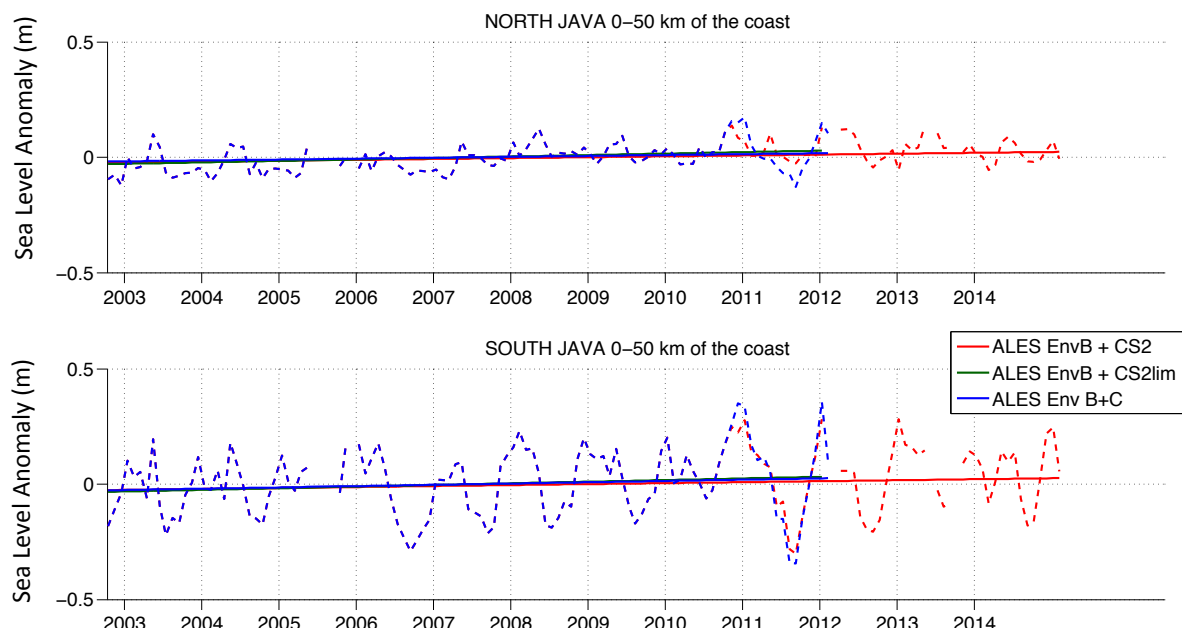


Figure 6.12: Time series in NJ and SJ at 0–50 km from the coast using Envisat B+C data (blue dotted line) or Envisat B+CS2 data (red dotted line). The straight lines show the linear fitting using Envisat B+C data (blue), Envisat B+CS2 data (red) and Envisat B+CS2 data only until the end of Envisat Phase C ("ALES Env B + CS2 lim", in green)

Firstly, the agreement of the time series from Env Phase C and CS-2 in the same months can be evaluated by computing the RMS of the difference, as reported in table 6.1 considering different distances from the coast. The RMS value is consistent, since numbers are similar in both the areas of study, although in NJ within 50 km of the coast the RMS is half a cm higher. There is an increase of 1.2 to 1.5

	0-50 km	50-100 km	100-150 km
North Java (m)	0.063	0.048	0.048
South Java (m)	0.058	0.046	0.047

Table 6.1: RMS of the difference between the monthly time series of Env C and CS-2 in NJ and SJ at different distances from the coast.

cm in the coastal zone compared to the open ocean. This could be due to the accuracy of the corrections applied to both datasets, in particular the tide and MSS models, considering that the ground tracks of the two missions span different areas at different times. This could be felt particularly in NJ, due to the influence of internal tides that the models do not take into account.

Trends and amplitudes of annual and semiannual cycles are reported in tables 6.2 and 6.3 for NJ and SJ; the estimates and uncertainties are computed for all the time series listed previously.

The estimates of annual and semiannual cycle amplitude for Env B+C and Env B+CS2lim agree within 5 mm in both basins. Trends are difficult to estimate due to large uncertainties. Positive trends are found for both Env B+C and Env B+CS2lim in NJ, but the trend of Env B+C in SJ is not statistically significant. Considering the trends of all combinations, the estimates are higher in the Env B years and decline with the extension of the time series up to 2015 (case Env B+CS2). In particular, the trends in the Env B years are in agreement with the trends ranging from 4 to 8 mm/year found in the region of study in the period 1993-2011[141]. The lower best estimates of the trends of Env+CS2 (which is not statistically significant in SJ) will be investigated in the next section.

The estimates confirm that SJ sees a strong annual cycle (\sim 12-14 cm), but also a pronounced semiannual cycle with an amplitude of roughly a third to a half of the annual amplitude. The semiannual and annual signals in NJ have similar amplitude of about 2 to 2.5 cm. The annual pattern in the region is related to the reversal of the wind patterns associated with the Asian-Australian monsoon, as explained in section 6.1. The semiannual signal is related to the passage of coastally trapped Kelvin waves; they are the propagation of equatorial Kelvin waves generated in the Indian Ocean at the transition of the two monsoons, which propagate eastward hitting the coast of Sumatra [156, 157].

Using the longest time series (Env B+CS2), the variability is then computed at different distances from the coast for NJ and SJ in tables 6.4 and 6.5. It is consistently observed that both trends and seasonal variability increase when the data are closer to the coast in SJ, while this is only true for the trend in NJ. Trend

	Env B	Env B+C	Env B+CS2lim	Env B+CS2
Trend (mm/y)	6.3±4.4	3.9±3.4	6.3±3.6	3.8±2.6
Ann Ampl (mm)	25.0±12.9	19.6±15.4	21.3±12.6	25.3±10.9
Semi Ampl (mm)	25.0±10.4	28.7±10.2	25.7±9.9	27.6±8.4

Table 6.2: Trend, annual amplitude and semiannual amplitude of the different sea level time series, using data within 50 km of the coast of NJ.

	Env B	Env B+C	Env B+CS2lim	Env B+CS2
Trend (mm/y)	8.9±7.6	5.6±7.0	7.0±6.6	4.2±4.3
Ann Ampl (mm)	120.9±30.7	138.1±30.9	134.3±29.0	130.5±24.5
Semi Ampl (mm)	38.7±23.3	49.3±21.8	43.9±21.0	57.8±17.7

Table 6.3: Trend, annual amplitude and semiannual amplitude of the different sea level time series, using data within 50 km of the coast of SJ.

estimates in NJ are all positive and significant, while the ones in SJ have a higher uncertainty and therefore cannot be considered statistically significant. The increase of the amplitude of the seasonal variability in the coastal areas characterised by a strong coastal current has already been debated in the previous chapter and here the case of the South Java Current in SJ is similar to the one of the Norwegian current in the Skagerrak Sea.

The possibility of higher sea level rise in the coastal zone compared to the open ocean has long been debated and addressed as one of the key reasons of interest for the development of coastal altimetry. Recent unpublished work has been presented in other areas using altimetry with corrections optimised for the coastal zone, but using neither coastal retracking of standard altimetry nor SAR-altimetry measurements [158]: results showed marked increase in the variability of the sea level, but also trends 20-30% higher than offshore, although conclusions were preliminary and possibly attributed to residual inaccuracies of coastal altimetry.

These results in NJ and SJ show higher coastal trends as best estimates, even using improved processing techniques, but considering the temporal and spatial limit it is not possible to deduce valid conclusions. As reported in section 6.2, all the time series here have different length depending on the mission taken in consideration. This is reflected in the uncertainty of the trend and periodicities, which are smaller for the longest time series (Env B+CS2). Nevertheless, also the longest time series is still affected by uncertainties that undermine any statistically significant conclusion for coastal trends in SJ. In particular, Table 6.5 shows that considering the years

	0-50 km	50-100 km	100-150 km
Trend (mm/y)	3.8 ± 2.6	3.4 ± 1.8	3.2 ± 1.6
Ann Ampl (mm)	25.3 ± 10.9	18.8 ± 10.9	26.2 ± 10.9
Semi Ampl (mm)	27.6 ± 8.4	33.6 ± 8.1	33.3 ± 8.2

Table 6.4: Trend, annual amplitude and semiannual amplitude of the multimission EnvB+CS2 time series, using data at different distances from the coast of NJ.

	0-50 km	50-100 km	100-150 km
Trend (mm/y)	4.2 ± 4.3	3.4 ± 4.3	3.3 ± 4.1
Ann Ampl (mm)	130.5 ± 24.5	112.3 ± 22.0	96.8 ± 18.7
Semi Ampl (mm)	57.8 ± 17.7	49.2 ± 14.4	36.8 ± 11.7

Table 6.5: Trend, annual amplitude and semiannual amplitude of the multimission EnvB+CS2 time series, using data at different distances from the coast of SJ.

2002-2014, no statistically significant trend is detectable in SJ. An effort is also needed in terms of extending the time series to previous missions in order to decrease the level of uncertainty.

6.6.2 Indonesian Seas

The trend and variability analysis is here extended to the Indonesian seas as defined in figure 6.2, considering the longest time series generated in this study, i.e. Env B+CS2. Among the seas listed in the figure, only the ones where at least 10 satellite passes of Envisat and CS-2 are available for each month are chosen: Java, Flores, Banda and Ceram Seas. The results reported in table 6.6 and figure 6.13 are representative of the whole basins, regardless of the distance from the coast, because the SAR-altimetry coverage is not complete and uniform in most of the basins and because they are delimited mainly by bathymetric slopes rather than by coastlines.

Figure 6.13 indicates the switch between Envisat and CS-2 data with a vertical straight line. To add robustness to the analysis, the Env B+CS2 time series for each basin are compared with the sea level time series available from <http://sealevel.colorado.edu/content/regional-sea-level-time-series> (here called CU time series), generated considering the Jason ground tracks over the entire Indonesian Throughflow region and part of a dataset that is constantly monitored against a network of tide gauges and used to produce global mean sea level estimates [159]. This dataset, even if coming from a different processing and averaged on a wider area, is still useful for comparison because it includes data from differ-

	Java	Flores	Banda	Ceram
Trend (mm/y)	2.9±2.0	2.9±2.4	1.7±4.2	3.3±3.2
Ann Ampl (mm)	52.3±10.6	59.1±10.1	79.1±10.1	78.4±11.8
Semi Ampl (mm)	26.7±6.8	4.2±6.3	2.8±5.9	6.3±7.4

Table 6.6: Trend, annual amplitude and semiannual amplitude of the multimission EnvB+CS2 time series for Java, Flores, Banda and Ceram seas.

ent missions (TOPEX, Jason-1 and Jason-2) that sample repeated tracks without a discontinuity in time, such as the Envisat-CS-2 "switch".

The annual signal amplitude estimated in the entire Java Sea is larger than in the test area NJ. Indeed, the full area of Java Sea is much wider and in particular includes a deeper area that borders the Makassar Strait. Moreover, the semiannual signal is stronger in Java than in the other internal seas. It has already been observed that the Kelvin waves that characterise the monsoon transitions can travel through the Lombok Strait and slow down the southward water transport in the Makassar Strait [160]. From the semiannual amplitudes in the different seas, it is inferred that the waves propagate to the shallower Java Sea reaching the Makassar Strait, but do not influence the variability of the deeper Flores and Banda basins. This is in agreement with previous studies that concluded that the Kelvin waves exiting the Lombok Strait travel along the 100-m isobath [161].

The comparison with the CU time series and the good agreement between the curves proves that the decay in sea level seen in the CS-2 years is not an artefact. Previously, [141] using altimetry in the region to compute trends in the timescale 1993-2011 observed how on interannual time scales the local sea level variability is strictly and homogeneously linked to the El Niño Southern Oscillation (ENSO) variability. The reason of the slowing trend is to be found in the strong La Niña event of 2010, which caused strong negative anomalies even in the global sea level [162], being the coldest ENSO event in the past eight decades [163].

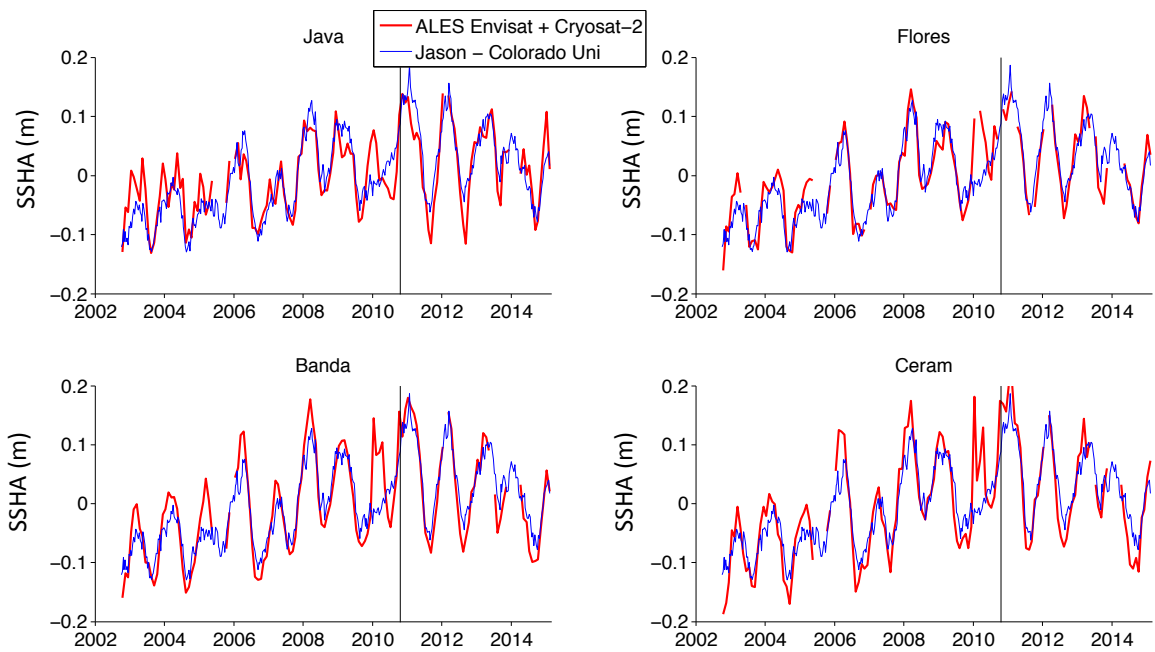


Figure 6.13: Multimission EnvB+CS2 time series (in red) and Jason-Colorado Uni time series (blue) for Java Sea (top left), Flores Sea (top right), Banda Sea (bottom left) and Ceram (bottom right). The black straight line indicates the start of CS2 dataset.

Chapter 7

Overall discussion and impact of the research

7.1 Improvements in Range and SWH Estimation

The main technical development of this research has been the design of a retracker capable of improving the sea level estimation in the coastal zone. The use of ALES as a single retracking strategy for any standard altimetry mission without the need of a preliminary classification, if combined with an effective outlier detection, can generate a homogenous global multi-mission dataset that enhances the coastal capabilities of satellite altimetry. Indeed, a similar approach could be tuned for the SAR-altimetry echoes, by adapting the Montecarlo simulations described in this research to the functional forms currently under study for the new delay-doppler echoes.

The validity of the proposed solution has been verified for Jason-1, Jason-2 and Envisat in two very different oceanographic areas. On one hand, the results prove that there is no significant degradation between standard open ocean high-rate range estimation and ALES values in terms of noise and accuracy. On the other hand, ALES significantly increases the amount of altimetric information retrievable in the coastal zone, in areas that were disregarded even by dedicated coastal post-processed datasets, such as in the Gulf of Trieste. Biases of the order of 1 cm with SGDR values demonstrate the comparability between the two datasets. Further analysis on bias and noise is needed and will be performed once an extensive global retracked dataset is available.

The benefits of ALES coastal reprocessing are not limited to a 10 km wide strip along the coast, where the satellite footprint assimilates land return together with ocean signal, but extend to tens of kilometres from the coast. Bright targets that

cause deviations from the standard open ocean model in the waveforms are seen much further in the open sea, because land interference is not the only source of perturbation in the trailing edge. Bright targets are mainly connected to sea state and areas of low sea roughness that can be caused by land sheltering from winds or coastal upwelling fronts that produce film slicks on the surface. Although ~ 3 km from the coast can be considered a reasonable threshold, it is not possible to give a global limit of validity for ALES range estimations. The CPP parameter is a good indication of the influence of the coastal elevation on the waveform, but its usefulness is limited to a measurement of land interference in the footprint. Nevertheless the criteria adopted in the previous chapters for the identification of the outliers are potentially valid in any other coastal area. Overall, although ALES seeks a solution to improve the use of satellite altimetry in the coastal zone, it would be incorrect to set a clear boundary between coast and open ocean data. Introducing a discontinuity between open ocean and coast could wrongly justify the use of different retracking solutions, while ALES circumvents the problem by using the same strategy for both the domains. Tailored sea level products are meaningful when dealing with specialised corrections such as regional tide models, but this research suggests that the scientific community should look for the adoption of a retracking strategy that is applicable to oceanic waveforms as a whole without undermining the precision of the estimation.

The SWH retrieval of the ALES retracker has been validated in the German Bight, but the use of multiple buoys and multiple tracks in the case of Envisat and the high number of cycles and the clear results in the case of Jason make a case for a more general extension of the conclusions. Nevertheless, the robustness of the findings is limited to low SWH (<2.5 m); this however includes conditions considered particularly challenging in altimetry, due to poor leading edge sampling.

It has been shown that ALES is able to increase the amount of SWH retrievals towards the coast, while remaining highly reliable in the open sea as well. An improvement is seen for one to three 1 Hz points towards the coast for each of the tracks (for both Envisat and Jason missions), meaning about 7 to 22 km in terms of spatial extension. Moreover, the 1 Hz estimations have a constantly lower standard deviation compared to the original SGDR product, which implies that the exclusion of part of the trailing edge by subwaveform selection provides more precise estimations of the slope of the leading edge.

A widespread underestimation of low SWH is found in the latest version of Envisat SGDR product and the cause is the value used to approximate the width of the PTR function in the Brown functional form for the SGDR retracking. This

analysis suggests that the previous value of $\sigma_p = 0.53r_t$ (with r_t being the time resolution) is a better one. This study has highlighted how the adoption of a single value for the width of the PTR is not a sufficient approximation of the reality in the Brown model. Moreover, the possibility of improving the SWH estimation in the coastal zone calls for a new ALES-based SSB correction.

The ALES retracking strategy makes use of the two additional DFT gates provided in the Envisat SGDR: it is found that the increased leading edge sampling reduces the standard deviation w.r.t. the ground truth from in-situ data and increases the amount of correct estimations. This is an indication that the oversampling of the leading edge, even if it does not add any information on the frequency content of the returned signal, improves the estimation thanks to a higher redundancy, which is beneficial for the convergence of the numerical fitting. The finding supports the strategy currently adopted for the generation of CS-2 echoes, that are zero-padded before the FFT operation, and consequently oversampled.

7.2 Improvements in coastal sea level analysis

For the first time, a dedicated coastal altimetry retracker has produced data that have been used to perform a sub-basin scale sea level analysis. In an area where validation is possible thanks to the high concentration of coastal in-situ data, such as the North Sea-Baltic Sea intersection, the improvements are clear. Only ALES-based amplitude estimates of the annual cycle are in agreement with TGs within 1 cm in every sub-basin with the exception of the Norwegian coast of the Skagerrak Sea: Here the difference between ALES and TG estimates of the annual cycle allows the recognition of a slope in the amplitude that follows the bathymetry of the Skagerrak Sea and is not well represented in the SL_cci estimates. The estimates of the annual cycle of the sea level from Level 4 gridded SL_cci product are in agreement with the TGs in most locations, but overestimate the amplitude in the West Arkona basin, probably due to residual tidal variability, and lack coastal details in the Norwegian Skagerrak, probably due to the gridding and the exclusion of coastal sea level retrievals. In these coastal environments the use of ALES reprocessed along-track data leads to the recognition of patterns that can be lost in the mapped dataset.

An integrated analysis considering external information helps to identify the sources of the variability in the annual cycle of the sea level. It was already known that the sea level time series in North Sea-Baltic Sea transition zone are correlated with the large-scale wind pattern. The new ALES dataset, in combination with an up-to-date archive of temperature/salinity profiles, has revealed that the differences

within and among the sub-basins are driven by different phases of the steric cycle (West Arkona and Norwegian Trench) and by coastal circulation patterns (Norwegian Coastal Current).

The methodology applied in this study is potentially applicable to other coastal areas, providing that the aliased annual component of tidal constituents such as K1 for Envisat is of a lower order of magnitude than the annual cycle of the sea level. The sub-basin division can increase the frequency of the measurements in a time series and limit aliasing problems in the annual cycle estimates due to the Envisat repeat orbit. Nevertheless, this procedure requires an a-priori knowledge of the dynamics of the area and an along-track analysis can help to detect differences within each sub-basin, particularly in areas with bathymetry slopes.

It has been shown how even in well-known areas the higher comparability between tide gauges and satellite measurements can reveal narrow details such as the annual signature of the Norwegian Coastal Current, but coastal altimetry will be even more important when used in areas that lack any in-situ monitoring. The example of the Indonesian seas is illuminating: it demonstrated the possibility to cross-calibrate the new SAR altimetry data with ALES-reprocessed coastal time series, which guarantees several years of observations that can help lowering the level of uncertainty on the computation of trends. The availability of global SAR altimetry with Sentinel-3 will allow the geographical expansion of this calibration exercise, but the validity of the consequent sea level analysis will still depend on the homogeneity and accuracy of the geophysical corrections applied to the dataset. Since there is still no agreement on the sea state bias model to be used for SAR altimetry, an empirical sea state bias correction (5% of the estimated SWH) was found. In Indonesia, it has been proven that the different orbit characteristics of Envisat and CS-2 do not have an influence on the variability of the averaged sea level, therefore the MSS model seems to be accurate enough even in areas that were previously unsampled. SAR altimetry from CS-2 is roughly 0.3 cm more precise than Envisat altimetry at 1 Hz, even without any coastal-dedicate retracking of SAR waveforms. Overall, this comparison shows that the ocean product designed for CS-2 SAR can be applied successfully in combination with previous missions, despite the peculiar orbit characteristics of the satellite, designed mainly for the cryosphere.

The study has shown examples of the transition from deeper to shallower areas in terms of amplitude of the annual cycle, which is consistently higher in the presence of coastal currents. The availability of a global ALES dataset will allow the analysis on a wider scale in relation to the main coastal circulation patterns. It is harder and premature to derive any conclusion by comparing coastal and open-ocean sea

level trends, since more years of observations are needed. The impact of the study in this case will definitely be enhanced by the extension of the ALES methodology to previous missions.

Chapter 8

Conclusions

This work has been devoted to the elaboration of a new dataset of satellite altimetry that could also be used in the coastal zone, bringing validated information to the oceanographic community. The approach was to start from the observation of the radar echoes and design an algorithm to properly fit them (in a process called retracking) in order to estimate the geophysical parameters of interest. Secondly, the estimations from the new algorithm have been validated and their application has shown the benefits that this new method can bring to coastal oceanography and, in particular, sea level studies. This thesis has given an answer to the three aims formulated in chapter 1:

1. Developing the optimal retracking solution.

It has been established that an optimal retracker needs to apply a homogenous strategy both in the open ocean and in the coastal zone, in order to minimise biases within the processing of the same satellite tracks. The analysis of coastal waveforms and the previous literature have shown on one hand that most of the wrong estimations are due to the presence of areas of high reflectance in the satellite footprint, due to land and calm water interaction, on the other hand that these phenomena do not repeat either in time nor in position at every satellite pass. The optimal solution was found by means of Montecarlo simulations that evaluated the difference in the accuracy of a full-waveform retracker against different widths of the subwaveforms. The solution presented, i.e. the Adaptive Leading Edge Subwaveform (ALES) retracker, is based on a linear relationship between a first estimation of the sea state and the width of the subwaveform that is used for the estimation of the parameters. Since it still adopts the classic Brown functional form, commonly used in the open ocean, ALES guarantees great comparability with the standard product and,

in particular, has very similar performances in terms of noise. At the same time, it increases the amount of valid sea level estimations in the coastal zone and it can be applied to any standard altimetry mission.

2. Defining and applying the criteria to demonstrate the performances of a re-tracking system.

The validation against in-situ data in challenging coastal environments and the verification against the statistics of the standard product have been considered the most effective criteria to evaluate the performances of ALES data. Sea level and significant wave height estimations were validated against tide gauges and buoys not only by means of traditional statistics such as correlation and root mean square error, but also using innovative techniques, such as the PCHC, that considers the number of repeated satellite passes that can be used to guarantee a high level of correlation with the in-situ dataset. Moreover, the statistics were evaluated considering the whole transition from open ocean to the coast, rather than only focusing on the closest points between the satellite pass and the in-situ sensor. Finally, the validation was performed on three different missions. These criteria were applied in areas with different oceanographic characteristics and the results showed that the best improvement compared to standard data is obtained in sheltered areas (such as the Gulf of Trieste), but also in the open ocean the ALES estimations do not degrade the performances.

For sea level studies, improvements were tested by applying the same analysis to two of the state-of-the-art sea level products available: the ESA Sea Level Climate Change Initiative and the RADS archive. The North Sea - Baltic Sea transition zone has been used as a test area, due to the complex coastline and the high availability of the in-situ data. Subsequently, an analysis of sea level periodicities and trends has been performed in the Indonesian Seas to test the comparability with the new SAR altimetry data and to cross-calibrate them to the Envisat data in order to expand the sea level time series.

3. Evaluating the improvements that the use of a coastal dedicated altimetry strategy brings to regional sea level analysis.

A complete coastal-dedicated altimetry strategy was developed for the output of the ALES retracker. This included careful outlier detection and the use of geophysical corrections that were found to be particularly suitable for the coastal environment. A sub-basin analysis of the annual sea level from the Envisat mission in the North Sea-Baltic Sea transition zone has shown that

the ALES dataset not only improved the quality and the quantity of sea level data in the area when compared to the other datasets, but was also able to capture details that were missed by the other datasets, i.e. the higher annual cycle of the narrow Norwegian Coastal Current. Overall, the ALES dataset was the most reliable and accurate, as confirmed by the smallest RMSD of the annual estimated sinusoid w.r.t. a tide-gauge based analysis. Although the improvements were evaluated considering the best estimates, the error bars were often too large and consequently the difference in the estimations between the different datasets were not statistically significant. The sub-basin average has proven an effective technique to densify the number of measurements in time and exploiting in the best way the high density of tracks of the Envisat mission compared to the Jason series, that are traditionally employed for studies at a larger scale.

The cross-calibration of ALES-reprocessed Envisat with the CS-2 SAR data has shown how SAR altimetry produces an improvement in coastal altimetry, even without a dedicated coastal retracker, thanks to a better precision of the measurements and a smaller footprint. The regional-based cross calibration managed to produce an overall unbiased multi-mission dataset, despite the use of an empirically-derived sea state bias correction for CS-2 data. This coastal dedicated strategy, using the sub-basin approach, has been able to detect the area of influence of the semiannual Kelvin waves generated in the Indian Ocean at the monsoon transitions, the coastal sea level rise in the years 2002-2010 and the effect of the strong La Niña event of 2010, which triggered lower sea level anomalies.

8.1 Future prospect

The possibility to have a multi-mission retracker opens a wide range of further studies in terms of applications and extensions. Validation with TG data also demonstrates that ALES can be used for coastal sea level and surge monitoring studies, due to its increased comparability with the coastal in-situ sensors.

The effort of the research on retracking should of course be assisted by new coastal-dedicated corrections, in particular wet troposphere correction and sea state bias, and, where possible, regional high resolution tidal models, in order to isolate the sea level anomaly from the TWLE. In this regard, a new computation of sea state bias using ALES estimations would be beneficial.

A stronger collaboration has to be found with the modellers, in order to evaluate

the impact of the ALES estimations if assimilated in ocean circulation and wave models, but also as an efficient validation tool.

ALES should also be applied to previous missions (TOPEX,ERS) to extend the time-series, but more work is needed to understand the benefit of a subwaveform approach for other functional forms in the SAR altimetry context. A particularly interesting tool is the possibility to retrack very high-frequency waveforms with an ALES-like retracker (see Appendix); this may guarantee a better fitting of the received echo, particularly in narrow backscattering surfaces such as leads in sea-ice or rivers.

This study demonstrates that coastal altimetry is now in a mature stage in which it can be used for coastal sea level variability studies at sub-regional spatial scales and seasonal time scales. Sea level studies should use reprocessed coastal altimetry with confidence also in areas where in-situ data are absent. With careful work on sub-basin selections and on tuning of the geophysical corrections, it would be possible to produce a dedicated coastal altimetry product in specific areas of the global coastal ocean where there is much room for improvements (due to lack of in-situ data, high risk of sea level rise or storm surges, rugged coastlines).

A further improvement to the ALES coastal altimetry product could be the addition of an uncertainty to every estimate. In the case of sea surface height, this would involve not only considering the errors in the corrections, but also associating an uncertainty value to the range estimate. Nevertheless, this is not directly derived from the estimation, since the optimisation method provides only the fitting error as a parameter to evaluate the fitting. The fitting error on the leading edge is a useful parameter that can help the expert user in avoiding the inclusion of outliers in the analysis, but to evaluate the uncertainty, one could use the precision of the 20-Hz measurement, which in altimetry is traditionally given by the standard deviation of the high rate estimates within a 1-Hz segment.

The successes in the validation and application of ALES, shown in this thesis, and the promising collaboration with other scientists that are interested in using this dataset (for example in the context of the ESA e-Surge and e-Surge Venice projects) has urged the importance of global availability of the dataset. At the time of writing, the global reprocessing of Jason-2 and Envisat data within 50 km of the coast, using the same algorithm described in this work, is completed and the data are being uploaded in the Physical Oceanography Distributed Active Archive Center (PODAAC) system (ftp://podaac.jpl.nasa.gov/allData/coastal_alt/L2/ALES/). It is hoped that the choice of sharing such a dataset with the science community will help the advances of coastal oceanography and the improvement of ALES itself.

Appendices

Appendix A

ALES for AltiKa

The aims of this short appendix are to show the applicability of the ALES strategy to the Altika waveforms and to propose an experimental study concerning the retracking of waveforms at higher frequency, i.e. formed by averaging a smaller amount of individual echoes (IEs). The analysis is shown here since it is beyond the objectives of this thesis and due to its preliminary state. Nevertheless, it is believed that it could constitute one of the most promising advanced applications of the ALES strategy in future studies.

A.1 ALES for AltiKa: retracking 40-Hz waveforms

As mentioned in section 2.6, Altika hosts the first satellite altimeter in Ka-band. Nevertheless, it can be considered a standard altimetry mission, being still pulse-limited. The ALES principle is therefore applicable. In order to identify the linear relationship between ALES first-pass SWH estimation and the width of the requested subwaveform for fitting an Altika 40-Hz echo, a Montecarlo simulation was run as described in section 3.2.2, using the specifics of Altika to generate the synthetic waveforms. The following linear relationship was found:

$$\text{Maximum gate} = \text{Ceiling}(\text{ Tracking point} + 2.90 + 3.37 \times \text{SWH}) \quad (\text{A.1})$$

where the nomenclature is the same as used for equations 3.3 and 3.4. Since Altika follows the same ground-tracks as Envisat (including the numbering), 14 cycles were reprocessed in the Gulf of Trieste along track 416. By doing so, it was possible to apply the same validation process as described in chapter 4 (including the

generation of a TWLE product and the outlier detection) comparing the estimations against the values of the TG in Trieste (see figure 4.1 for the location of the TG and the ground track). The statistics of the validation (see 4.1 for a methodological description) are shown in figure A.1. It can be seen that both the SGDR product and the ALES retracker behave similarly, but ALES scores generally better particularly in the last 2.5 km from the coast. Until this threshold, both the datasets have significantly stable performances. This confirms that AltiKa is less affected by bright targets compared to previous missions, thanks to the reduced footprint size and the higher radar frequency, which brings to a fast decay of the trailing edge of the waveforms.

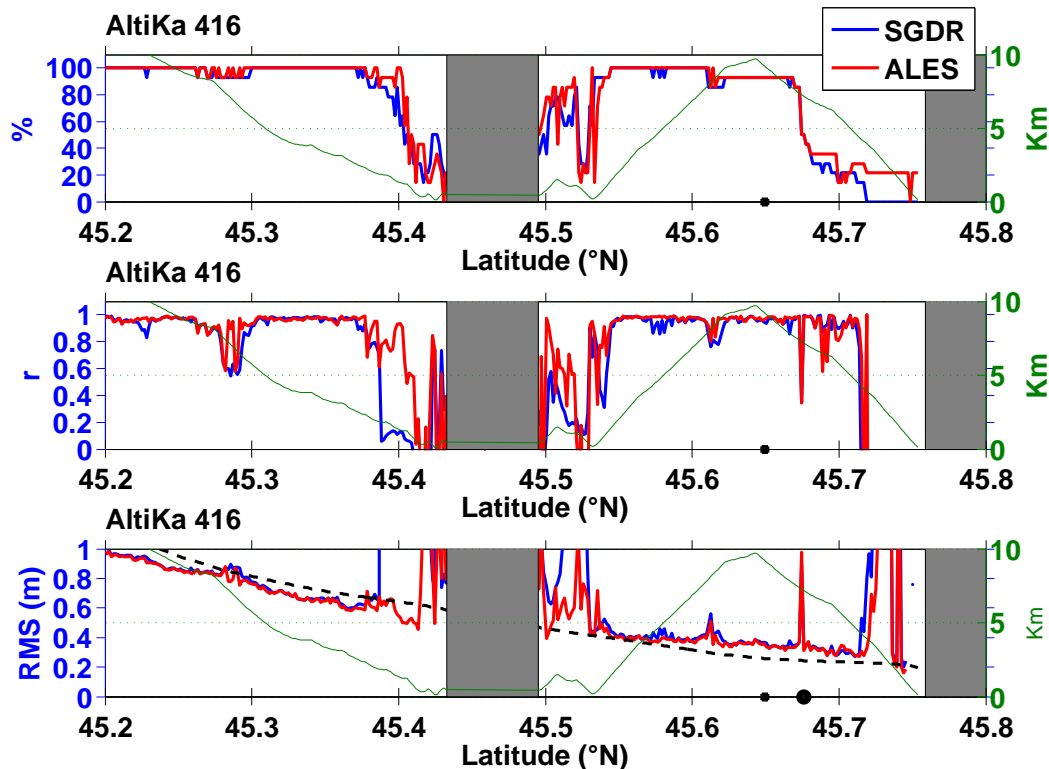


Figure A.1: AltiKa pass 416 (14 cycles): PCHC (top), correlation coefficient (centre) and absolute RMS difference (bottom) between Trieste TG and ALES (SGDR) data in red (blue). On the x-axis the along-track latitude of the nominal tracks are shown. Black dots on the x-axis highlight the latitude of the TG (big dot) and of the closest point along track (small dot). Land is shaded in grey. The distance from the closest coastline is specified by a green line which refers to the y-axis on the right. A black dashed line marks the difference between the along track mean sea surface (DTU10) and the mean sea surface DTU10 at the TG.

A.2 ALES for AltiKa: retracking at higher frequencies

AltiKa emits 3700 chirps per second, with the returns normally being summed in groups of 96 to produce average echoes (AEs) at the rate of 40 Hz. Normally, 40-Hz echoes are downlinked and distributed in the SGDR format. However, at specific times a 1-second burst of IEs is recorded and transmitted in its entirety. Typically this burst will consist of 42 segments of 96 IEs, thus corresponding to 1.09s of data (7.1 km distance along track). These 1-second bursts form the so-called high density (HD) product. In the HD product each burst is registered as a series of 128 in-phase and quadrature (I and Q) components. A Fourier transform, plus power summation over returns, is required to produce the familiar delayed time echo shown in waveforms.

In the context of the KaNUTE project, the Centre National d'Etudes Spatiales (CNES) granted access to a limited number of HD products: here the analysis concentrates on 17 bursts available over marine surfaces, for which the mean shape is well described by the Brown model. This allows the opportunity to investigate the potential for different processing strategies. In particular, the motivation comes from the empirical observation of IEs: although their trailing edge does not show a clear decaying power and the standard Brown shape is highly compromised by the noise, the leading edge is still clearly recognisable. This can be seen in the example of figure A.2, where waveforms formed by averaging a growing number of IEs up to the whole burst are compared. The high noise in the trailing edge justifies the attempt of using a subwaveform strategy to extract the geophysical information from these echoes. The open-ocean bursts, away from extraneous reflections from land surfaces, are therefore used to investigate how the retracking performances degrade as the retracker fits noisier AEs calculated from fewer IEs.

Although a single IE does have a definite leading edge, the expected variability at any particular bin precludes it from giving the desired accuracy. The more IEs that are summed to produce an average, the better defined will be its leading edge and the less noisy its trailing edge. The question is how many IEs should be summed to form a waveform that can be satisfactorily retracked by ALES. To give a quantitative answer, for each 0.025s (40 Hz) segment we can thus construct a number of AEs that depends on how many IEs are summed for each of them. This processing is applied to the 17 burst files over the ocean, with the putative AEs calculated from 8, 12, 16, 24 and 32 IEs. The ALES retracker is applied to the 40-Hz waveforms and to the different AEs to evaluate the retracking performances.

No. of IEs	Range std (cm)	Range bias (cm)	<i>SWH</i> std (m)	<i>SWH</i> bias (m)
8	16.2	8.55	0.95	0.46
12	14.4	7.90	0.71	0.40
16	11.8	6.75	0.57	0.36
24	10.8	5.81	0.48	0.28
32	8.7	4.34	0.45	0.24

Table A.1: Median error over all 17 bursts as a function of number of IEs summed. The std indicates the consistency of estimates within a burst; the bias is the median absolute deviation with respect to tracking of 40-Hz waveforms.

Two statistics are taken into account for each 0.025s segment for both the estimation of range and of SWH:

1. the median absolute bias of the estimations from each AE with respect to the estimation from the 40-Hz waveform, and
2. the standard deviation of the AEs estimations within the whole burst.

The first is a measure of uncertainty related to a "best case" estimation, in this case the retracking performed on the average of all the 96 IEs of each segment. The second is a measure of noise in the estimation. Results are shown in figure A.2 b-e for range and SWH estimation. Median results from each file are colour-coded depending on the number of IE powers averaged before retracking. The statistics are plotted against the median SWH of each burst, estimated from ALES applied to the 40-Hz waveforms. As expected, this demonstrates that more precise results are achieved at lower values of SWH. Precision also improves with increasing number of IEs averaged, but it is surprising to see how consistent the estimations can be even at very high frequencies. For example, the ALES retracking of sums of 32 IEs (120 Hz) adds a lower noise level to epoch estimation than was estimated for 10 Hz AEs for Jason-1 [60]. Generally, the findings are consistent with the familiar picture from past altimetry missions of greater range uncertainty in 1-Hz records at larger SWH.

Table A.1 provides the median values for bias and precision across these diverse 17 cases. These show that the error in the tracking of a generated average echo typically scales as $M^{-0.5}$, where M is the no. of IEs summed together. This is as expected from statistical considerations for the mean calculated from M independent samples. Similarly, the precision, here estimated as the std of the estimates, scales as $M^{-0.5}$.

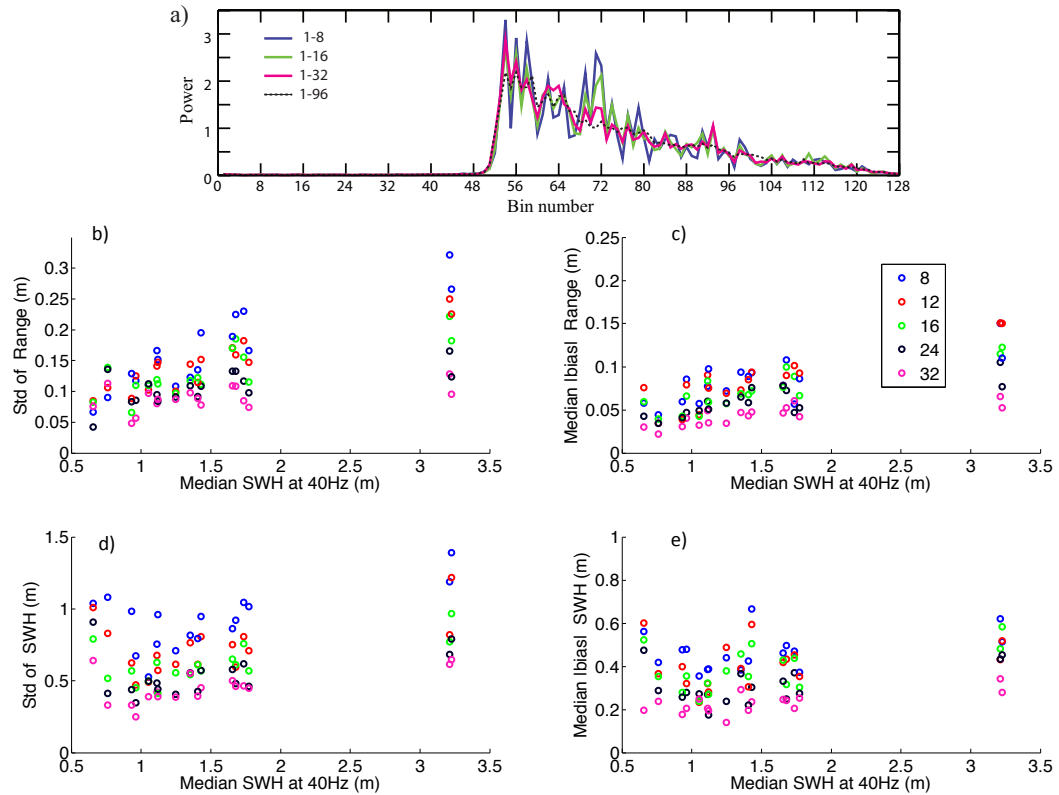


Figure A.2: Tracking error engendered by summing fewer IEs. a) Illustration that the leading edge is well-defined by just a few summed pulses, whereas the trailing edge is much less clear. b), d) Consistency of retracking of range and SWH respectively within a 1s burst. c), e) Mean absolute bias (relative to processing of 40-Hz waveforms) for range and *SWH*.

A.3 Discussion

An application emerging from this analysis is the possibility to retrack waveforms at a frequency > 40 Hz and eliminate the AEs that produce an estimate substantially different from the rest within a 1-second burst. Corrupted high-rate AEs could therefore be identified as outliers and the remaining estimates can then be averaged to produce a more robust result at a lower frequency. This procedure could be useful in coastal areas, inland water bodies and leads in sea-ice to eliminate the IEs that are highly corrupted by "bright targets".

For oceanographic applications, 40-Hz data are sufficient, corresponding to along-track sampling of ~ 174 m, especially given that the instrument footprint corresponds to a disk with a minimum diameter of 2 km. However over more variable terrain where calm water and spurious returns in the footprint can influence the shape of the returned echo, it may be advantageous to use data at a finer resolution, allowing the removal of signals whose waveform shape does not match expectation.

Bibliography

- [1] R. K. Raney, “The delay/doppler radar altimeter,” *IEEE Trans. Geosci. Remote Sensing*, vol. 36, no. 5, pp. 1578–1588, 1998.
- [2] P. Bonnefond, B. Haines, and C. Watson, “In situ absolute calibration and validation: a link from coastal to open-ocean altimetry,” in *Coastal Altimetry* (S. Vignudelli, A. Kostianoy, P. Cipollini, and J. Benveniste, eds.), (Berlin Heidelberg), pp. 259–96, Springer-Verlag, 2011.
- [3] F. Birol, M. Cancet, and C. Estournel, “Aspects of the seasonal variability of the northern current (NW Mediterranean Sea) observed by altimetry,” *J. Marine Syst.*, vol. 81, no. 4, pp. 297–311, 2010.
- [4] C. Desportes, E. Obligis, and L. Eymard, “One-dimensional variational retrieval of the wet tropospheric correction for altimetry in coastal regions,” *IEEE Trans. Geosci. Remote Sensing*, vol. 48, no. 3, pp. 1001–1008, 2010.
- [5] S. Mangiarotti, “Coastal sea level trends from TOPEX-Poseidon satellite altimetry and tide gauge data in the Mediterranean Sea during the 1990s,” *Geophys. J. Int.*, vol. 170, no. 1, pp. 132–144, 2007.
- [6] K. Madsen, J. Høyer, and C. Tscherning, “Near-coastal satellite altimetry: Sea surface height variability in the North Sea–Baltic Sea area,” *Geophys. Res. Lett.*, vol. 34, no. 14, p. L14601, 2007.
- [7] G. D. Quartly, M. A. Srokosz, and A. C. McMillan, “Analyzing altimeter artifacts: Statistical properties of ocean waveforms,” *J. Atmos. Ocean. Tech.*, vol. 18, no. 12, pp. 2074–2091, 2001.
- [8] E. J. Walsh, “Pulse-to-pulse correlation in satellite radar altimeters,” *Radio Sci.*, vol. 17, no. 4, pp. 786–800, 1982.
- [9] D. B. Chelton, J. C. Ries, B. J. Haines, L.-L. Fu, and P. S. Callahan, “Satellite altimetry,” in *Satellite Altimetry And Earth Sciences: A Handbook Of Tech-*

niques And Applications (L.-L. Fu and A. Cazenave, eds.), vol. 69, pp. 1–131, Academic Press, 2001.

- [10] G. S. Brown, “The average impulse response of a rough surface and its applications,” *IEEE Trans. Antennas Propagat.*, vol. 25, no. 1, pp. 67–74, 1977.
- [11] G. S. Hayne, “Radar altimeter mean return waveforms from near-normal-incidence ocean surface scattering,” *IEEE Trans. Antennas Propagat.*, vol. 28, no. 5, pp. 687–692, 1980.
- [12] X. Deng, W. Featherstone, C. Hwang, and P. Berry, “Estimation of contamination of ERS-2 and Poseidon satellite radar altimetry close to the coasts of Australia,” *Mar. Geod.*, vol. 25, no. 4, pp. 249–271, 2002.
- [13] P. Berry, J. Freeman, and R. Smith, *An Enhanced Ocean and Coastal Zone Retracking Technique for Gravity Field Computation*, pp. 213–220. Berlin Heidelberg: Springer-Verlag, 2010.
- [14] O. Andersen, P. Knudsen, and P. Berry, “The DNSC08GRA global marine gravity field from double retracked satellite altimetry,” *J. Geodesy*, vol. 84, no. 3, pp. 191–199, 2010.
- [15] N. Idris and X. Deng, “The retracking technique on multi-peak and quasi-specular waveforms for Jason-1 and Jason-2 missions near the coast,” *Mar. Geod.*, vol. 35, no. sup1, pp. 217–237, 2012.
- [16] C. Gommenginger, P. Thibaut, L. Fenoglio-Marc, G. D. Quartly, X. Deng, J. Gómez-Enri, P. G. Challenor, and Y. Gao, “Retracking altimeter waveforms near the coasts,” in *Coastal Altimetry* (S. Vignudelli, A. Kostianoy, P. Cipollini, and J. Benveniste, eds.), (Berlin Heidelberg), pp. 61–102, Springer-Verlag, 2011.
- [17] J. Tournadre, “Signature of lighthouses, ships, and small islands in altimeter waveforms,” *J. Atmos. Ocean Tech.*, vol. 24, no. 6, pp. 1143–1149, 2007.
- [18] J. Gómez-Enri, S. Vignudelli, G. D. Quartly, C. P. Gommenginger, P. Cipollini, P. G. Challenor, and J. Benveniste, “Modeling ENVISAT RA-2 waveforms in the coastal zone: case study of calm water contamination,” *IEEE Trans. Geosci. Remote Sensing*, vol. 7, no. 3, pp. 474–478, 2010.
- [19] A. Scorzari, J. Gomez-Enri, S. Vignudelli, and F. Soldovieri, “Understanding target-like signals in coastal altimetry: Experimentation of a tomographic imaging technique,” *Geophys. Res. Lett.*, vol. 39, 2012.

-
- [20] G. D. Quartly, “Determination of oceanic rain rate and rain cell structure from altimeter waveform data. Part I: Theory,” *J. Atmos. Ocean Tech.*, vol. 15, no. 6, pp. 1361–1378, 1998.
 - [21] A. Ollivier and M. Guibbaud, “Envisat RA2/MWR reprocessing impact on ocean data.,” tech. rep., ESA CLS.DOS/NT/12.064, 2012.
 - [22] B. Soussi and P. Femenias, “ENVISAT RA-2/MWR Level 2 User Manual,” *ESA User Manual*, ESA, 2006.
 - [23] J. R. Jensen, “Radar altimeter gate tracking: Theory and extension,” *IEEE Trans. Geosci. Remote Sensing*, vol. 37, no. 2, pp. 651–658, 1999.
 - [24] H. Akima, “A new method of interpolation and smooth curve fitting based on local procedures,” *Journal of the ACM (JACM)*, vol. 17, no. 4, pp. 589–602, 1970.
 - [25] X. Deng and W. Featherstone, “A coastal retracking system for satellite radar altimeter waveforms: application to ERS-2 around Australia,” *J. Geophys. Res.-Space*, vol. 111, no. C6, p. C06012, 2006.
 - [26] L. Yang, M. Lin, Q. Liu, and D. Pan, “A coastal altimetry retracking strategy based on waveform classification and sub-waveform extraction,” *Int. J. Remote Sens.*, vol. 33, no. 24, pp. 7806–7819, 2012.
 - [27] C. Hwang, J. Guo, X. Deng, H.-Y. Hsu, and Y. Liu, “Coastal gravity anomalies from retracked Geosat/GM altimetry: Improvement, limitation and the role of airborne gravity data,” *J. Geodesy*, vol. 80, no. 4, pp. 204–216, 2006.
 - [28] L. Bao, Y. Lu, and Y. Wang, “Improved retracking algorithm for oceanic altimeter waveforms,” *Prog. Nat. Sci.*, vol. 19, no. 2, pp. 195–203, 2009.
 - [29] H. Lee, C. Shum, W. Emery, S. Calmant, X. Deng, C.-Y. Kuo, C. Roesler, and Y. Yi, “Validation of Jason-2 altimeter data by waveform retracking over California coastal ocean,” *Mar. Geod.*, vol. 33, no. S1, pp. 304–316, 2010.
 - [30] P. Berry, H. Bracke, and A. Jasper, “Retracking ERS-1 altimeter waveforms over land for topographic height determination: an expert systems approach,” *ESA-SP 414, 3rd ERS Symposium, Florence, Italy, (17-20 March 1997)*, vol. 414, no. 1, pp. 403–408, 1997.

-
- [31] G. D. Quartly, "Hyperbolic retracker: Removing bright target artefacts from altimetric waveform data," in *ESA SP-686, Living Planet Symposium 2010, Bergen, Norway, (28 June - 2 July 2007)*, ESA Publication, SP-686, (Noordwijkerhout, NL), ESA, 2010.
 - [32] A. Halimi, C. Mailhes, J.-Y. Tourneret, P. Thibaut, and F. Boy, "Parameter estimation for peaky altimetric waveforms," *IEEE Trans. Geosci. Remote Sensing*, pp. 1568–1577, 2012.
 - [33] F. Mercier, N. Picot, P. Thibaut, A. Cazenave, F. Seyler, P. Kosuth, and E. Bronner, "CNES/PISTACH project: An innovative approach to get better measurements over inland water bodies from satellite altimetry. Early results.," in *EGU General Assembly Conference Abstracts*, vol. 11, p. 11674, 2009.
 - [34] J. Guo, Y. Gao, C. Hwang, and J. Sun, "A multi-subwaveform parametric retracker of the radar satellite altimetric waveform and recovery of gravity anomalies over coastal oceans," *Sci. China Earth. Sci.*, vol. 53, no. 4, pp. 610–616, 2010.
 - [35] Y. Yang, C. Hwang, H. Hsu, E. Dongchen, and H. Wang, "A subwaveform threshold retracker for ERS-1 altimetry: A case study in the Antarctic Ocean," *Comput. Geosci.*, vol. 41, no. 1, pp. 88–98, 2011.
 - [36] O. Andersen and R. Scharroo, *Range and Geophysical Corrections in Coastal Regions and Implications for Mean Sea Surface Determination*, pp. 103–146. Berlin Heidelberg: Springer-Verlag, 2011.
 - [37] D. Volkov, G. Larnicol, and J. Dorandeu, "Improving the quality of satellite altimetry data over continental shelves," *J. Geophys. Res.-Space*, vol. 112, no. C6, p. C06020, 2007.
 - [38] M. Le Hénaff, L. Roblou, and J. Bouffard, "Characterizing the Navidad Current interannual variability using coastal altimetry," *Ocean. Dynam.*, vol. 61, no. 4, pp. 425–437, 2011.
 - [39] S. Vignudelli, P. Cipollini, L. Roblou, F. Lyard, G. Gasparini, G. Manzella, and M. Astraldi, "Improved satellite altimetry in coastal systems: Case study of the Corsica Channel (Mediterranean Sea)," *Geophys. Res. Lett.*, vol. 32, no. 7, p. L07608, 2005.
 - [40] G. D. Egbert and S. Y. Erofeeva, "Efficient inverse modeling of barotropic ocean tides," *J. Atmos. Oceanic Technol.*, vol. 19, no. 2, pp. 183–204, 2002.

-
- [41] D. Stammer, R. D. Ray, O. B. Andersen, B. K. Arbic, W. Bosch, L. Carrere, Y. Cheng, B. D. Dushaw, G. D. Egbert, S. Y. Erofeeva, H. S. Fok, M. Green, S. Griffiths, B. Killer, M. A. King, F. G. Lemoine, S. B. Luthcke, F. Lyard, M. Mller, L. Padman, J. Richman, J. Shriver, C. K. Shum, and E. Taguchi, “Accuracy assessment of global barotropic ocean tide models,” *Rev. Geophys.*, vol. 52, no. 3, pp. 243–282, 2014.
 - [42] Envisat-1 Products Specifications, *MWR Products Specifications, PO-RS-MDA-GS-2009. Rev. C. 13*, 1 2009.
 - [43] M. J. Fernandes, N. Pires, C. Lázaro, and A. Nunes, “Tropospheric delays from GNSS for application in coastal altimetry,” *Adv. Space Res.*, vol. 51, no. 8, pp. 1352–1368, 2013.
 - [44] M. J. Fernandes, L. Bastos, and M. Antunes, “Coastal satellite altimetry—methods for data recovery and validation,” in *3rd Meeting of the International Gravity and Geoid Commission Gravity and Geoid*”, pp. 26–30, 2002.
 - [45] C. Lázaro, M. Fernandes, A. Santos, and P. Oliveira, “Seasonal and interannual variability of surface circulation in the Cape Verde region from 8 years of merged T/P and ERS-2 altimeter data,” *Remote Sens. Environ.*, vol. 98, no. 1, pp. 45–62, 2005.
 - [46] J.-F. Legeais, M. Ablain, and S. Thao, “Evaluation of wet troposphere path delays from atmospheric reanalyses and radiometers and their impact on the altimeter sea level,” *Ocean Sci.*, vol. 10, no. 6, pp. 893–905, 2014.
 - [47] S. Brown, “A novel near-land radiometer wet path-delay retrieval algorithm: application to the Jason-2/OSTM advanced microwave radiometer,” *IEEE Trans. Geosci. Remote Sensing*, vol. 48, pp. 1986–1992, APR 2010.
 - [48] M. J. Fernandes, C. Lazaro, A. L. Nunes, N. Pires, L. Bastos, and V. B. Mendes, “GNSS-Derived path delay: An approach to compute the Wet Tropospheric Correction for coastal altimetry,” *IEEE Geosci. Remote Sens. Lett.*, vol. 7, pp. 596–600, JUL 2010.
 - [49] B. S. Yaplee, A. Shapiro, D. Hammond, B. Au, and E. Uliana, “Nanosecond radar observations of the ocean surface from a stable platform,” *IEEE T. Geosci. Elect.*, vol. 9, no. 3, pp. 170–174, 1971.

-
- [50] P. Prandi, A. Cazenave, and M. Becker, “Is coastal mean sea level rising faster than the global mean? A comparison between tide gauges and satellite altimetry over 1993–2007,” *Geophys. Res. Lett.*, vol. 36, no. 5, p. L05602, 2009.
 - [51] S. Barbosa, M. Silva, and M. J. Fernandes, “Changing seasonality in North Atlantic coastal sea level from the analysis of long tide gauge records,” *Tellus A*, vol. 60, no. 1, pp. 165–177, 2008.
 - [52] G. Chen and G. D. Quartly, “Annual amphidromes: a common feature in the ocean?,” *IEEE Geosci. Remote Sens. Lett.*, vol. 2, no. 4, pp. 423–427, 2005.
 - [53] S. V. Vinogradov, R. M. Ponte, P. Heimbach, and C. Wunsch, “The mean seasonal cycle in sea level estimated from a data-constrained general circulation model,” *J. Geophys. Res.-Oceans*, vol. 113, no. C3, 2008.
 - [54] S. Vinogradov and R. Ponte, “Annual cycle in coastal sea level from tide gauges and altimetry,” *J. Geophys. Res.-Space*, vol. 115, no. C4, p. C04021, 2010.
 - [55] L. Ruiz Etcheverry, M. Saraceno, A. Piola, G. Valladeau, and O. Möller, “A comparison of the annual cycle of sea level in coastal areas from gridded satellite altimetry and tide gauges,” *Cont. Shelf Res.*, vol. 92, pp. 87–97, 2015.
 - [56] P. Vincent, N. Steunou, E. Caubetq, L. Phalippou, L. Rey, E. Thouvenot, and J. Verron, “Altika: a Ka-band altimetry payload and system for operational altimetry during the GMES period,” *P. Soc. Photo-opt. Ins.*, vol. 6, no. 3, pp. 208–234, 2006.
 - [57] N. Steunou, J. Desjonquères, N. Picot, P. Sengenes, J. Noubel, and J. Poisson, “Altika altimeter: Instrument description and in flight performance,” *Mar. Geod.*, no. just-accepted, pp. 00–00, 2014.
 - [58] R. Morrow and P. Traon, “Recent advances in observing mesoscale ocean dynamics with satellite altimetry,” *Adv. Space Res.*, vol. 50, no. 8, pp. 1062–1076, 2011.
 - [59] P. C. Marth, J. R. Jensen, C. C. Kilgus, J. A. Perschy, J. L. MacArthur, D. W. Hancock, G. S. Hayne, C. L. Purdy, L. C. Rossi, and C. J. Koblinsky, “Prelaunch performance of the NASA altimeter for the TOPEX/Poseidon project,” *IEEE Trans. Geosci. Remote Sensing*, vol. 31, no. 2, pp. 315–332, 1993.

-
- [60] O. Zanife, P. Vincent, L. Amarouche, J. Dumont, P. Thibaut, and S. Labroue, “Comparison of the Ku-band range noise level and the relative sea-state bias of the Jason-1, TOPEX, and Poseidon-1 radar altimeters special issue: Jason-1 calibration/validation,” *Mar. Geod.*, vol. 26, no. 3-4, pp. 201–238, 2003.
 - [61] J. A. Nelder and R. Mead, “A simplex method for function minimization,” *The Computer Journal*, vol. 7, no. 4, pp. 308–313, 1965.
 - [62] D. M. Olsson and L. S. Nelson, “The Nelder-Mead simplex procedure for function minimization,” *Technometrics*, vol. 17, no. 1, pp. 45–51, 1975.
 - [63] Y. Faugere, J. Dorandeu, F. Lefevre, N. Picot, and P. Femenias, “Envisat ocean altimetry performance assessment and cross-calibration,” *Sensors*, vol. 6, no. 3, pp. 100–130, 2006.
 - [64] P. Thibaut, J. Poisson, E. Bronner, and N. Picot, “Relative performance of the MLE3 and MLE4 retracking algorithms on Jason-2 altimeter waveforms,” *Mar. Geod.*, vol. 33, no. S1, pp. 317–335, 2010.
 - [65] D. J. Wingham, “Onboard correction of mispointing errors in satellite altimeter returns,” *IEEE J. Oceanic Eng.*, vol. 13, no. 2, pp. 77–81, 1988.
 - [66] G. D. Quartly, “Optimizing σ^0 information from the Jason-2 altimeter,” *IEEE Geosci. Remote Sens. Lett.*, vol. 6, no. 3, pp. 398–402, 2009.
 - [67] L. Amarouche, P. Thibaut, O. Zanife, J.-P. Dumont, P. Vincent, and N. Steunou, “Improving the Jason-1 ground retracking to better account for attitude effects,” *Mar. Geod.*, vol. 27, no. 1-2, pp. 171–197, 2004.
 - [68] J. Dorandeu, M. Ablain, Y. Faugere, F. Mertz, B. Soussi, and P. Vincent, “Jason-1 global statistical evaluation and performance assessment: Calibration and cross-calibration results,” *Mar. Geod.*, vol. 27, no. 3-4, pp. 345–372, 2004.
 - [69] S. Querin, A. Crise, D. Deponte, and C. Solidoro, “Numerical study of the role of wind forcing and freshwater buoyancy input on the circulation in a shallow embayment (Gulf of Trieste, Northern Adriatic Sea),” *J. Geophys. Res.-Oceans*, vol. 111, no. C3, 2006.
 - [70] P.-M. Poulain, “Adriatic Sea surface circulation as derived from drifter data between 1990 and 1999,” *J. Marine Syst.*, vol. 29, no. 1, pp. 3–32, 2001.
 - [71] F. Stravisi, “Bora driven circulation in Northern Adriatic,” *Bollettino di Geofisica*, vol. 19, pp. 73–74, 1977.

-
- [72] A. Boyd and F. Shillington, “Physical forcing and circulation patterns on the Agulhas Bank,” *S. Afr. J. Sci.*, vol. 90, pp. 114–114, 1994.
 - [73] South African Navy, “South African tide tables,” *Tokai, South Africa*, 2007.
 - [74] E. H. Schumann, “Interannual wind variability on the south and east coasts of South Africa,” *J. Geophys. Res.-Atmospheres*, vol. 97, no. D18, pp. 20397–20403, 1992.
 - [75] O. Andersen, “The DTU10 gravity field and mean sea surface,” in *Second international symposium of the gravity field of the Earth (IGFS2)*, Univ. of Alaska Fairbanks, Fairbanks, 2010.
 - [76] L. Fenoglio-Marc, C. Dietz, and E. Grotten, “Vertical land motion in the Mediterranean Sea from altimetry and tide gauge stations,” *Mar. Geod.*, vol. 27, no. 3-4, pp. 683–701, 2004.
 - [77] L. Roblou, F. Lyard, M. Le Henaff, and C. Maraldi, “X-TRACK, a new processing tool for altimetry in coastal oceans,” in *IEEE Geoscience and Remote Sensing Symposium, Barcelona, Spain, (23-27 July 2007)*, pp. 5129–5133, IEEE, 2007.
 - [78] L. Roblou, J. Lamouroux, J. Bouffard, F. Lyard, M. Le Hénaff, A. Lombard, P. Marsaleix, P. De Mey, F. Birol, S. Vignudelli, *et al.*, “Post-processing altimeter data toward coastal applications and integration into coastal models,” in *Coastal Altimetry* (S. Vignudelli, A. Kostianoy, P. Cipollini, and J. Benveniste, eds.), (Berlin Heidelberg), pp. 217–246, Springer-Verlag, 2011.
 - [79] J. Bouffard, L. Roblou, F. Birol, A. Pascual, L. Fenoglio-Marc, M. Cancet, R. Morrow, and Y. Menard, “Introduction and assessment of improved coastal altimetry strategies: case study over the Northwestern Mediterranean Sea,” in *Coastal Altimetry* (S. Vignudelli, A. Kostianoy, P. Cipollini, and J. Benveniste, eds.), (Berlin Heidelberg), pp. 297–330, Springer-Verlag, 2011.
 - [80] F. García, M. Vigo, D. García-García, and J. Sánchez-Reales, “Combination of multisatellite altimetry and tide gauge data for determining vertical crustal movements along Northern Mediterranean Coast,” *Pure Appl. Geophys.*, vol. 169, no. 8, pp. 1411–1423, 2012.
 - [81] R. Dussurget, F. Birol, R. Morrow, and P. De Mey, “Fine resolution altimetry data for a regional application in the Bay of Biscay,” *Mar. Geod.*, vol. 34, no. 3-4, pp. 447–476, 2011.

-
- [82] G. Herbert, N. Ayoub, P. Marsaleix, and F. Lyard, “Signature of the coastal circulation variability in altimetric data in the southern Bay of Biscay during winter and fall 2004,” *J. Marine Syst.*, vol. 88, no. 2, pp. 139–158, 2011.
 - [83] Y. Liu, R. H. Weisberg, S. Vignudelli, L. Roblou, and C. R. Merz, “Comparison of the X-TRACK altimetry estimated currents with moored ADCP and HF radar observations on the West Florida Shelf,” *Adv. Space Res.*, vol. 50, no. 8, pp. 1085–1098, 2012.
 - [84] R. Ferrari, C. Provost, N. Sennéchael, and J.-H. Lee, “Circulation in Drake Passage revisited using new current time series and satellite altimetry: 2. The Ona basin,” *J. Geophys. Res.-Oceans*, vol. 117, 2013.
 - [85] A. Melet, L. Gourdeau, and J. Verron, “Variability in Solomon Sea circulation derived from altimeter sea level data,” *Ocean Dynam.*, vol. 60, no. 4, pp. 883–900, 2010.
 - [86] E. Gamboni, “Sul caposaldo fondamentale di riferimento della nuova rete altimetrica di alta precisione,” *Bollettino di Geodesia e Scienze Affini*, vol. 1, pp. 155–165, 1965.
 - [87] F. Stravisi and N. Purga, “Il livello del mare a Trieste: piani di riferimento e statistiche,” Tech. Rep. 112, Universita’ di Trieste, Dipartimento di Scienze della Terra, 2005.
 - [88] M. Becker, S. Zerbini, T. Baker, B. Bürki, J. Galanis, J. Garate, I. Georgiev, H.-G. Kahle, V. Kotzev, and V. Lobazov, “Assessment of height variations by GPS at Mediterranean and Black Sea coast tide gauges from the SELF projects,” *Global Planet. Change*, vol. 34, no. 1, pp. 5–35, 2002.
 - [89] C. Ferrarin, G. Umgiesser, I. Scroccaro, and G. Matassi, “Hydrodynamic modeling of the lagoons of Marano and Grado, Italy,” *ISMAR, ARPA*, 2009.
 - [90] R. L. Brooks, D. W. Lockwood, J. E. Lee, D. Handcock, and G. S. Hayne, “Land effects on TOPEX radar altimeter measurements in Pacific Rim coastal zones,” *Remote Sensing of the Pacific by Satellites*, edited by RA Brown, pp. 175–198, 1998.
 - [91] N. Picot, K. Case, S. Desai, and P. Vincent, “AVISO and PODAAC user handbook. IGDR and GDR Jason products,” *SMM_MU_M5_OP_13184_CN (AVISO) JPL D_21352 (PODAAC)*, 2003.

-
- [92] B. Lange, H. Johnson, S. Larsen, J. Højstrup, H. Kofoed-Hansen, and M. Yelland, “On detection of a wave age dependency for the sea surface roughness,” *J. Phys. Oceanogr.*, vol. 34, no. 6, pp. 1441–1458, 2004.
 - [93] S. Ermakov, S. Salashin, and A. Panchenko, “Film slicks on the sea surface and some mechanisms of their formation,” *Dynam. Atmos. Ocean*, vol. 16, no. 3, pp. 279–304, 1992.
 - [94] J. Ryan, A. Fischer, R. Kudela, M. McManus, J. Myers, J. Paduan, C. Ruhssam, C. Woodson, and Y. Zhang, “Recurrent frontal slicks of a coastal ocean upwelling shadow,” *J. Geophys. Res.-Oceans*, vol. 115, no. C12, 2010.
 - [95] P. Bonnefond, P. Exertier, O. Laurain, G. T., and P. Femenias, “Corsica: A multi-mission absolute calibration site,” in *Proceeding of 20 Years of Progress in Radar Altimetry*, ESA-SP-710, 2013.
 - [96] P. Bonnefond, P. Exertier, O. Laurain, P. Thibaut, and F. Mercier, “GPS-based sea level measurements to help the characterization of land contamination in coastal areas,” *Adv. Space Res.-Series*, vol. 51, pp. 1383–1399, 2012.
 - [97] K. Mittendorf, M. Kohlmeier, and W. Zielke, “A hind-cast data base for the design of offshore wind energy structures in the German Bight,” in *Coastal Engineering Conference*, vol. 29, p. 740, ASCE American Society Of Civil Engineers, 2004.
 - [98] L. Fenoglio-Marc, S. Dinardo, R. Scharroo, A. Roland, M. D. Sikiric, B. Lucas, M. Becker, J. Benveniste, and R. Weiss, “The German Bight: a validation of Cryosat-2 altimeter data in SAR mode,” *Adv. Space Res.*, vol. 55, no. 11, pp. 2641–2656, 2015.
 - [99] J. Schulz-Stellenfleth and E. Stanev, “Statistical assessment of ocean observing networks—a study of water level measurements in the German Bight,” *Ocean Model.*, vol. 33, no. 3, pp. 270–282, 2010.
 - [100] P. Thibaut, L. Amarouche, O. Zanife, N. Steunou, P. Vincent, and P. Raizonville, “Jason-1 altimeter ground processing look-up correction tables,” *Mar. Geod.*, vol. 27, no. 3-4, pp. 409–431, 2004.
 - [101] F. Monaldo, “Expected differences between buoy and radar altimeter estimates of wind speed and significant wave height and their implications on buoy-altimeter comparisons,” *J. Geophys. Res.-Oceans*, vol. 93, no. C3, pp. 2285–2302, 1988.

-
- [102] A. Alvera-Azcárate, D. Sirjacobs, A. Barth, and J.-M. Beckers, “Outlier detection in satellite data using spatial coherence,” *Remote Sens. Environ.*, vol. 119, pp. 84–91, 2012.
 - [103] T. Wahl, I. Haigh, P. Woodworth, F. Albrecht, D. Dillingh, J. Jensen, R. Nicholls, R. Weisse, and G. Wöppelmann, “Observed mean sea level changes around the North Sea coastline from 1800 to present,” *Earth-Sci. Rev.*, 2013.
 - [104] A. Stigebrandt, “Analysis of an 89-year-long sea level record from the Kattegat with special reference to the barotropically driven water exchange between the Baltic and the sea,” *Tellus A*, vol. 36, no. 4, pp. 401–408, 1984.
 - [105] K. Novotny, G. Liebsch, A. Lehmann, and R. Dietrich, “Variability of sea surface heights in the Baltic sea: An intercomparison of observations and model simulations,” *Mar. Geod.*, vol. 29, no. 2, pp. 113–134, 2006.
 - [106] M. Stramska, “Temporal variability of the Baltic Sea level based on satellite observations,” *Estuar. Coast. Shelf S.*, vol. 133, pp. 244–250, 2013.
 - [107] M. Stramska and N. Chudziak, “Recent multiyear trends in the Baltic Sea level,” *Oceanologia*, vol. 55, no. 2, 2013.
 - [108] M. Stramska, H. Kowalewska-Kalkowska, and M. Swirgon, “Seasonal variability in the Baltic Sea level,” *Oceanologia*, vol. 55, no. 4, 2013.
 - [109] E. Svendsen, J. Bemtsen, M. Skogen, B. Ådlandsvik, and E. Martinsen, “Model simulation of the Skagerrak circulation and hydrography during SKAGEX,” *J. Marine Syst.*, vol. 8, no. 3, pp. 219–236, 1996.
 - [110] N. G. Winther and J. A. Johannessen, “North Sea circulation: Atlantic inflow and its destination,” *J. Geophys. Res.-Oceans*, vol. 111, no. C12, 2006.
 - [111] M. Samuelsson and A. Stigebrandt, “Main characteristics of the long-term sea level variability in the Baltic sea,” *Tellus A*, vol. 48, no. 5, pp. 672–683, 1996.
 - [112] A. Lehmann, W. Krauß, and H.-H. Hinrichsen, “Effects of remote and local atmospheric forcing on circulation and upwelling in the Baltic Sea,” *Tellus A*, vol. 54, no. 3, pp. 299–316, 2002.
 - [113] G. Liebsch, K. Novotny, R. Dietrich, and C. Shum, “Comparison of multimission altimetric sea-surface heights with tide gauge observations in the Southern Baltic Sea,” *Mar. Geod.*, vol. 25, no. 3, pp. 213–234, 2002.

-
- [114] J. Holt and R. Proctor, “The seasonal circulation and volume transport on the northwest european continental shelf: A fine-resolution model study,” *J. Geophys. Res.-Oceans*, vol. 113, no. C6, 2008.
 - [115] W. Maslowski and W. Walczowski, “Circulation of the Baltic Sea and its connection to the Pan-Arctic region-a large scale and high-resolution modeling approach,” *Boreal Environ. Res.*, vol. 7, no. 4, pp. 319–326, 2002.
 - [116] H. Lass and V. Mohrholz, “On dynamics and mixing of inflowing saltwater in the Arkona Sea,” *J. Geophys. Res.-Oceans*, vol. 108, no. C2, 2003.
 - [117] Y. Cheng and O. B. Andersen, “Multimission empirical ocean tide modeling for shallow waters and polar seas,” *J. Geophys. Res.-Oceans*, vol. 116, no. C11, 2011.
 - [118] O. B. Andersen, A. Abulaitijiang, and L. Stenseng, “MSS at the coast. What Cryosat-2 revealed about existing MSS + Ocean Tide models in coastal & Arctic regions,” *presented at the 8th Coastal Altimetry Workshop, Konstanz, Germany, URL: http://www.coastalt.eu/files/konstanzwkshop14/pres/45_Andersen_MSSH.pdf*, 2014.
 - [119] L. Carrère and F. Lyard, “Modeling the barotropic response of the global ocean to atmospheric wind and pressure forcing-comparisons with observations,” *Geophys. Res. Lett.*, vol. 30, no. 6, p. 1275, 2003.
 - [120] R. Scharroo, E. W. Leuliette, J. L. Lillibridge, D. Byrne, M. C. Naeije, and G. T. Mitchum, “RADS: Consistent multi-mission products,” in *Proc. of the Symposium on 20 Years of Progress in Radar Altimetry, Venice, 20-28 September 2012*, vol. ESA SP-710, 2012.
 - [121] M. Bersch, V. Gouretski, R. Sadikni, and I. Hinrichs, “KLIWAS North Sea climatology of hydrographic data (version 1.0),” *World Data Center for Climate (WDCC)*, 2013.
 - [122] B. S. Giese and S. Ray, “El Niño variability in simple ocean data assimilation (SODA), 1871–2008,” *J. Geophys. Res.-Oceans*, vol. 116, no. C2, 2011.
 - [123] M. Passaro, P. Cipollini, S. Vignudelli, G. Quartly, and H. Snaith, “ALES: A multi-mission subwaveform retracker for coastal and open ocean altimetry,” *Remote Sens. Environ.*, vol. 145, pp. 173–189, 2014.

-
- [124] P. Cipollini, “A new parameter to facilitate screening of coastal altimetry data and corrections,” *presented at the 5th Coastal Altimetry Workshop, San Diego, USA*, 2011.
 - [125] J. M. Wooldridge, *Introductory Econometrics: A modern approach*. Thomson Learning, 3 ed., 2003.
 - [126] S. J. Prais and C. B. Winsten, “Trend estimators and serial correlation,” tech. rep., Cowles Commission discussion paper, 1954.
 - [127] M. Ablain, A. Cazenave, G. Valladeau, and S. Guinehut, “A new assessment of the error budget of global mean sea level rate estimated by satellite altimetry over 1993-2008.,” *Ocean Sci.*, vol. 5, no. 2, 2009.
 - [128] A. E. Gill, *Atmosphere-Ocean Dynamics*, vol. 30. Academic press, 1982.
 - [129] M. Tomczak and J. S. Godfrey, *Regional Oceanography: An Introduction*. Daya Books, 2003.
 - [130] S. R. Jayne, J. M. Wahr, and F. O. Bryan, “Observing ocean heat content using satellite gravity and altimetry,” *J. Geophys. Res.-Oceans*, vol. 108, no. C2, 2003.
 - [131] A. Lombard, A. Cazenave, P.-Y. Le Traon, and M. Ishii, “Contribution of thermal expansion to present-day sea-level change revisited,” *Glob. Planet. Change*, vol. 47, no. 1, pp. 1–16, 2005.
 - [132] M. Ekman, *The Changing Level of the Baltic Sea During 300 Years: A Clue to Understanding the Earth*. Summer Institute for Historical Geophysics Åland Islands, 2009.
 - [133] I. Karagali, A. Peña, M. Badger, and C. B. Hasager, “Wind characteristics in the North and Baltic seas from the QuikSCAT satellite,” *Wind Energy*, vol. 17, no. 1, pp. 123–140, 2014.
 - [134] D. L. Volkov and M. Pujol, “Quality assessment of a satellite altimetry data product in the Nordic, Barents, and Kara seas,” *J. Geophys. Res.-Oceans*, vol. 117, no. C3, p. C03025, 2012.
 - [135] S. Rudenko, M. Otten, P. Visser, R. Scharroo, T. Schöne, and S. Esselborn, “New improved orbit solutions for the ers-1 and ers-2 satellites,” *Adv. Space Res.*, vol. 49, no. 8, pp. 1229–1244, 2012.

-
- [136] A. Lehmann, “A three-dimensional baroclinic eddy-resolving model of the Baltic Sea,” *Tellus A*, vol. 47, no. 5, pp. 1013–1031, 1995.
 - [137] D. S. Danielssen, E. Svendsen, and M. Ostrowski, “Long-term hydrographic variation in the Skagerrak based on the section Torungen–Hirtshals,” *ICES Journal of Marine Science: Journal du Conseil*, vol. 53, no. 6, pp. 917–925, 1996.
 - [138] J. Wahr, D. A. Smeed, E. Leuliette, and S. Swenson, “Seasonal variability of the Red Sea, from satellite gravity, radar altimetry, and in situ observations,” *J. Geophys. Res.-Oceans*, 2014.
 - [139] M. Strassburg, B. Hamlington, R. Leben, P. Manurung, J. Lumban Gaol, B. Nababan, S. Vignudelli, and K.-Y. Kim, “Sea level trends in South East Asian Seas (SEAS),” *Climate Past Discuss.*, vol. 10, no. 5, pp. 4129–4148, 2014.
 - [140] H. Palanisamy, A. Cazenave, T. Delcroix, and B. Meyssignac, “Spatial trend patterns in the pacific ocean sea level during the altimetry era: The contribution of thermocline depth change and internal climate variability,” *Ocean Dynam.*, pp. 1–16, 2015.
 - [141] L. Fenoglio-Marc, T. Schöne, J. Illigner, M. Becker, P. Manurung, and Khafid, “Sea level change and vertical motion from satellite altimetry, tide gauges and GPS in the Indonesian region,” *Mar. Geod.*, vol. 35, no. sup1, pp. 137–150, 2012.
 - [142] A. L. Gordon, “The Indonesian Seas,” *Oceanography*, vol. 18, no. 4, p. 14, 2005.
 - [143] J. Durand and D. Petit, *The Java Sea Environment*, pp. 15–38. Jakarta, Indonesia: Indonesian Agency for Agriculture Research and Development, 2011.
 - [144] A. J. Clarke and X. Liu, “Observations and dynamics of semiannual and annual sea levels near the eastern equatorial Indian Ocean boundary,” *J. Phys. Oceanogr.*, vol. 23, no. 2, pp. 386–399, 1993.
 - [145] F. Syamsudin and A. Kaneko, “Ocean variability along the southern coast of Java and Lesser Sunda Islands,” *Journal of Oceanography*, vol. 69, no. 5, pp. 557–570, 2013.

-
- [146] A. L. Gordon and R. D. Susanto, “Banda Sea surface-layer divergence,” *Ocean Dynam.*, vol. 52, no. 1, pp. 2–10, 2001.
 - [147] C. Ray, C. Martin-Puig, M. P. Clarizia, G. Ruffini, S. Dinardo, C. Gommenginger, and J. Benveniste, “SAR altimeter backscattered waveform model,” *IEEE Trans. Geosci. Remote Sensing*, vol. 53, no. 2, pp. 911–919, 2015.
 - [148] S. Dinardo and J. Benveniste, “Guidelines for the SAR (Delay-Doppler) L1b Processing,” *ESA document, reference XCRY-GSEG-EOPS-TN-14-0042*, 2013.
 - [149] E. S. Garcia, D. T. Sandwell, and W. H. Smith, “Retracking Cryosat-2, Envisat and Jason-1 radar altimetry waveforms for improved gravity field recovery,” *Geophys. J. Int.*, p. ggt469, 2014.
 - [150] F. Lyard, F. Lefevre, T. Letellier, and O. Francis, “Modelling the global ocean tides: Modern insights from FES2004,” *Ocean Dynam.*, vol. 56, no. 5-6, pp. 394–415, 2006.
 - [151] A. Koch-Larrouy, G. Madec, P. Bouruet-Aubertot, T. Gerkema, L. Bessières, and R. Molcard, “On the transformation of pacific water into indonesian throughflow water by internal tidal mixing,” *Geophys. Res. Lett.*, vol. 34, no. 4, 2007.
 - [152] S. Labroue, F. Boy, N. Picot, M. Urvoy, and M. Ablain, “First quality assessment of the Cryosat-2 altimetric system over ocean,” *Adv. Space Res.*, vol. 50, no. 8, pp. 1030–1045, 2012.
 - [153] R. M. Ponte and R. D. Ray, “Atmospheric pressure corrections in geodesy and oceanography: A strategy for handling air tides,” *Geophys. Res. Lett.*, vol. 29, no. 24, pp. 6–1, 2002.
 - [154] J. Liu, R. Chen, Z. Wang, and H. Zhang, “Spherical cap harmonic model for mapping and predicting regional TEC,” *GPS solutions*, vol. 15, no. 2, pp. 109–119, 2011.
 - [155] S. Jin, O. Luo, and S. Gleason, “Characterization of diurnal cycles in ZTD from a decade of global GPS observations,” *J. Geodesy*, vol. 83, no. 6, pp. 537–545, 2009.
 - [156] J. Sprintall, A. L. Gordon, R. Murtugudde, and R. D. Susanto, “A semiannual Indian Ocean forced Kelvin wave observed in the Indonesian seas in May 1997,” *J. Geophys. Res.-Oceans*, vol. 105, no. C7, pp. 17217–17230, 2000.

-
- [157] J. Sprintall and A. Révelard, “The Indonesian Throughflow response to Indo-Pacific climate variability,” *J. Geophys. Res.-Oceans*, vol. 119, no. 2, pp. 1161–1175, 2014.
 - [158] A. Melet, M. Nonti, B. Chide, B. Meyssignac, and F. Birol, “Comparing coastal and open ocean sea level variability and trend from altimetric data,” *presented at the Ocean Surface Topography Science Team meeting, Konstanz, Germany*, 2014.
 - [159] R. Nerem, D. Chambers, C. Choe, and G. Mitchum, “Estimating mean sea level change from the TOPEX and Jason altimeter missions,” *Mar. Geod.*, vol. 33, no. S1, pp. 435–446, 2010.
 - [160] R. D. Susanto and Y. T. Song, “Indonesian throughflow proxy from satellite altimeters and gravimeters,” *J. Geophys. Res.-Oceans*, vol. 120, no. 4, pp. 2844–2855, 2015.
 - [161] K. Pujiana, A. L. Gordon, and J. Sprintall, “Intraseasonal Kelvin wave in Makassar Strait,” *J. Geophys. Res.-Oceans*, vol. 118, no. 4, pp. 2023–2034, 2013.
 - [162] A. Cazenave, H.-B. Dieng, B. Meyssignac, K. von Schuckmann, B. Decharme, and E. Berthier, “The rate of sea-level rise,” *Nature Clim. Change*, vol. 4, no. 5, pp. 358–361, 2014.
 - [163] C. Boening, J. K. Willis, F. W. Landerer, R. S. Nerem, and J. Fasullo, “The 2011 La Niña: So strong, the oceans fell,” *Geophys. Res. Lett.*, vol. 39, no. 19, p. L19602, 2012.